Development of dielectric materials for low temperature co-fired ceramics (LTCC) application

By

Xiaozhou Wang

Research School of Chemistry

The Australian National University

A thesis submitted for the degree of Doctor of philosophy of The Australian National University

Australian National University

September 2020

Declaration

This thesis is a collection of the major outcomes arising from my own independent research work during my PhD candidature. Except where specifically mentioned in the text, this thesis constitutes original work carried out by the candidate.

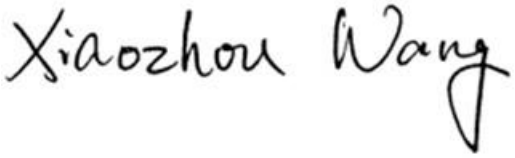

September 2020

Acknowledgement

First of all, I would like to sincerely thank my supervisor, Prof. Yun Liu, for giving me the opportunity and financial support to study for my PhD degree. Her rich professional knowledge and spiritual encouragements are the strong support for me to complete the project. I also acknowledge Prof. Lan Fu (Research School of Physics and Engineering), Dr. Hua Chen (Centre for Advanced Microscopy) and Dr. David Cortie (University of Wollongong) for their enthusiastic co-supervision.

I would also appreciate Dr. Genmiao Wang for his timely technique supports and Dr. Jianli Wang for his help in XRD refinement.

Gratitude also expressed to Dr. Tao Chen of Guangdong Fenghua Advanced Technology Holding Co., LTD. and Shaun Kenny, as well as Carlie Piggott, of ALS Company for their help in some important characterizations.

Also thanks for the assistance from our group members, including Dr. Qingbo Sun, Dr. Teng Lu, Dr. Narendirakumar Narayanan, Dr. Bethany MacBride, Dr. Wen Dong, Mr. Haoxin Mai, Miss Jianmei Liu, Mr. Zhen Liu, Mr. Farzin Nekouei and Mr. Tongwei Yuan.

Last but not least, I would also thanks my grandparents, parents and friends for their help and love, which support me overcome the difficulties in my life. Special thanks to my wife, Jing Dong, for taking care of our clever and lovely daughter, Ziying Wang, during my study period.

Abstract

Low temperature co-fired ceramics (LTCC) technology allows constructing three-dimensional structure of electronic devices and components, and facilitates the assembly of devices made of different types of materials and presented with different functions. This LTCC technology would increase device integration density whilst shortening internal electrical connection, and subsequently benefiting the manufacturing of portable electronic devices and the application of these devices/components in communication technology. The development of high performance LTCC materials, which either intrinsically have a low sintering temperature or enable to be sintered at relatively low temperature with the assistance of sintering aids or glasses, is a big challenging in this field due to the limitation of the processing conditions and the selection of potential candidate materials. The controllable stability and repeatability are also critical issues. This thesis is to challenge these difficulties by conducting systematic research on the chemical composition, phase formation, structure as well as electrical and thermal properties of potential candidate materials to successfully develop a series of LTCC materials with optimal performance.

In this thesis, the novel sol-gel process is introduced to prepare the amorphous phase, rather than using traditional molten glass, for better chemical composition control (e.g. precisely adjusting composition and avoiding the loss of low-melting chemical component). For instance, boron, a typical element often appears in molten glass, generally would have 15-25% loss relevant to its nominal composition. Using the approach proposed in this work, the resultant boron content is consistent with nominal composition and the volatilisation is completely suppressed. To do so, two amorphous materials, denoted as Amorphous phase-1 and Amorphous phase-2, are hence able to be synthesised in the temperature range of 600 ^{o}C and 700 ^{o}C. The final chemical composition of Amorphous phase-1 is 79.51% SiO_2-0.81% Na_2O-2.41% K_2O-2.50% CaO-14.77% B_2O_3 (mole ratio), and that of Amorphous phase-2 is 80.78% SiO_2-0.27% Na_2O-0.87% K_2O-3.45% CaO-5.25% BaO-9.38% B_2O_3 (mole ratio). The particle size distribution of such obtained amorphous materials is in the micrometre range. The processing condition is optimized to significantly reduce, if it is not completely avoided, any

potentially residual carbon, and also avoid potential crystallisation out of the amorphous phase due to a high temperature treatment. The existence and controllability of such chemical components (with low melting point) in amorphous phases will reduce the sintering temperature of LTCC materials in a manageable manner, facilitating the optimization of chemical compositions, process conditions and subsequently properties of LTCC materials.

The sol-gel derived amorphous phases are used to develop the LTCC composites with dielectric constant at different values (5, 7~8 and 11) and optimized thermal expansion property. As results, the hexagonal Al_2O_3 is mixed with 50.19 wt% Amorphous phase-1 and 46.65 wt% Amorphous phase-2, respectively, to form the composites which show dielectric constant of 7~8 and the coefficient of thermal expansion (CTE) of ~ 6 ppm/^oC when sintered between 850 ^oC and 900 ^oC for 6h. The composite made up of 60 wt% monoclinic ZrO_2 and 40 wt% Amrophous phase-1 presents dielectric constant of ~ 11 and CTE of ~ 6 ppm/^oC when sintered at 850 ^oC for 30min. The composite with the composition of 42.86 wt% Amorphous phase-1+52.38 wt% fused SiO_2+4.76 wt% Al_2O_3 exhibits dielectric constant of ~5 and CTE of 3.26 ppm/^oC when sintered at 850 ^oC for 6h.

Although the hexagonal Al_2O_3, monoclinic ZrO_2 and pure fused SiO_2 require high sintering temperature (>1500 ^oC), the sol-gel derived amorphous phase can form the vacuous liquid and then densify the composites below 900 ^oC, due to its low softening temperatures (~800 ^oC). And the dielectric constant of the sol-gel derived amorphous phases are ~ 6.2. Therefore, the composites with relative permittivity of 4~6.2, 6.2~10 and 6.2~20 are achievable via mixing the sol-gel derived amorphous phase with pure fused SiO_2 (ε_r=4), hexagonal Al_2O_3 (ε_r=10) and monoclinic ZrO_2 (ε_r=20), respectively, according to the mixing rule.

To optimize the thermal expansion property, the formation of the SiO_2-based cristobalite phase, which causes abrupt change of thermal expansion at ~200 ^oC due to the tetragonal-to-cubic phase transition, in monoclinic ZrO_2 and pure fused SiO_2 based composites is suppressed by adjusting the chemical composition and synthesis condition. For the monoclinic ZrO_2 based composite, the SiO_2-based cristobalite phase should come from the Amorphous phase-1 in view of the chemical composition and its amount shows evident dependence on the soaking time.

Therefore we eliminate it by reducing the amount of Amorphous phase-1 in the raw materials and the sintering time. For the pure fused SiO_2 based composite, the formation of cristobalite phase is suppressed by Al_2O_3, but the sintering temperature is limited at 800 ^oC. In this case, the cristobalite phase can be from either fused SiO_2 or sol-gel derived Amorphous phase-1, so we need to figure out which of them were the origin of the cristobalite phase before further optimization. Based on the X-ray powder diffraction (XRD) characterization, it is found the undesired cristobalite phase originates from the Amorphous phase-1 since it will get crystallized at lower temperature compared with the pure fused SiO_2. Thus the proportion of Amorphous phase-1 in this composite is reduced and while the sample is sintered at 850 ^oC, the cristobalite phase disappears. This series of LTCC materials with adjustable dielectric constant and appropriate thermal expansion property can provide a flexibility in electronic circuit designs.

Besides the sol-gel derived amorphous phases, we also introduced a cubic $KBSi_2O_6$ phase with simpler composition as the precursor to develop the LTCC materials for the first time. Different from the amorphous phase forming vacuous liquid to densify the composites, this silicate exhibits good tolerance for ionic substitutions (such as Al substituting B), and thus lead to intimate contact of phases in the sintered sample to achieve well densified microstructure. As the result, the composition of developed sample is Al_2O_3: $KBSi_2O_6$: CaO=1.07: 1: 0.4 (mole ratio). It shows dielectric constant of ~8 and CTE of 11.04~12.46 ppm/^oC when sintered between 850 ^oC and 900 ^oC. With the optimization of three components, we initially developed a composite with composition of Al_2O_3: $KBSi_2O_6$: CaO=1: 1: 0.4. After sintered between 850 ^oC and 900 ^oC for 6h, the final composites contains $KAlSi_2O_6$, Al_2O_3 and $CaAl_2Si_2O_8$ phase. The dielectric constant of $KAlSi_2O_6$, Al_2O_3 and $CaAl_2Si_2O_8$ phase are 6.8, 10 and 6.9, respectively, resulting in a low permittivity (6.8~10) of the final sample. By adjusting the soaking period from 0.5h to 6h, the amount of the $CaAl_2Si_2O_8$ phase increases evidently but the resistivity of the corresponding sample does not show significant differences. When the sintering time further extends to 12h, no obvious change of the phase fraction of $CaAl_2Si_2O_8$ can be obtained in the XRD pattern but the resistivity of sample is obviously enhanced. Therefore, the $CaAl_2Si_2O_8$ phase has no evident influence on the resistivity of sample. The CaO

in the raw materials is necessary for the crystallization of $CaAl_2Si_2O_8$ phase which does not present significant impacts on the resistivity of resultant samples. Therefore, to achieve the sample with higher resistivity, the amounts of other raw materials, *i.e.*, Al_2O_3 and $KBSi_2O_6$, are adjusted. Finally, addition of 2 wt% Al_2O_3 leads to a higher resistivity without any side effect on the dielectric properties.

Overall, utilising the sol-gel derived amorphous phases and unique crystalline $KBSi_2O_6$ phase as the precursors enables controllable design of LTCC materials. And as a result, through systematic investigation presented in this thesis, we have developed five LTCC materials with tuneable dielectric constant in the range of 4-12 (at 1MHz). These materials show dielectric loss below 0.003 (at 1MHz) and resistivity above 10^{12} Ω·cm. The thermal expansion property is also adjusted to be in the acceptable range to match with the substrates, including silicon, alumina substrates and printed circuit board. All designed LTCC materials can be co-fired with silver electrode at the temperature range of 850-900 ^{o}C without any internal diffusion, avoiding the potential silver immigration-induced failure and significantly increasing the service lifetime of LTCC devices in practical application. Also industrial trial has been conducted by industrial collaboration partner which confirmed the validation of these LTCC materials.

Table of Content

Acknowledgement II

Abstract III

List of Figures XI

List of Tables XVII

Glossary and List of Abbreviations XVIII

Chapter 1 Introduction 1

1.1 Applications of LTCC technology 1

1.2 The fabrication process of LTCC modules 4

1.3 Key technique requirements for LTCC materials 6

1.3.1 Low sintering temperature and compatibility with electrode 6

1.3.2 Dielectric properties 8

1.4 LTCC materials 10

1.5 Thermal expansion 16

1.6 Shrinkage phenomenon 17

1.7 Motivation and outline of the thesis 18

Reference 21

Chapter 2 Experimental and characterization methods 29

2.1 Chemicals 29

2.2 Experimental methods 30

2.2.1 Amorphous phases and ceramics composites 30

2.2.2 Crystalline composite 32

2.2.3 Compatibility with silver electrode 32

2.3 Structures and compositions characterization 33

2.3.1 X-ray diffraction 33
2.3.2 Attenuated total reflectance Fourier transform infrared spectroscopy 34
2.3.3 Laser scattering 35
2.3.4 Scanning electron microscope 37
2.3.5 X-ray fluorescence spectrometer 38
2.3.6 Inductively coupled plasma atomic emission spectroscopy 39
2.4 Electrical properties measurement 40
2.4.1 Dielectric measurement 40
2.4.2 Resistivity measurement 40
2.5 Thermal properties measurement 41
2.5.1 Thermal expansion measurement 41
2.5.2 Glass transition temperature measurement 41
Reference 42
Chapter 3 Sol-gel derived amorphous phases for Al_2O_3-based composites 44
3.1 Introduction 44
3.2 Syntheses, structures and properties of sol-gel derived amorphous phases 46
3.2.1 Amorphous phase-1 46
3.2.2 Amorphous phase-2 51
3.3 Synthesis, structure and performance of Amorphous phase-1/Al_2O_3 composite 55
3.3.1 Synthesis of Amorphous phase-1/Al_2O_3 composite 55
3.3.2 Structure and performance of Amorphous phase-1/Al_2O_3 composite 56
3.4 Synthesis, structure and performance of Amorphous phase-2/Al_2O_3 composite 60
3.4.1 Synthesis of Amorphous phase-2/Al_2O_3 composite 60
3.4.2 Structure and performance of Amorphous phase-2/Al_2O_3 composite 60

3.5 Conclusion 64

Reference 66

Chapter 4 Tuning of dielectric constant for amorphous phase-based composites 70

4.1 Monoclinic ZrO_2 for composite with high dielectric constant 70

4.1.1 Background 70

4.1.2 Synthesis of the ZrO_2/amorphous phase composite 72

4.1.3 Compositions, structures and properties of ZrO_2/amorphous phase composite 72

4.2 Pure fused SiO_2 for composite with low dielectric constant 82

4.2.1 Background 82

4.2.2 Synthesis of amorphous phase/fused SiO_2/Al_2O_3 composite 83

4.2.3 Compositions, structures and properties of amorphous phase/fused SiO_2/Al_2O_3 composite 84

4.3 Conclusion 92

Reference 94

Chapter 5 A crystalline composite for LTCC application 98

5.1 Introduction 98

5.2 Experimental procedures 99

5.3 Compositions, structures and electrical properties of the crystalline composite 100

5.4 Improvement of resistivity and associated properties 108

5.5 Conclusion 117

Reference 119

Chapter 6 Main achievements and outlook 122

6.1 Main achievements 122

6.2 Future work 125

Publication.....127

List of Figures

Fig. 1-1 (a) Aperture-coupled stacked patch microstrip antenna using LTCC technology (Reproduced from Bhutani A. et al[1]); (b) Schematic representation of the NO_2 gas sensor based on LTCC technology (Reproduced from Ma M. et al[5]); (c) Fuel cell system based on LTCC technology (Reproduced from Goldberg A. et al[6]);.....2

Fig. 1-2 Examples of integration and device miniaturization by LTCC technology, where (a) & (b) are reproduced from Jiang W. et al.[11] and (c) & (d) are reproduced from Sickinger F. et al.[12].....3

Fig. 1-3 A typical flowing diagram of tape casting method for preparing LTCC modules.[18]...5

Fig. 1-4 Resistivities and melting points of common metal electrodes (Data are collected from Imanaka Y. and Chance D. A. et al[15, 21]).....7

Fig. 1-5 Polarization mechanisms of dielectric materials over a wide range of frequencies. The figure is reproduced from Khaled D. E. et al[25]. 9

Fig. 1-6 Relationship between signal propagation delay and dielectric constant in the case of ceramic package. The figure is reproduced from Sebastian M. T. et al[31].....9

Fig. 1-7 Summary and classification of reported LTCC materials. The inserted figure about the densification process is reproduced from Zhou J.[24].....12

Fig. 1-8 Structure of the pure amorphous silica glass and multi-components silica glass, which are reproduced from Vallet-Reg íM.[55].....13

Fig. 1-9 Modulation of the coefficients of thermal expansion (CTE) of Li_2O-Al_2O_3-SiO_2 glass by addition of MgO. The figure and inserted table are reproduced from Qing Z. et al[79]. 17

Fig. 1-10 LTCC tapes laminate with sacrificial tapes in the green state (above) and after sintering (below), which are reproduced from Rabe T. et al[80].....18

Fig. 2-1 Main process to synthesize multi-components amorphous phases using sol-gel method. 30

Fig. 2-2 Dependence of hydrolysis (blue curve) and condensation (orange curve) rates of tetraethyl orthosilicate on pH. (The figure is reproduced from Montheil T. et al.[2]).....31

Fig. 2-3 Schematic of Bragg's law for X-ray diffractions. (The figure is reproduced from Askeland D. R. et al.[3]) 33

Fig. 2-4 Schematic representation of an ATR-FTIR system. (The figure is reproduced from Ausili A. et al.[6]) 35
Fig. 2-5 Relationship between particle size (D) and light intensity distribution of scattered light. (The figure is reproduced from Shen S. et al.[8]). 37
Fig. 2-6 Signals generated when the electron beam interacts with the sample. (The figure is reproduced from Zhang S.[9]).....37
Fig. 3-1 XRD patterns of the Amorphous phase-1 xerogel and that calcined from 600^{o}C to 800^{o}C for 2h. 47
Fig. 3-2 Attenuated total reflectance Fourier transform infrared (ATR-FTIR) spectroscopy of the Amorphous phase-1 powder calcined at 700^{o}C from 4000cm^{-1} to 400cm^{-1}. 48
Fig. 3-3 Particle size distribution of the Amorphous phase-1 powders calcined at 700^{o}C.....49
Fig. 3-4 Thermogravimetric-differential thermal analysis (TG-DTA) characterization of Amorphous phase-1 powder calcined at 700^{o}C. 50
Fig. 3-5 XRD patterns of the Amorphous phase-2 xerogel and that calcined between 600^{o}C and 800^{o}C.....52
Fig. 3-6 Attenuated total reflectance Fourier transform infrared (ATR-FTIR) spectroscopy of Amorphous phase-2 powder calcined at 600^{o}C from 4000cm^{-1} to 400cm^{-1}. 53
Fig. 3-7 Particle size distribution of the Amorphous phase-2 powder calcined at 600^{o}C for 2h. 54
Fig. 3-8 Thermogravimetric-differential thermal analyses (TG-DTA) curve of the calcined Amorphous phase-2 powder at the heating rate of 10^{o}C/min. 55
Fig. 3-9 (a) Dielectric properties (@1MHz); (b) Resistivities and XY shrinkages of samples with composition of 49.81wt% Al_2O_3 and 50.19wt% Amorphous phase-1 powder sintered from 850^{o}C to 900^{o}C. 56
Fig. 3-10 XRD patterns of the Amorphous phase-1/Al_2O_3 composite sintered between 850^{o}C and 900^{o}C. 57
Fig. 3-11 SE image of Amorphous phase-1/Al_2O_3 composite sintered at (a) 850^{o}C, (b) 875 ^{o}C and (c) 900^{o}C. 58

Fig. 3-12 SEM of the cross section of cofired Ag/LTCC interface and the atomic percentage of Ag at the interface. 59
Fig. 3-13 Coefficient of thermal expansion (CTE) of Amorphous phase-1/Al_2O_3 composite sintered at 850°C and 900°C. 59
Fig. 3-14 XRD patterns of the sample with composition of 53.35wt% Al_2O_3 and 46.65wt% Amorphous phase-2 powder sintered from 825°C to 900°C. 61
Fig. 3-15 (a) Dielectric properties of samples with composition of 53.35wt% Al_2O_3 and 46.65wt% Amorphous phase-2 powder sintered between 825°C and 900°C; (b) Resisitivities and XY shrinkages of the corresponding samples. 62
Fig. 3-16 SEM image of samples with composition of 53.35wt% Al_2O_3 and 46.65wt% Amorphous phase-2 powder sintered at (a) 825°C, (b) 850°C, (c) 875°C, (d) 900°C. 63
Fig. 3-17 SEM imgae of the cross section of Ag electrode/ LTCC interface and corresponding atomic percentage of Ag at the interface. 63
Fig. 3-18 Coefficient of thermal expansion (CTE) of samples with the composition of 53.35wt% Al_2O_3 and 46.65wt% Amorphous phase-2 powder sintered at 850°C and 900°C. 64
Fig. 4-1 XRD patterns of samples with various ZrO_2/Amorphous phase-1 ratio sintered at 850°C for 6h. 73
Fig. 4-2 (a) Dielectric properties (@1MHz) and (b) Resistivities (100V, DC) and XY shrinkages of samples with various amount of ZrO_2 in the raw materials and sintered at 850°C for 6h. 74
Fig. 4-3 XRD patterns of sampls with composition of ZrO_2: Amorphous phase-1= 60: 40 sintered at 850°C with soaking period from 0.5h to 6h. 74
Fig. 4-4 (a) Backscattered electron (BSE) image and (b) secondary electron (SE) image of samples with composition of ZrO_2: Amorphous phase-1= 60: 40 sintered at 850°C for 6h. .. 75
Fig. 4-5 Backscattered electron (BSE) image of the dark region in the sample with composition of ZrO_2: Amorphous phase-1= 60: 40 sintered at 850°C for 6h. 77
Fig. 4-6 Microstructure of the Si-Zr-rich region in the sample with composition of ZrO_2: Amorphous phase-1= 60: 40 sintered at 850°C for 6h. 79

Fig. 4-7 (a) Backscattered electron image (BSE) and (b) secondary electron (SE) image of samples with composition of ZrO_2: Amorphous phase-1= 60: 40 sintered at 850°C for 0.5h.79
Fig. 4-8 Coefficient of thermal expansion of the samples with composition of ZrO_2: Amorphous phase-1= 60: 40 sintered at 850°C for various soaking period. 80
Fig. 4-9 (a) Frequency and (b) temperature dependence of dielectric properties of samples with composition of ZrO_2: Amorphous phase-1= 60: 40 sintered at 850°C for 0.5h. 80
Fig. 4-10 (a) and (c) SEM image of the cross section of the LTCC/Ag interface; (b) and (d) Atomic percentage of Ag at the interface. 81
Fig. 4-11 (a) XRD patterns of Amorphous phase-1 powder heated from 700°C to 800°C. (b) XRD patterns of raw fused SiO_2 and that heated between 900°C and 1000°C.....84
Fig. 4-12 Dielectric properties (@1MHz) of samples with the composition of Amorphous phase-1: pure fused SiO_2=50.19: 49.81and sintered from 800°C to 900°C. 85
Fig. 4-13 XRD patterns of samples (Amorphous phase-1: pure fused SiO_2=50.19: 49.81) with 0~5wt% addition of Al_2O_3 sintered at 800°C. 86
Fig. 4-14 (a) XRD patterns of samples with composition of Amorphous phase-1: fused SiO_2=50.19: 49.81and 5wt% Al_2O_3 sintered between 800°C and 850°C; (b) XRD patterns of samples with various Amorphous phase-1/fused SiO_2 ratio and 5wt% Al_2O_3 sintered at 850°C. 87
Fig. 4-15 SEM images of samples with various Amorphous phase-1/fused SiO_2 ratio and 5wt% Al_2O_3: (a) and (b) Amorphous phase-1: fused SiO_2=40:60; (c) and (d) Amorphous phase-1: fused SiO_2=45:55; (e) and (f) Amorphous phase-1: fused SiO_2=50.19:49.81; (g) and (h) Amorphous phase-1: fused SiO_2=55:45. 89
Fig. 4-16 (a) Dielectric properties and (b) resistivities and XY shrinkages of samples with various Amorphous phase-1/fused SiO_2 ratio and 5wt% Al_2O_3 sintered at 850°C.....89
Fig. 4-17 (a) The dielectric properties (at room temperature) of the samples with composition of 42.86wt% Amorphous phase-1- 52.38wt% pure fused SiO_2- 4.76wt% Al_2O_3 sintered at 850°C; (b) The temperature dependence of dielectric properties (@1MHz) from 30°C to 100°C. 90

Fig. 4-18 Backscattered image of the cross section of sintered sample and the atomic percentage of Ag at the LTCC/Ag electrode interface. 91
Fig. 4-19 Coefficient of thermal expansion of the samples with composition of 42.86wt% Amorphous phase-1- 52.38wt% pure fused SiO_2- 4.76wt% Al_2O_3 sintered at 850°C. 92
Fig. 5-1 XRD patterns of raw materials (a) Al_2O_3 powders with different particle sizes; (b) $CaCO_3$ powders before and after calcination at 1000°C. 101
Fig. 5-2 XRD refinement result of the as-synthesized $KBSi_2O_6$ phase using Rietveld method. The inserted plot presents its crystal structure, where the B and Si occupy the same site. ... 101
Fig. 5-3 (a) Dielectric properties (@1MHz); (b) Resistivities and shrinkages in XY plane of the sintered samples with $CaCO_3$ and CaO as calcium source. 103
Fig. 5-4 (a) Dielectric properties; (b) Resistivities and XY-shrinkages of samples with various amount of CaO sintered at 950°C; (c) and (d) performance of samples with composition of Al_2O_3(135nm): $KBSi_2O_6$: CaO=1: 0.5: 0.2 sintered between 900°C and 950°C. 103
Fig. 5-5 (a) and (b) Electrical properties and XY shrinkages of samples with addition of $KBSi_2O_6$ sintered from 800°C to 950°C; (c) and (d) electrical properties and XY shrinkages of samples with various amount of CaO in Al_2O_3: $KBSi_2O_6$: CaO =1: 0.75: x composite sintered at 850°C and 900°C; (e) and (f) electrical properties and XY shrinkages of samples with various amount of CaO in Al_2O_3: $KBSi_2O_6$: CaO =1: 1: x composite sintered at 850°C and 900°C. 105
Fig. 5-6 (a) Dielectric properties; (b) resistivities and XY shrinkages; (c) XRD patterns of samples with Al_2O_3 at different particle sizes in composition of Al_2O_3: $KBSi_2O_6$: CaO=1: 1: 0.4 sintered at 900°C. 106
Fig. 5-7 XRD patterns of samples with the composition of Al_2O_3 (300nm): $KBSi_2O_6$: CaO=1: 1: 0.4 (mole ratio) sintered between 850°C and 900°C. 107
Fig. 5-8 (a) Dielectric properties of samples with the composition of Al_2O_3 (300nm): $KBSi_2O_6$: CaO=1: 1: 0.4 (mole ratio) @1MHz sintered from 850°C to 900°C; (b) resistivities of the corresponding samples tested under 100V (DC) and shrinkages in XY plane. 108
Fig. 5-9 XRD patterns of samples with composition of Al_2O_3 (300nm): $KBSi_2O_6$: CaO=1:1:0.4 sintered at 900°C for 0.5h, 6h and 12h. 109

Fig. 5-10 (a) Resistivities of samples with composition of Al_2O_3 (300nm): $KBSi_2O_6$: CaO=1: 1: 0.4 sintered at 900°C for different time; (b) influence of Al_2O_3 (300nm) and $KBSi_2O_6$ on resistivities of developed samples sintered from 850°C to 900°C for 6h. 110
Fig. 5-11 Dielectric properties of samples with addition of 2%~10% Al_2O_3 (300nm) sintered between 850°C and 900°C. 111
Fig. 5-12 (a) Coefficients of thermal expansion (CTE); (b) XRD patterns of samples with composition of Al_2O_3 (300nm): $KBSi_2O_6$: CaO=1.07: 1: 0.4 sintered between 850°C and 900°C. 112
Fig. 5-13 SEM images of samples with composition of Al_2O_3 (300nm): $KBSi_2O_6$: CaO=1.07:1:0.4 sintered at (a) and (b) 850°C; (c) and (d) 875°C; (e) and (f) 900°C. 113
Fig. 5-14 Backscattered electron image of sample with composition of Al_2O_3 (300nm): $KBSi_2O_6$: CaO=1.07:1:0.4 sintered at 850°C. The numbers specify the locations of point analyses. 114
Fig. 5-15 Backscattered electron image of sample with composition of Al_2O_3 (300nm): $KBSi_2O_6$: CaO=1.07: 1: 0.4 sintered at 900°C. The numbers specify the locations of point analyses. 115
Fig. 5-16 SEM image of the cross section of sample co-fired with Ag electrode at (a) 850°C; (b) 900°C; (c) atomic percentage of silver in a series of point analyses. 117

List of Tables

Tab. 1-1 Target of the performance for the developed samples. 19

Tab. 2-1 Information about chemicals involved in this thesis. 29

Tab. 2-2 Particle size characterization techniques and corresponding measuring range. 35

Tab. 3-1 Comparison of nominal composition and characterized composition of Amorphous phase-1. 49

Tab. 3-2 Comparison of nominal composition and characterized composition of Amorphous phase-2. 53

Tab. 4-1 Atomic percentage of elements in different regions of the sample with composition of ZrO_2: Amorphous phase-1= 60: 40 sintered at 850^oC for 6h. 76

Tab. 4-2 Atomic percentage of elements in the dark region of the sample with composition of ZrO_2: Amorphous phase-1= 60: 40 sintered at 850^oC for 6h. 77

Tab. 5-1 Refined atomic fractional coordinates from XRD data for $KBSi_2O_6$ sample. 102

Tab. 5-2 Point analyses of different regions in the sample sintered at 850^oC. 114

Tab. 5-3 Point analyses of different regions in the sample sintered at 900^oC. 116

Tab. 6-1 Performance of developed samples in this project. The chemical composition of Amorphous phase-1 is 79.51% SiO_2-0.81% Na_2O-2.41% K_2O-2.50% CaO-14.77% B_2O_3 (mole ratio), and that of Amorphous phase-2 is 80.78% SiO_2-0.27% Na_2O-0.87% K_2O-3.45% CaO-5.25% BaO-9.38% B_2O_3 (mole ratio). 122

Glossary and List of Abbreviations

Description	Abbreviation
Low temperature co-fired ceramic	LTCC
Polarisation	P
Electric field	E
Direct current	DC
Dielectric constant/ Relative permittivity	ε_r
Dielectric loss	tanδ
Lattice parameters	*a, b, c, α, β, γ*
Profile R-factor	R_p
Weighted profile R-factor	R_{wp}
Goodness of fit	GOF
X-ray diffraction	XRD
Scanning electron microscopy	SEM
Secondary electron	SE
Backscattered electron	BSE
Energy dispersive X-ray spectroscopy	EDS
X-ray fluorescence spectroscopy	XRF
Particle size distribution	PSD
Attenuated total reflectance Fourier transform infrared spectroscopy	ATR-FTIR
Inductively coupled plasma atomic emission spectroscopy	ICP-AES
Thermogravimetric and differential thermal analysis	TG-DTA

Coefficient of thermal expansion	CTE

Chapter 1 Introduction

This chapter mainly includes the basic knowledge which benefits the understanding of research results reported in this thesis. The applications and typical fabrication process of the low temperature co-fired ceramics (LTCC) are firstly introduced. Then the key technical requirements for LTCC materials, involving the low sintering temperature, the compatibility with electrodes and the dielectric properties, are addressed. After that, the current research progress of LTCC materials, especially those are made of the amorphous phase and ceramic, are summarized. A brief introduction to the thermal expansion and shrinkage phenomena of LTCC materials are also given since they are critical for the commercial use of LTCC devices. Finally, the motivation and outline of this thesis are briefly stated.

1.1 Applications of LTCC technology

LTCC technology, with which the passive components and conductive patterns can be embedded into stacked ceramics sheets, has attracted more and more attention in the past two decades. Thanks to the low sintering temperature, excellent electrical properties and unique three dimensional structure, it has been widely applied in microwave devices, sensors and micro-energy systems. For example, an aperture-coupled stacked patch microstrip antenna based on LTCC technology, as shown in Fig. 1-1a, has been reported for the upcoming 5G communication.[1, 2] To further minimize the attenuation of the millimetre wave in transmission, the phased array antenna based on LTCC technology, which can behave as the directional antenna, is also designed to establish stable point-to-point communication between terminal devices and base stations.[3, 4] In addition, Ma M. et al. also developed a novel wireless gas sensor for NO_2 in Fig. 1-1b by LTCC technology, in which the resistance and capacitance of LTCC template changes once the NO_2 gas molecules absorbed on the SnS_2 surface.[5] The detection limit of this sensor reaches as low as 0.6ppm even in the air. Besides, Goldberg A. et al. designed a fuel cell based on a micro energy system in Fig. 1-1c with a nominal power of less than one watt by LTCC technology,[6] which offers a high efficient and long-term stable way for hydrogen storage.

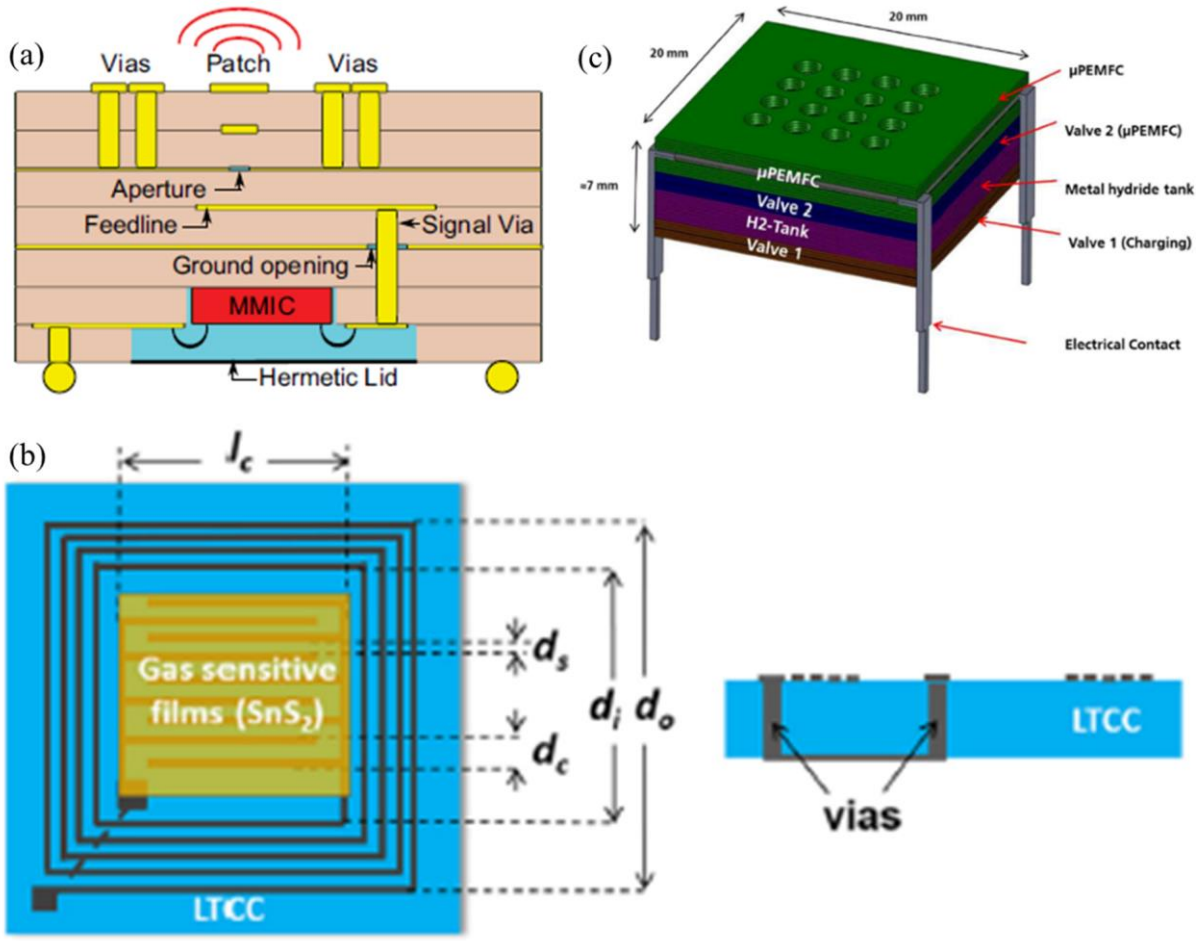

Fig. 1-1 (a) Aperture-coupled stacked patch microstrip antenna using LTCC technology (Reproduced from Bhutani A. et al[1]); (b) Schematic representation of the NO_2 gas sensor based on LTCC technology (Reproduced from Ma M. et al[5]); (c) Fuel cell system based on LTCC technology (Reproduced from Goldberg A. et al[6]);

More importantly, the LTCC technology is also extremely popular in the integration and device miniaturization field. The electronic components in a device can be classified into active components (transistors) and passive components (resistors, capacitors or inductors) depending on whether they can introduce the power gains.[7] The integration of active components has been greatly improved with the support of semiconductor technology in the past decades.[8] However, in real devices, the passive-to-active component ratio normally is higher than 10:1 and this ratio remains growing.[9, 10] Such a large number of passive components makes it still a challenge for packaging and device down-scaling.

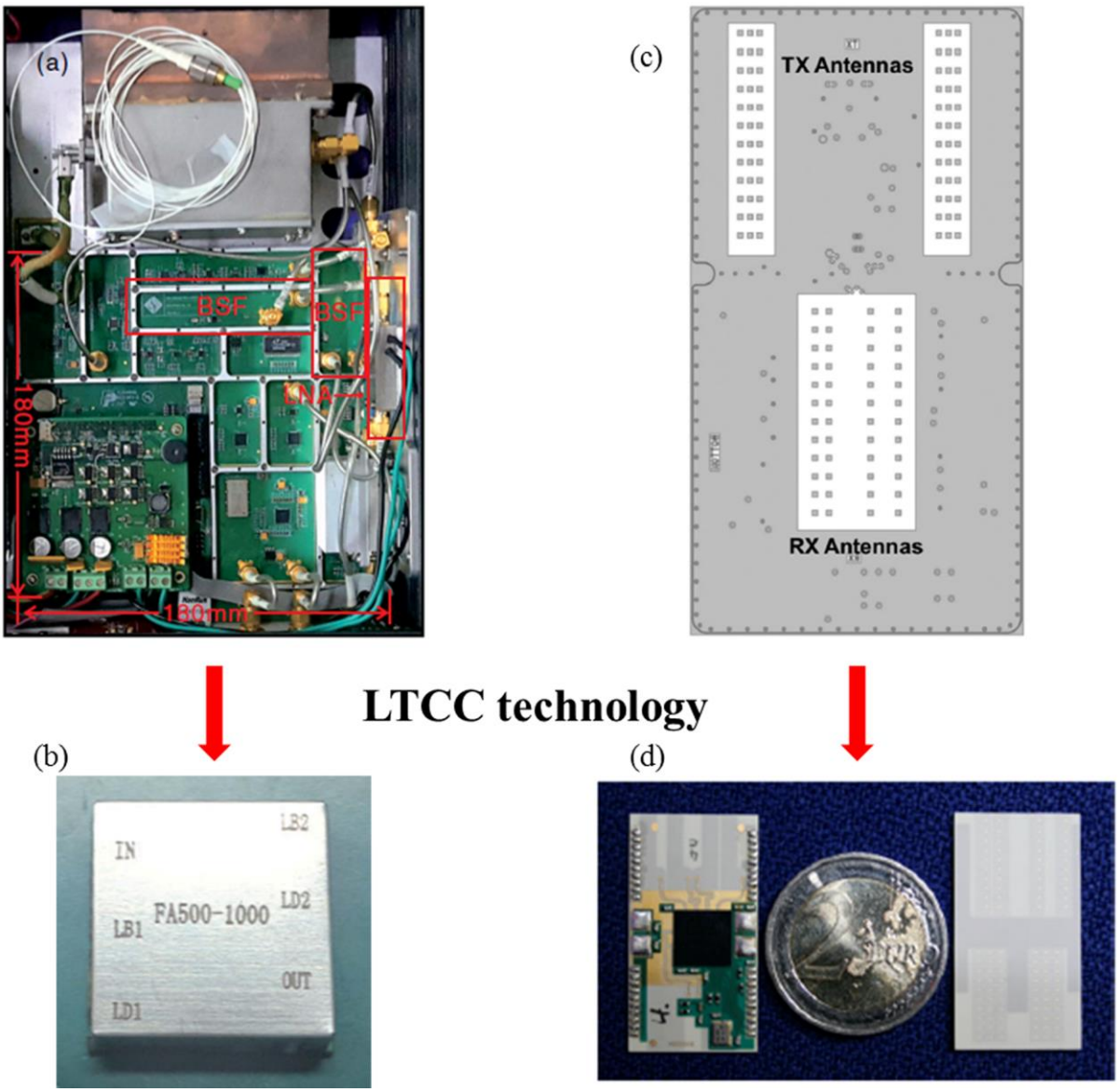

Fig. 1-2 Examples of integration and device miniaturization by LTCC technology, where (a) & (b) are reproduced from Jiang W. et al.[11] and (c) & (d) are reproduced from Sickinger F. et al.[12]

LTCC technology has shown overwhelming advantages in massive passive components packaging field benefiting from its unique three-dimensional structure. For example, Fig. 1-2a presents a typical single photon detector in 2012. The total size of the avalanche exaction circuit inside, as marked by three red rectangular regions, is ~5000mm^2. In 2017, Pan J. and co-workers have successfully integrated the circuit into a smaller module, as present in Fig. 1-2b, with area of 15mm×15mm by LTCC technology.[11] This size is only 4.5% of that in

conventional modules. Besides this, LTCC technology also makes a big difference in automobile field. The fully 360 °detection around a vehicle is highly demanded to develop the autonomous cars. This requires more radar systems to be involved for additional positions, such as B-pillars and side skirts, where the installation space is very limited. Sickinger F. et al[12] has successfully reduced the dimension from 90mm ×55mm to 33mm ×18mm by the LTCC technology, as shown in Fig. 1-2c and Fig. 1-2d, which is only 12% of that in the conventional radars.

1.2 The fabrication process of LTCC modules

The fabrication process of the LTCC modules is further described below in order to give readers a more visualized idea about LTCC technology.

In industry production, the LTCC modules are generally fabricated by the tape casting method as shown in Fig. 1-3. Initially, a slurry mixture of raw materials and organic solvents is cast under the "doctor blades" to obtain a tape with certain thickness. Then holes or vias are mechanically punched on the dried tapes and then filled with conductive pastes. After that, the designed conductive patterns are printed on the tapes using the screen printing method. Finally, the ceramic sheets are stacked, laminated and co-fired followed by final inspection.[13, 14] With this method, passive components can be integrated into different layers of the module, leaving more rooms on the surface for other components. In addition, it's compatible with metals having low conductor loss and low resistance, which endows itself the merit of rapid signal transmission and high density mounting.

In the fabrication process, the organics have played an important role in forming of the green tapes. The composition of organics is rather complicated and it generally contains binders, plasticizers, dispersing agents, antifoaming agents, as well as surface treatment coupling agents. In detail, the binders and the plasticizers are used for improving the formability and rheological properties of the slurry, as well as the strength of the green tapes. To avoid agglomeration, the dispersing agents are added to control the pH of the slurry and the charge of the particle surface. The antifoaming agents and surface treatment coupling agents are able to prevent the foam in

the slurry and improve wettability of ceramic powder by lowering its surface tension, respectively.[15] The amount of the organics and the ratio of each component inside are highly depended on the LTCC materials.[16, 17] This means the specific organics should be appropriately designed according to LTCC materials. More importantly, these organics should be completely eliminated after firing because any residual organics would cause performance degradation. In view of this, it would be better to use the organics as little as possible.

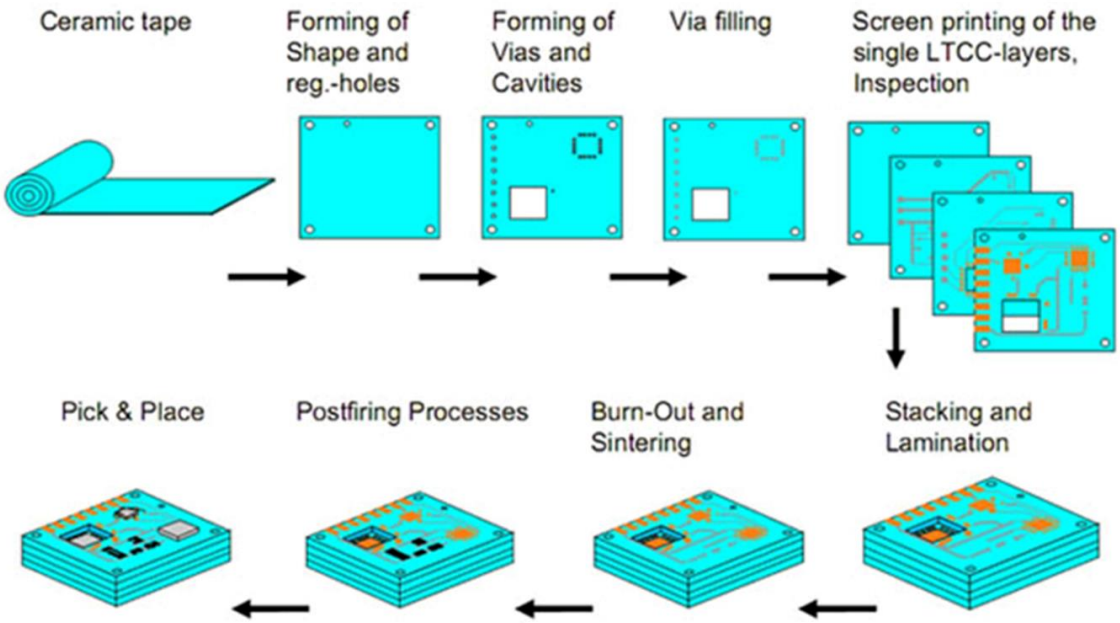

Fig. 1-3 A typical flowing diagram of tape casting method for preparing LTCC modules.[18]

The main target of this project is in the development of LTCC materials, so the solid-stated ceramic route, where the raw materials are directly pressed into pellets and sintered, is employed to achieve the intrinsic performances of the materials. When the comprehensive performances have been characterized and meet the requirements, the developed compositions will be submitted to our industry partner for industry production using tape casting method. But the organic binder is involved when checking the compatibility with silver electrode in this thesis because the granulated particles can form more compacted pellets to prevent the diffusion of silver paste before sintering.

1.3 Key technique requirements for LTCC materials

For commercial application, there are some key technique requirements for the LTCC materials, especially the low sintering temperature, compatibility with electrodes and suitable dielectric properties. In this section, we will give an introduction about these characteristics.

1.3.1 Low sintering temperature and compatibility with electrode

The sintering temperature, on one hand, stems from the limitation of melting points of co-fired electrodes. Historically, the LTCC technology is evolved from the high temperature co-fired ceramics (HTCC) technology, where alumina tapes were co-fired with Mo or W electrodes at 1600^{o}C.[19] Until 1980s, motived by increasing the speed of computer and high density mounting, finer electrode wire was proposed.[15] However, when the Mo or W electrode wire gets finer, the resistance increases and conspicuous attenuation of signals occurs. Thus, metals with lower electrical resistivity have been introduced from then on. As shown in Fig. 1-4, Au, Cu and Ag possess the lowest resistivity among the commonly used electrodes. In addition, the melting point of silver electrode is about 961^{o}C, so the raw materials should not be sintered at temperature higher than 900^{o}C, otherwise the designed conductive patterns on the ceramic sheets would be destroyed. This sintering temperature could be slightly adjusted by using other electrodes, such as copper or gold whose melt points are about 1000^{o}C. Considering the high cost of Au and easy oxidation of Cu in the air environment, the Ag is the most widely used electrode in commercial LTCC application.

On the other hand, it is worthwhile pointing out that sintering temperature is not the lower, the better. As mentioned in section 1.2, organics, such as binders or plasticisers, are added in industry production process of LTCC tapes. It is reported that the residual carbon after sintering should be controlled below 300ppm, otherwise, it would cause adverse effect on the dielectric performance.[20] The sintering temperature below 800^{o}C will be too low to remove such trace amount of organics.

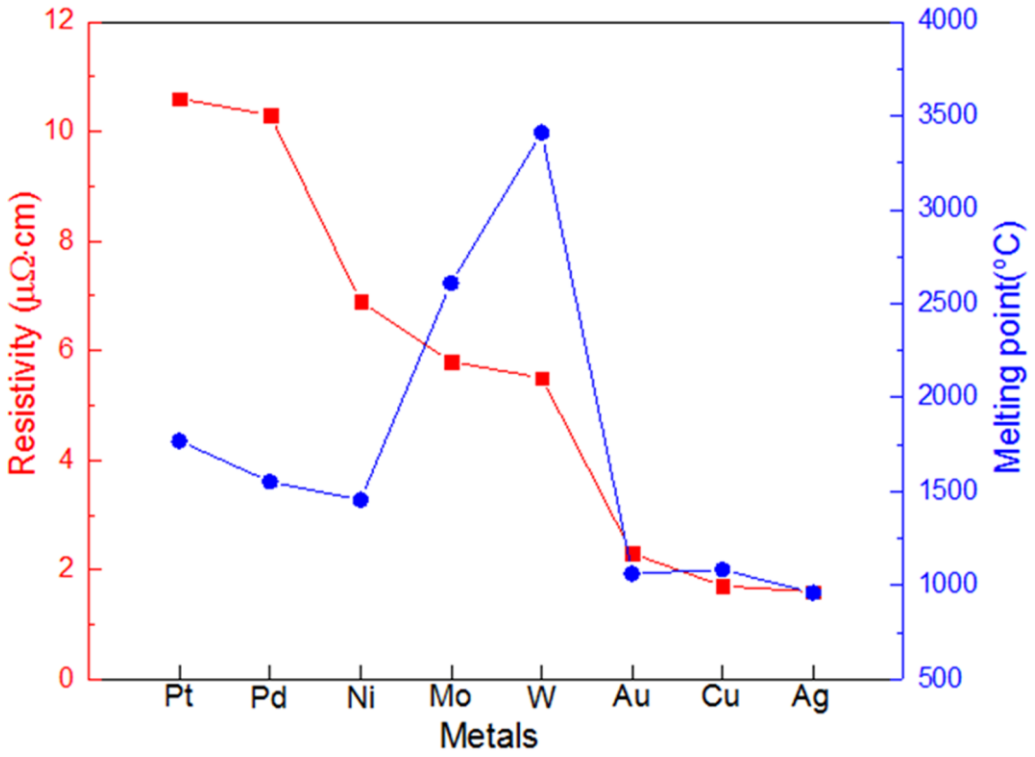

Fig. 1-4 Resistivities and melting points of common metal electrodes (Data are collected from Imanaka Y. and Chance D. A. et al[15, 21]).

Even in the range of sintering temperature, the LTCC materials must be compatible with electrode because any reaction or diffusion between them can degrade the device performance. Generally, the light brown colour on the surface of sintered sample can be found if the diffusion happens during sintering.[22] To be more precise, this compatibility is confirmed by checking the concentration of the electrode atom along the interface in the cross section based on energy-dispersive X-ray spectroscopy (EDS) characterization.[23]

As a result, the developed samples for LTCC application should have mentioned characteristics, that is, sinterable between 850°C and 900°C and compatible with silver electrode. Besides these, the developed sample should have well densified micro-structure as the ceramic after sintering. Any deficiencies, such as pores and cracks, are detrimental to the mechanical strength and dielectric performance of the samples to work as a packaging substrate.

1.3.2 Dielectric properties

For conductors and semiconductors, electrons can move under the external electric field and form electron current. In contrast, positive and negative charges of atoms or molecules are strongly bonded in the forms of covalent bond or ionic bond in the dielectric materials and cannot run away. Under the electric field, they can have a displacement at small scale to create a dipole. In terms of the dielectric materials, there are mainly four polarization mechanisms contributing to the dielectric as follows[24-27]:

(1) Electronic polarization refers to the shift in gravity centres of electron clouds and atom nucleus.

(2) Ionic polarization arises from the displacement of the cations with regard to the anions.

(3) Dipole orientation relates to orientation change of the polar molecules under applied electric field. For the glass, it comes from the dipoles made up of the modifier oxides and non-bridging oxygen.

(4) Space charge polarization is associated with the charges that accumulate in the vicinity of electrode, grain boundaries or the interfaces between different phases in the composites.

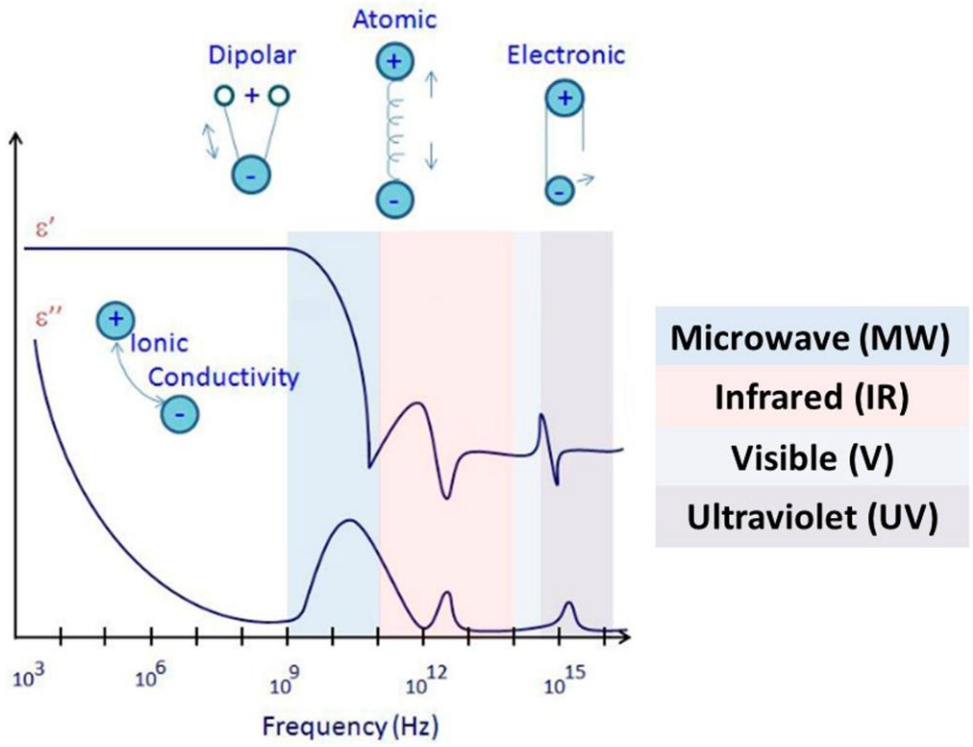

Fig. 1-5 Polarization mechanisms of dielectric materials over a wide range of frequencies. The figure is reproduced from Khaled D. E. et al[25].

The relation between the polarization (P) and dielectric constant of the material (ε_r) can be described as $P=\varepsilon_0(\varepsilon_r-1)E$, where E is the electric field, and ε_0 is the permittivity of free space.[28, 29] Thus, the dielectric constant is a measure of the polarizing effect under the external electric field.[25]

For the LTCC composite, the dielectric constant, also known as relative permittivity, can be empirically described by the dielectric constant and volume fraction of each phase, that is $\log \varepsilon_r = \Sigma v_i \log \varepsilon_i$, where ε_r represents for the dielectric constant of the composite, the v_i is volume fraction and ε_i is the relative permittivity of each phase, respectively.[30] So in many cases the sintering temperature plays a dominant role in controlling the dielectric properties due to different crystalline phases forming at certain temperature.

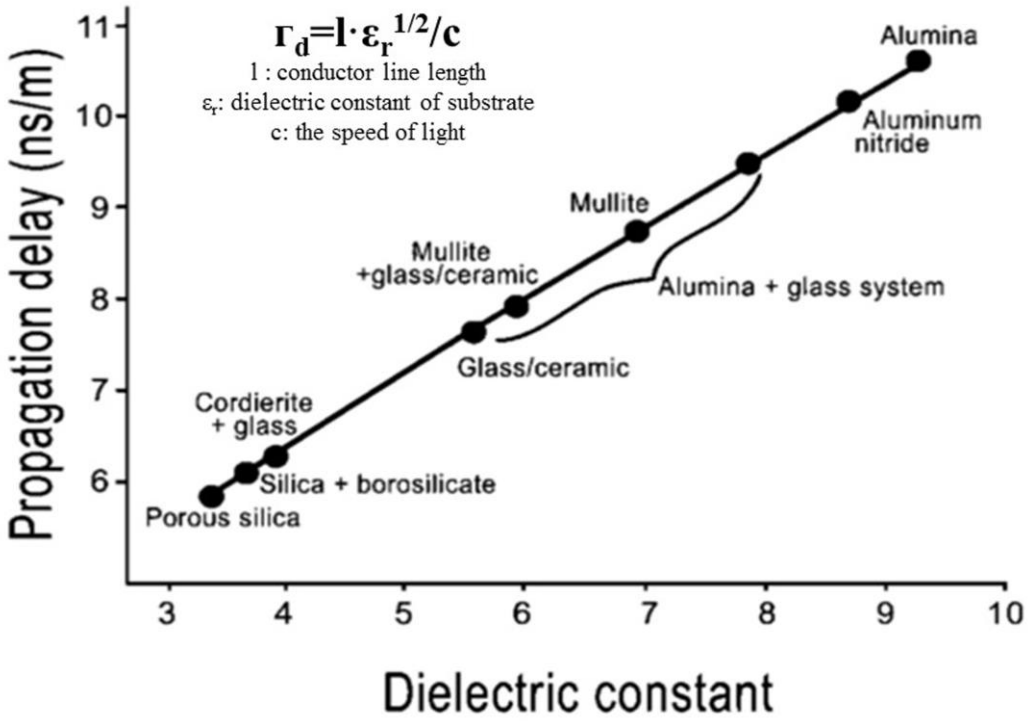

Fig. 1-6 Relationship between signal propagation delay and dielectric constant in the case of ceramic package. The figure is reproduced from Sebastian M. T. et al[31].

The dielectric constant of a specific LTCC material determines its application. Generally, dielectric materials with permittivity in the range from 4 to 12 are used for substrate layers while those with higher permittivity are mainly used as capacitor layers or resonating structures.[31] And as illustrated in Fig. 1-6, the signal propagation delay is proportional to the square root of the dielectric constant of the ceramic in the case of ceramic packages.[20, 32, 33] As a result, the materials with lower dielectric constant are in favour of rapid signal transition.

Dielectric loss refers to the amount of electric energy lost through heat in the dielectric materials when an external electric field is applied. And some loss mechanisms, such as conduction loss, dipole relaxation loss, distortion loss and ion vibration loss mechanisms have been recognized in LTCC materials.[15, 24, 34] On balance, such complicated loss mechanisms make it a challenge to control the dielectric loss, but some strategies have been proved effective. For example, Imanaka Y. et al. have derived the equation $\tan\delta = (\gamma/\omega_T^2)\,\omega$ from the one-dimensional lattice vibration model, where ω_T is the resonating angular frequency of the optical mode of lattice vibration transverse waves, γ and ω are respectively attenuation constant and angular frequency. They point out it is effective to use raw materials with high purity to achieve low dielectric loss because the presence of impurities will increase γ.[15] In addition, for glass/ceramic composites, the dielectric loss mainly comes from migration losses in the glass, which are caused by the movement of mobile ions, such as Na^+ and K^+.[35] If alkali metal ions in lossy glass are co-doped with different alkali or alkaline metal ions, the loss can be reduced since the mobility of alkali ions will be hindered.

As illustrated in Fig. 1-5, the dielectric properties show great dependence on frequency. The dielectric properties of reported LTCC materials are measured under different frequency, so it is hard to make solid comparison with each other. In this project, we concentrate on the dielectric properties at 1MHz.

1.4 LTCC materials

Considering the key technique requirements of LTCC materials, especially the limitation of sintering temperature, the selection of materials for LTCC application is few because most

conventional electro-ceramics have to be sintered above 1000°C. To develop the suitable materials, on one hand, the researchers are looking for materials with intrinsic low sintering temperature. On the other hand, some methods, such as addition of sintering aids or glasses with low softening temperature, are employed to reduce the sintering temperature. Although the method using raw materials with small particle size to reduce the sintering temperature is also reported, it is not practical in the industry tape casting method because the large surface area will require more organics.[36]

According to the two strategies mentioned above, the current reported LTCC materials can be classified into three groups as presented in Fig. 1-7. Group one is the tellurium oxide based materials that have intrinsic low sintering temperature.[37] However, their toxicity and incompatibility with silver electrode have hindered the way to commercial application.[38] It is worthwhile pointing out that there are also some compounds with specific structures, such as $NaAgMoO_4$ with spinel-like structure,[39] are reported can be sintered below 800°C. Yet it is hard to apply them to the industry tape casting process because such low sintering temperature would prevent the complete evaporation of the organics during firing. Group two covers the materials with low processing temperature, such as MNb_2O_8 (M=Zn, Ca, Ba, Mn) mixed with sintering aids (V_2O_5, CuO, Bi_2O_3, B_2O_3).[31, 40] But most of these materials have the dielectric constant higher than 20, which is not in favour of rapid signal transmission as ceramic packaging substrate. The third group is related to the glass and ceramics composite and it can be further divided into two subgroups depending on the amount of glass in the raw material. One subgroup is glass-ceramic composite which starts with full glassy phase and then gets crystallized during sintering.[41, 42] For this kind of materials, the degree of crystallization (~90%) should be finely controlled, otherwise it would result in poor dielectric loss or mechanical properties.[31, 43] Some compounds, such as ZrO_2 and TiO_2, can be further introduced as the nucleating agent to improve the crystallization.[44, 45] Another subgroup is based on glass/ceramic composite, which consists of a dielectric material with high sintering temperature and the glass phase with low softening temperature. For example, alumina, with relative permittivity of 10, quality factor ($1/\tan\delta$) of 680000 and sintering temperature as high as 1550°C, is a good basic dielectric material.[46] The compositions of glass phases used in reported

literatures are quite scattered but generally with softening temperature of ~800°C.[15, 47] In this composite, the overall performance can be modulated by selecting various ceramics or changing the ratio between glassy phase and ceramic. Depending on the reactivity between the glass and ceramic, the glass/ceramic composite can be further classified into reactive and non-reactive systems.[48] In the reactive system, the densification process has been described by three stages, that is, dissolution and particle rearrangement, precipitation, as well as solid state sintering.[49] As shown in Fig. 1-7, the glass phase melts into viscous liquid and quickly fills the pores in the first stage. Driven by capillary pressure, the particles are also rearranged and turn into a closer packed structure. In the second stage, the distance between particles in the packed structure is further decreased since the solubility at the contact points between particles is larger than that at other surfaces. This solubility leads to the transfer of material away from the contact points and precipitation in the form of larger particles.[50] In the final stage, the densification process becomes slow down since the relative rigid skeleton has formed. The grain growth through Ostwald ripening kinetics is the typical phenomenon occurring in this stage.[51] While in terms of the non-reactive sintering, the densification process is mainly happened in the first stage and little dissolution of ceramic in glass is happened.[52]

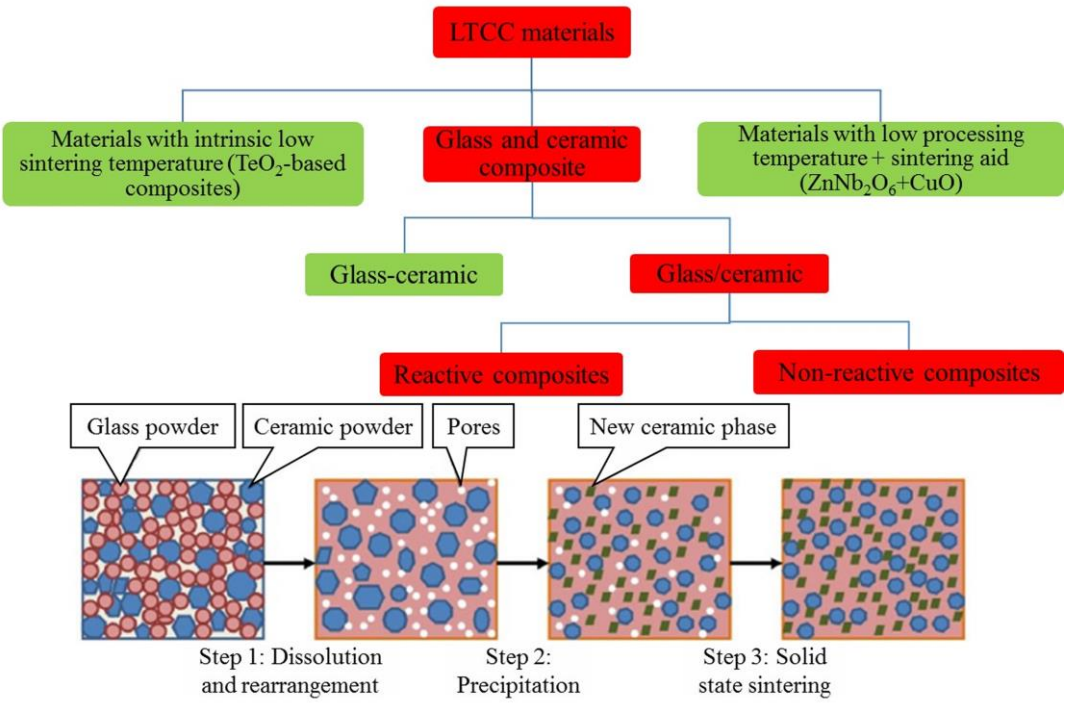

Fig. 1-7 Summary and classification of reported LTCC materials. The inserted figure about the

densification process is reproduced from Zhou J.[24]

Among reported LTCC materials, the glass/ceramic composites are of the highest practical value benefiting from its flexibility in performance tuning. Herein the glass composition, glass making method and the selection of ceramic are of significant importance.

In terms of the glass composition, the pure amorphous SiO_2 has intrinsic high transition temperature (~2000°C) and high viscosity. Thus when used in LTCC materials, it is often doped by other oxides, as shown in Fig. 1-8, to decrease transition temperature and viscosity. These oxide dopants comprise oxides that form glass network and modifier oxides that break the network.[53] For example, B_2O_3, a typical substance to forms glass network structures, mainly reduces viscosity of glass but with very small influence on thermal expansion or chemical durability.[15] Modifier oxides include alkali metal and alkaline earth metal oxides, such as Na_2O and CaO. Alkali oxides can break some rigid Si-O-Si bonds in the continuous networks and form non-bridging oxygen.[54] The bond between Na and non-bridging oxygen is relatively weak, so the alkali ions are weakly held in the interstices of the glassy network.

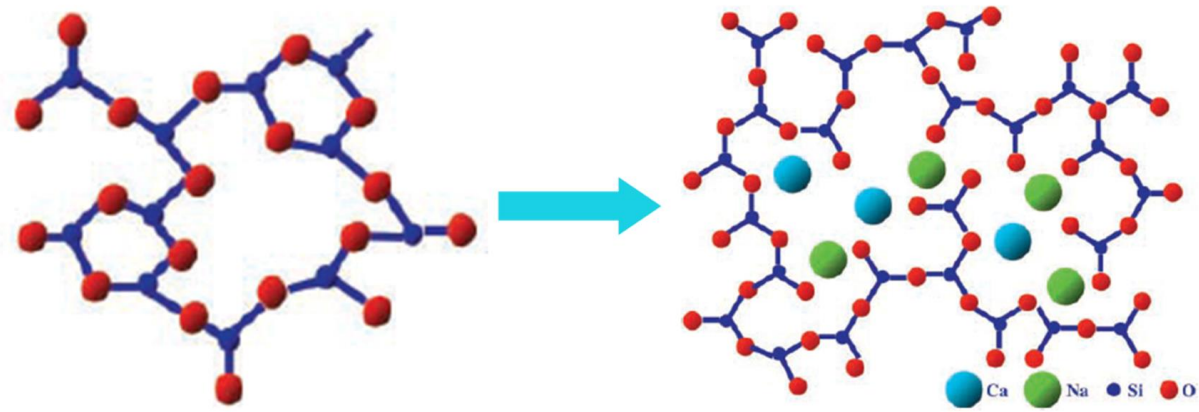

Fig. 1-8 Structure of the pure amorphous silica glass and multi-components silica glass, which are reproduced from Vallet-Reg íM.[55]

These modifier ions in the glass network are easy to move under high frequency fields, consequently depleting energy and giving rise to dielectric loss. It is reported that when two or

more different alkali metals are co-doped, this mobility would be supressed because that they prefer to accumulate around the non-bridging oxygen, leading to relatively stronger bonding. This is so called "mixed alkali effect".[56, 57] Besides, it is reported alkaline earth metal oxides can also prevent the migration of alkali ion. For example, when Na is co-doped with Ca, Ca tends to enter modifier-rich regions in the glass and contributes to the formation of percolation channels together with Na ions. However, the Ca-O bond is stronger than the Na-O bond, which means the calcium ions are less mobile in the structure and thus obstruct the Na diffusion channels.[58, 59]

No matter what composition of the glass is used, it is inevitable to fabricate the glassy phase before developing the LTCC materials based on glass/ceramic composites. As other research has reported, there are mainly three methods to fabricate the glass. The most widely used method is melt-quench method, and as the name implies, it melts the raw components of glass at high temperature (~1500^{o}C) and then quenches in water to reserve the amorphous structure.[60, 61] Most glass compositions can be synthesized by this method. But it lacks of control on the volatilisation of some constituents, such as B_2O_3, at high melting temperature and some undesired crystal nucleations due to change of quench rate.[62] These labile factors have made it struggle to reproduce the same performance in industry production. To make the things even worse, some glass compositions still cannot be prepared by this method. For example, CaO-SiO_2 glass has not been successfully synthesized by this method because of the presence of the stable liquid-liquid immiscibility region in this system.[63]

To make up these deficiencies, Abhilash P. et al. have made a specific glass (10% ZnO-2% B_2O_3-8% P_2O_5-80%TeO_2, denote as ZBPT glass) without quench process.[64] No matter the ZBPT glass synthesized by the conventional melt-quench method or the quench-free method, the designed ZBPT glass/Sr_2ZnTeO_6 (SZT) composite shows similar performance. But there is no support that this method can be applied to other glass compositions.

Alternatively, the multi-components glass can also be synthesized using the sol-gel method. With this method, the glass can be synthesized at much lower temperature,[65] which can definitely suppress the evaporation of glass components. And the quench rate makes no

difference, so it is able to cool to the room temperature naturally. Furthermore, the above mentioned CaO-SiO_2 glasses, which failed to be synthesized by the melt-quench method, can also be synthesized by this way. Consequently, the sol-gel method could be applied to more glass compositions than the melt-quench method. However, this method has not been widely used in the LTCC development.

No matter which method is employed, the fabricated glass powders all show hump peak under X-ray powder diffraction (XRD) characterization due to lack of long range order in structure. Strictly speaking, glass refers to the solid achieved by the melt-quench method, while that synthesized by the sol-gel method is called amorphous phase. The sol-gel derived amorphous phases show similar physical properties with the glasses obtained from the melt-quench method, but the former shows higher energy and more uniform microstructure.[66, 67]

Ceramic is the equally important factor as the glass in the glass/ceramic based composite and its influence is also rather complicated. For example, ceramic with diverse particle size requires various amount the glass for densification process due to different specific surface area.[68] In addition, the ceramic would better have a good wetting behaviour with the glass to achieve well densified microstructure. This wetting behaviour can be characterized by the heating microscopy experiment.[69] A simple but effective criterion is to check whether there is any reaction happened between them based on XRD characterization, which also implies a good wetting behaviour.

The selection of the polymorphs of ceramic should be comprehensively considered. Take the alumina as an example. Actually it contains seven polymorphs and the most widely used one, with relative permittivity of 10, high quality factor ($1/\tan\delta$) of 680000, is the α-Al_2O_3 phase.[70] The polymorphs possess some similarities but more differences. For instance, quartz, cristobalite and fused silica, which are polymorphs of SiO_2, share the similar permittivity of ~4. But fused silica has the coefficient of thermal expansion of $0.5\times10^{-6}/^{o}C$, which is much smaller than that of quartz ($11\times10^{-6}/^{o}C$) and cristobalite ($50\times10^{-6}/^{o}C$).[69, 71] In addition, the cristobalite phase exhibits phase transformation at ~200^{o}C,[72-74] which will lead to unwanted thermal stress or mechanism damage during sintering.

In this project, we will mainly develop the LTCC materials based on the amorphous phase and ceramic composites. Herein the amorphous phases will be synthesized by sol-gel method to make up the deficiencies of melt-quench method. Also the various ceramics will be tried to develop LTCC materials with different dielectric constants. Besides these, we will also develop a composite which is fully composted of crystalline phases. Herein, the $KBSi_2O_6$ phase is synthesized by the solid state reaction and introduced to develop the LTCC materials. The advantage of this silicate is in that the B atom can be substituted by other trivalent cations, such as Al, under low temperature and this substitution can lead to good bonding behaviour in the sintered sample.[75, 76]

1.5 Thermal expansion

In real application, devices or chips are usually mounted on the top of the LTCC modules. So if coefficients of thermal expansion (CTE) of these two parts mismatch, a misfit strain will be produced, leading to electrical contact failure or substrate crack.[77] Generally, if the LTCC module would be mounted with silicon substrate, its CTE should be ~4 ppm/ ^oC. And it should be 7~9 ppm/ ^oC and 12~20 ppm/ ^oC when connected with alumina and printed circuit board, respectively.[78] In this project, the developed samples will possess matched CTE with these substrates.

Similar with dielectric properties of the composite, the CTE of LTCC composite also depends on constituents and their fraction. As a result, the CTE of the LTCC materials can be designed by controlling the phases present. As illustrated in Fig. 1-9, Qing Z. et al. have reported the addition of MgO to Li_2O-Al_2O_3-SiO_2 glass-ceramic composite can form $CaMgSi_2O_6$ phase in the sintered and thus modulate CTE from 1.06 ppm/ ^oC to 2.89 $\times 10^{-6}$ ppm/ ^oC so that the material is compatible with silicon chip.[79]

Except the matched value, the thermal expansion of the LTCC composite should be linear in any circumstance because any non-linear change will cause unwanted thermal stress or mechanism damage. For instance, if cristobalite phase, a polymorph of SiO_2, presents in the sintered composite, a non-linear change of the CTE in the range of 100^oC to 200^oC will happen

and destroy the connection reliability of the product.

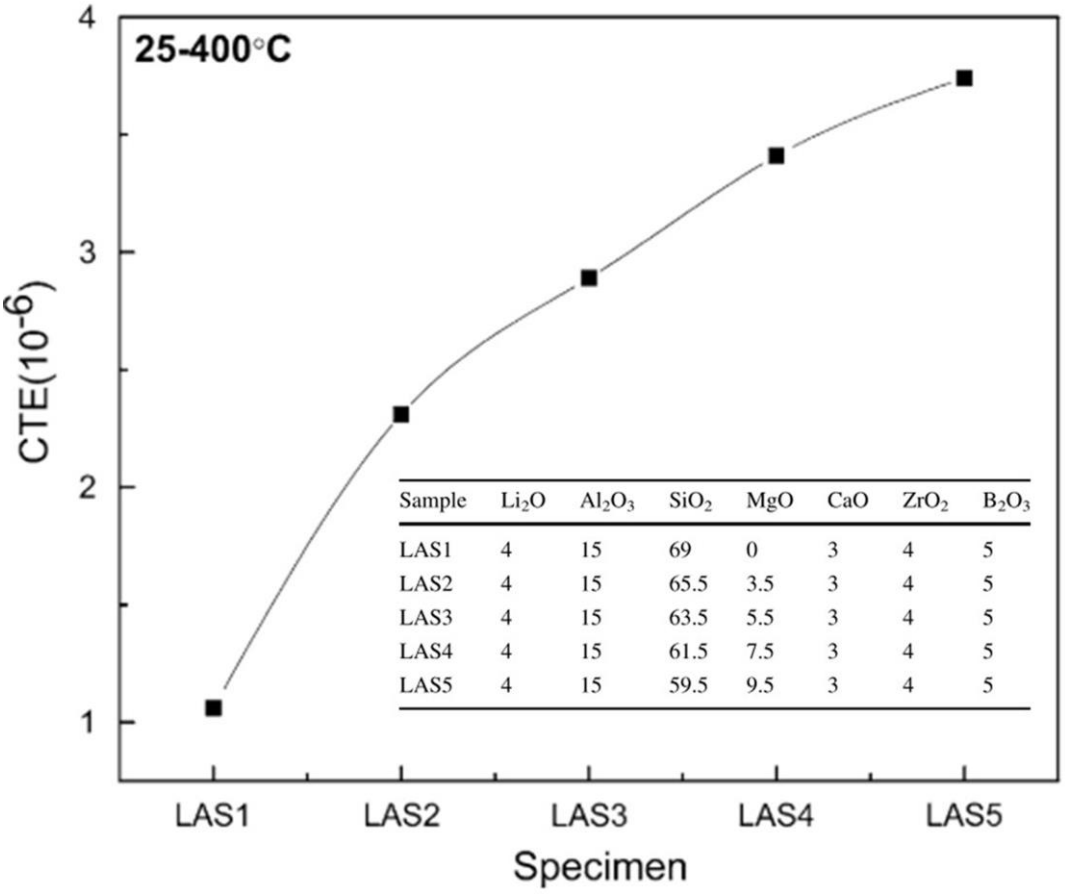

Sample	Li_2O	Al_2O_3	SiO_2	MgO	CaO	ZrO_2	B_2O_3
LAS1	4	15	69	0	3	4	5
LAS2	4	15	65.5	3.5	3	4	5
LAS3	4	15	63.5	5.5	3	4	5
LAS4	4	15	61.5	7.5	3	4	5
LAS5	4	15	59.5	9.5	3	4	5

Fig. 1-9 Modulation of the coefficients of thermal expansion (CTE) of Li_2O-Al_2O_3-SiO_2 glass by addition of MgO. The figure and inserted table are reproduced from Qing Z. et al[79].

1.6 Shrinkage phenomenon

The LTCC materials experience three dimensional shrinkage during sintering. Compared with the shrinkage in thickness direction (Z direction), that in XY plane is more important because it limits the number of embedded passive components and the size of vias, especially the adherence of conductive patterns on ceramics. In order to control XY shrinkage, the constrained sintering technologies, such as pressure assisted sintering (PAS), pressure less assisted sintering (PLAS), self-constrained sintering and the LTCC-Metal approach, are consequently proposed as the solutions.[80, 81] With these methods, the LTCC tapes are stacked with sacrificial tapes, as shown in Fig. 1-10, so that XY shrinkage is constrained by the in-

plane tensile stress arises from the interfacial friction. This can relieve or even eliminate the shrinkage in XY directions and result in a larger shrinkage taking place in Z direction.

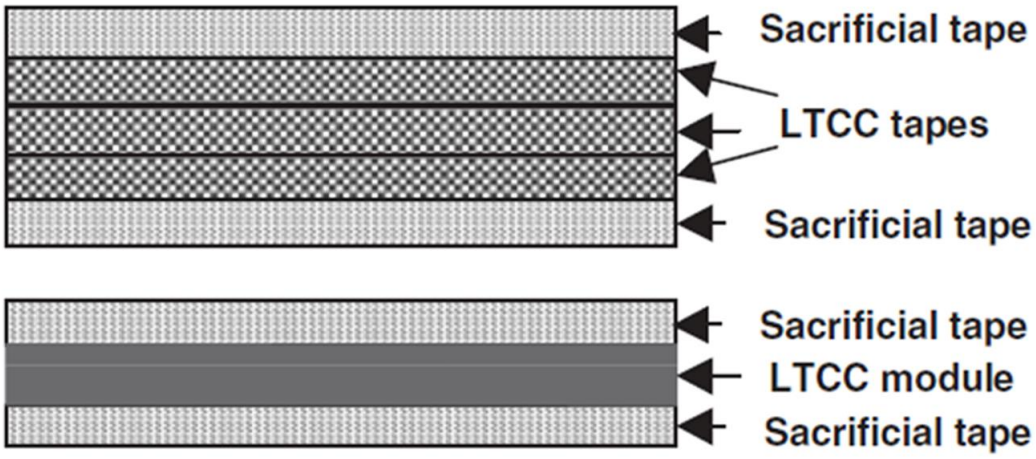

Fig. 1-10 LTCC tapes laminate with sacrificial tapes in the green state (above) and after sintering (below), which are reproduced from Rabe T. et al[80].

These constrained sintering methods are mainly implemented in the tape casting method. In this project, we concern the shrinkage match between the developed samples and co-fired Ag electrode more than the absolute value. It is acceptable as long as no any crack or delamination happened in the electrode/LTCC interface.

1.7 Motivation and outline of the thesis

The most important motivation of this project is to develop the dielectric materials for LTCC applications. Although some LTCC materials have been reported over the past decades, only a few of them are well-used in practical application. This is because it is difficult to balance many properties under such rigorous processing conditions. Our industry partner suggests the developed samples in this work to meet the performance requirements listed in Tab. 1-1. In detail, the developed materials have to be sinterable between 850^{o}C and 900^{o}C. The relative permittivity must be in the range between 4 and 12 (@1MHz) to work as the packaging substrate. And the dielectric loss need to be below 0.003 (@1MHz) for the sake of high fidelity

of signal. The coefficient of thermal expansion must match with common chip substrates, such as silicon, alumina or printed circuit board. What is more, the developed materials have to be compatible with silver electrode during sintering. With this performance, our industry partner can apply these materials directly to industry production using tape casting method.

Tab. 1-1 Target of the performance for the developed samples.

Performance requirements	
Sintering temperature	850~900 °C
Dielectric constant	4~12 @1MHz
Dielectric loss	≤0.003 @1MHz
Resistivity	$\geq 10^{12}$ Ω·cm @100V DC
Coefficient of thermal expansion	Match with silicon (4 ppm/ °C), alumina (7~9 ppm/°C) or printed circuit board (12~20ppm/ °C)
Compatibility	Compatible with silver electrode

Secondly, as mentioned in section 1.4, the glass/ceramic composites are of the highest practical value benefiting from its flexibility in performance tuning. Herein the glass making method is quite important. Except failure in fabricating some specific glass, it also lacks control of the evaporation and quench rate in the popular melt-quench method. And these deficiencies make the developed glass/ceramic materials work unsteadily in the industry production. In comparison, by the sol-gel method, the amorphous phases can be made at lower temperature and has no requirements on the quench rate. In particular, the specific $CaO\text{-}SiO_2$ glass, which has not been successfully synthesized by the melt-quench method, can also be synthesized using sol-gel method. As a result, it is worthy to try the sol-gel derived amorphous phases for LTCC application.

In addition, it is of great value to develop the dielectric materials with relative permittivity between 4 and 12 for flexibility in circuit design.[1, 2, 4] Based on the information from our industry partner, the materials with relative permittivity of ~8 are very popular in current consumer electronic market. And the materials with smaller dielectric constant (~5) are highly demanded in high-speed digital circuits as the signal propagation delay is proportional to the

square root of relative permittivity. Furthermore, application of those with higher dielectric constant (~11) in design of high frequency circuits is growing.[82] Therefore, there is a huge market prospect for the materials with various dielectric constant.

Finally, instead of adding amorphous phase to reduce the sintering temperature, many effects have been made to develop composite only consisted of crystalline phases for high frequency application. But currently reported amorphous phase-free composites are with relative permittivity higher than 20, which is not in favour of rapid signal transition as ceramic packaging substrates. Hence, it is anticipated to develop an amorphous phase-free composite with lower dielectric constant, especially that with relative permittivity of ~8, for LTCC application.

The thesis consists of the following chapters:

Chapter 1 is an introduction to the relevant background knowledge to this work.

Chapter 2 is an overview of the characterization methods involved in the project.

Chapter 3 is the development of samples with dielectric constant of 7~8 based on amorphous phases and Al_2O_3, where the amorphous phases are fabricated by sol-gel method.

Chapter 4 is the development of samples with relative permittivity of 5 and 11 based on the pure fused SiO_2 and ZrO_2 with amorphous phase, respectively.

Chapter 5 is the development of a composite only consisting of crystalline phases for LTCC application.

Chapter 6 is to summarize the main research outcomes and present an outlook on the potential continuing work of this thesis.

Reference

1. Akanksha Bhutani, Heiko Gulan, Benjamin Goettel, Christoph Heine, Torsten Thelemann, Mario Pauli, Thomas Zwick, 122GHz aperture coupled stacked patch microstrip antenna in LTCC technology. In *10th European Conference on Antennas and Propagation* IEEE: Davos, Switzerland, 2016.

2. Stefan Beer, Leonardo Pires, Christian Rusch, Jaska Paaso, Thomas Zwick, A 122GHz microstrip slot antenna with via-fence resonator in LTCC techology. In *6th European Conference on Antennas and Propagation (EUCAP)*, IEEE: Prague, Czech Republic, 2012; pp 1329-1332.

3. Kam, D. G.; Liu, D.; Natarajan, A.; Reynolds, S.; Chen, H.-C.; Floyd, B. A., LTCC Packages With Embedded Phased-Array Antennas for 60 GHz Communications. *IEEE Microwave and Wireless Components Letters* **2011,** *21* (3), 142-144.

4. Mingming Peng, Anping Zhao, LTCC based phased array antenna for 5G millimeter wave application in mobile device. In *2018 IEEE International Symposium on Antennas and Propagation & USNC/URSI National Radio Science Meeting*, IEEE: Boston, MA, USA, 2018; pp 245-246.

5. Ma, M.; Khan, H.; Shan, W.; Wang, Y.; Ou, J. Z.; Liu, Z.; Kalantar-zadeh, K.; Li, Y., A novel wireless gas sensor based on LTCC technology. *Sensors and Actuators B: Chemical* **2017,** *239*, 711-717.

6. Adrian Goldberg, Carsten Pohlmann, Lars Rontzsch, Christian Freitag, Ariel Thierry Tagne Sahal, Steffen Zieschel, Uwe Partschl, Highly efficient and long term stable micro fuel cell system based on ceramic multilayer technology. In *2016 6th Electronic System-Integration Technology Conference (ESTC)*, IEEE: Grenoble, France, 2016.

7. Glisson, T. H., *Introduction to circuit analysis and design*. Springer, Dordrecht: 2011.

8. Knickerbocker, J. U.; Andry, P. S.; Dang, B.; Horton, R. R.; Interrante, M. J.; Patel, C. S.; Polastre, R. J.; Sakuma, K.; Sirdeshmukh, R.; Sprogis, E. J.; Sri-Jayantha, S. M.; Stephens, A. M.; Topol, A. W.; Tsang, C. K.; Webb, B. C.; Wright, S. L., Three-dimensional silicon integration. *IBM Journal of Research and Development* **2008,** *52* (6), 553-569.

9. ULRICH, R. K., *Integrated Passive Component Technology*. Wiley-IEEE Press: 2003.

10. L.J. Golonka, K.-J. Wolter, A. Dziedzic, J. Kita, L. Rebenklau, Embeded passive components for MCM. In *24th International Spring Seminar on Electronics Technology. Concurrent Engineering in Electronic Packaging. ISSE 2001. Conference Proceedings (Cat. No.01EX492)*, IEEE: Calimanesti-Caciulata, Romania, Romania, 2001.

11. Wen-Hao Jiang, Jian-Hong Liu, Yin Liu, Ge Jin, Jun Zhang, Jian-Wei Pan, 1.25GHz sine wave gating InGaAs/InP single photo detector with a monolithically integrated readout circuit. *Optics Letter* **2017,** *42*, 5090-5093.

12. Sickinger, F.; Weissbrodt, E.; Vossiek, M., 76–81 GHz LTCC antenna for an automotive miniature radar frontend. *International Journal of Microwave and Wireless Technologies* **2018,** *10* (5-6), 729-736.

13. Y. C. Chan and G. Y. Li, Fabrication and characterization of multilayer capacitors buried in a low temperature co-fired ceramic substrate. *Active and Passive Elec. Comp.* **1998,** *20*, 215-224.

14. Richard E. Mistler, Eric R. Twiname, *Tape Casting: Theory and Practice*. The American Ceramic Society: 2000.

15. Imanaka, Y., *Multilayered low temperature cofired ceramics technology*. Springer US: 2005; p 229.

16. Liu, M.; Zhou, H.-q.; Zhu, H.-k.; Yue, Z.-x.; Zhao, J.-x., Tape casting of borosilicate glass/Al_2O_3 composites for LTCC substrate with various relative molecular masses of PVB. *Journal of Central South University* **2013,** *20* (1), 37-43.

17. D. Hotza, P. Greil, Review: aqueous tape casting of ceramic powders. *Materials Science and Engineering* **1995,** *202*, 206-217.

18. Complete Solutions in Ceramic Tech for Advanced Electronics. http://www.imc-india.com/content/complete-solutions-ceramic-tech-0.

19. A. J. Blodgett, D. R. Barbour, Thermal conduction module: A high-performance multilayer ceramic package. IBM: IBM Journal of Research and Development, 1982; pp 30-36.

20. Turnmala, R. R., Ceramic and glass-ceramic packaging in the 1990s. *J. Am. Ceram. Soc.* **1991,** *74*, 895-908.

21. Dudley A. Chance, David L. Wilcox, Metal-ceramic constraints for multilayer electronic packages. *Proceedikgs of the IEEE.* **1971,** *59*, 1455-1462.

22. Hsi, C.-S.; Chen, Y.-R.; Hsiang, H.-I., Diffusivity of silver ions in the low temperature co-fired ceramic (LTCC) substrates. *Journal of Materials Science* **2011,** *46* (13), 4695-4700.

23. Ma, M.; Liu, Z.; Zhang, F.; Liu, F.; Li, Y.; Bordia, R., Suppression of Silver Diffusion in Borosilicate Glass-Based Low-Temperature Cofired Ceramics by Copper Oxide Addition. *Journal of the American Ceramic Society* **2016,** *99* (7), 2402-2407.

24. Zhou, J., Towards rational design of low-temperature co-fired ceramic (LTCC) materials. *Journal of Advanced Ceramics* **2012,** *1* (2), 89-99.

25. El Khaled, D.; Castellano, N. N.; Gazquez, J. A.; Perea-Moreno, A. J.; Manzano-Agugliaro, F., Dielectric Spectroscopy in Biomaterials: Agrophysics. *Materials (Basel)* **2016,** *9* (5).

26. Newnham, R. E., *Properties of materials: anisotropy, symmetry, structure*. Oxford University Press: 2004.

27. Dakin, T. W., Conduction and polarization mechanisms and trends in dielectrics. *IEEE Electrical Insulation Magazine* **2006,** *22* (5), 11-28.

28. Donald R. Askeland, Pradeep P. Fulay, Wendelin J. Wright, *The science and engineering of materials*. 6 ed.; Cengage Learning: 2011.

29. Cardarelli, F., *Materials handbook*. Springer, London: 2008.

30. Chung-Lun Lo, Jenq-Gong Duh, Bi-Shiou Chiou, Wen-Hsi Lee, Low-temperature sintering and microwave dielectric properties of anorthite-based glass-ceramics. *J. Am. Ceram. Soc.* **2002,** *85(9)*, 2230 –35.

31. Sebastian, M. T.; Jantunen, H., Low loss dielectric materials for LTCC applications: a review. *International Materials Reviews* **2013,** *53* (2), 57-90.

32. Schwartz, B., Review of multilayer ceramics for microelectronic packaging. *Journal of Physics and Chemistry of Solids* **1984,** *45*, 1051-1068.

33. Klaus Kupfer, Eberhard Trinks, Simulations and experiments for detection of moisture profiles with TDR in a saline environment. In *Electromagnetic Aquametry*, Springer, Berlin, Heidelberg: 2005; p 530.

34. Scholze, H., *Glass: nature, structure, and properties*. Springer-Verlag New York: 1991; p 454.

35. Chen, X.; Zhang, W.; Bai, S.; Du, Y., Densification and characterization of SiO_2-B_2O_3-CaO-MgO glass/Al_2O_3 composites for LTCC application. *Ceramics International* **2013,** *39* (6), 6355-6361.

36. Qingxue Zhang, Xiaojun Luo., Wenlan Li, Hanrui Zhuang, Dongsheng Yan, Tape casting of AlN/glass composites for LTCC substrate. *Journal of Materials Science* **2003,** *38*, 1781– 1785.

37. M. Udovic, M. Valant, D. Suvorov, Dielectric characterisation of ceramics from the TiO_2-TeO_2 system. *Journal of the European Ceramic Society* **2001,** *21*, 1735–1738.

38. Rajesh, S.; Jantunen, H.; Letz, M.; Pichler-Willhelm, S., Low Temperature Sintering and Dielectric Properties of Alumina-Filled Glass Composites for LTCC Applications. *International Journal of Applied Ceramic Technology* **2012,** *9* (1), 52-59.

39. Di, Z.; Li-Xia, P.; Ze-Ming, Q.; Biao-Bing, J.; Xi, Y., Novel ultra-low temperature co-fired microwave dielectric ceramic at 400 degrees and its chemical compatibility with base metal. *Sci Rep* **2014,** *4*, 5980.

40. Dong-Wan Kim, Kyung Hyun Ko and Kug Sun Hong, Influence of copper(II) oxide addition to zinc niobate microwave ceramics on sintering temperature and dielectric properties. *J. Am. Ceram. Soc.* **2001,** *84*, 1286–1290.

41. Jau-Ho Jean and J.-I. Shen, Binary crystallizable glass composite for low dielectric multilayer ceramic substrate. *Japanese Journal of Applied Physics* **1996,** *35*, 3942-3946.

42. A. G. Gregory, T. J. Veasey, The crystallization of cordierite glass. *Journal of Materials Science* **1971,** *6*, 1312-1321.

43. Katsumasa Yasukawa, Yoshitake Terashi and Akira Nakayama, Crystallinity analysis of glass-ceramics by the Rietveld method. *J. Am. Ceram. Soc.* **1998,** *81*, 2978-82.

44. Li, B.; Duan, D.; Long, Q., Influences of ZrO_2 on microstructures and properties of Li_2O–Al_2O_3–SiO_2 glass–ceramics for LTCC applications. *Journal of Materials Science: Materials in Electronics* **2015,** *27* (1), 134-139.

45. Chung-Lun Lo, Jenq-Gong Duh, Bi-Shiou Chiou, Wen-Hsi Lee, Microstructure characterizatics for anorthite composite glass with nucleating agents of TiO_2 under non-isothermal crystallization. *Materials Research Bulletin* **2002,** *37*, 1949-1960.

46. Hitishi Ohsato, Tsutomu Tsunooka, Minato Ando, Yoshihiro Ohishi, Yasuharu Miyauchi and Ken-ichi Kakimoto, Millimeter-wave dielectric ceramics of alumina and forsterite with high quality factor and low dielectric constant. *Journal of the Korean Ceramic Society* **2003,** *40*, 350-353.

47. Dileep Kumar, C. J.; Sunny, E. K.; Raghu, N.; Venkataramani, N.; Kulkarni, A. R., Synthesis and Characterization of Crystallizable Anorthite-Based Glass for a Low-Temperature Cofired Ceramic Application. *Journal of the American Ceramic Society* **2008,** *91* (2), 652-655.

48. Kemethmüller, S.; Hagymasi, M.; Stiegelschmitt, A.; Roosen, A., Viscous Flow as the Driving Force for the Densification of Low-Temperature Co-Fired Ceramics. *Journal of the American Ceramic Society* **2007,** *90* (1), 64-70.

49. Hamzawy, E. M.; El-Kheshen, A. A.; Zawrah, M. F., Densification and properties of glass/cordierite composites. *Ceramics International* **2005,** *31* (3), 383-389.

50. Kingery, W. D., Densification during Sintering in the Presence of a Liquid Phase. I. Theory. *Journal of Applied Physics* **1959,** *30* (3), 301-306.

51. J. H. Jean, C. H. Lin, Coarsening of tungsten particles in W-Ni-Fe alloys. *Journal of Materials Science* **1989,** *24*, 500-504.

52. Jau-Ho Jean, T. K. Gupta, Liquid-phase sintering in the glass-cordierite system. *Journal of Materials Science* **1992,** *27*, 1575-1584.

53. Condon, E. U., Physics of the Glassy State. I. Constitution and Structure. *American Journal of Physics* **1954,** *22* (2), 43-53.

54. Zachariasbn, W. H., The atomic arrangement in glass. *J. Am. Chem. Soc.* **1932,** *54,10,* 3841-3851.

55. Vallet-Regí, M., Ceramics for medical applications. *Journal of the Chemical Society, Dalton Transactions* **2001,** (2), 97-108.

56. ISARD, J. O., The mixed alkali effect in glass. *Journal of Non-Crystalline Solids* **1969,** *1*, 235-261.

57. Jan Swenson and Stefan Adams, Mixed alkali effect in glasses. *Phys Rev Lett* **2003,** *90* (15), 155507.

58. A. N. Cormack, Jincheng Du, Molecular dynamics simulations of soda-lime-silicate glasses. *Journal of Non-Crystalline Solids* **2001,** *293-295*, 283-289.

59. Alfonso Pedone, Gianluca Malavasi, M. Cristina Menziani, Ulderico Segre and Alastair N. Cormack, Role of Magnesium in Soda-Lime Glasses Insight into Structural, Transport, and Mechanical Properties through Computer Simulations. *J. Phys. Chem. C* **2008,** *112*, 11034–11041.

60. Shao, H.; Zhou, H.; Zhu, H.; Shen, X., Preparation and properties of crystallizable Glass/Al_2O_3 composites for LTCC material. *Journal of Wuhan University of Technology-Mater. Sci. Ed.* **2011,** *26* (6), 1174-1178.

61. Li, B.; Qing, Z.; Li, Y.; Li, H.; Zhang, S., Effect of CaO content on structure and properties of low temperature co-fired glass–ceramic in the Li_2O–Al_2O_3–SiO_2 system. *Journal of Materials Science: Materials in Electronics* **2015,** *27* (3), 2455-2459.

62. Ashis Kumar Mandal, Presanta Kumar Sinha, Santanu Sen, Sitendu Mondal, Chandan Guha and Ranjan Sen, Microwave preparation of SiO_2-B_2O_3-Na_2O-K_2O-CaO-Fe_2O_3-TiO_2 glass system. *J. Chem. Chem. Eng.* **2014,** *8*, 349-357.

63. Takashi Hayashi, Hajime Saito, Preparation of CaO-SiO_2 glasses by the gel method. *Journal of Materials Science* **1980,** *15*, 1971-1977.

64. Abhilash, P.; Thomas, D.; Surendran, K. P.; Sebastian, M. T.; Pinckney, L., Facile Synthesis of "Quench-Free Glass" and Ceramic-Glass Composite for LTCC Applications. *Journal of the American Ceramic Society* **2013,** *96* (5), 1533-1537.

65. Dislich, H., New routes to multicomponent oxide glasses. *Angew. Chem. internat. Edit.* **1971,** *10*, 363-370.

66. B. J. J. Zelinski and D. R. Uhlmann, Gel technology in ceramics. *Journal of Physics and Chemistry of Solids* **1984,** *45*, 1069-1090.

67. Roy, R., Gel route to homogeneous glass preparation. *Journal of The American Ceramic Society* **1969,** *52*, 344.

68. Seo, Y. J.; Jung, J. H.; Cho, Y. S.; Kim, J. C.; Kang, N. K., Influences of Particle Size of Alumina Filler in an LTCC System. *Journal of the American Ceramic Society* **2007,** *90* (2), 649-652.

69. Kumar, C. J. D.; Sowmya, T. K.; Sunny, E. K.; Raghu, N.; Venkataramani, N.; Kulkarni, A. R., Influence of Nature of Filler on Densification of Anorthite-Based Crystallizable Glass+Ceramic System for Low Temperature Cofired Ceramics Application. *Journal of the American Ceramic Society* **2009,** *92* (3), 595-600.

70. Gangwar, J.; Gupta, B. K.; Tripathi, S. K.; Srivastava, A. K., Phase dependent thermal and spectroscopic responses of Al_2O_3 nanostructures with different morphogenesis. *Nanoscale* **2015,** *7* (32), 13313-44.

71. Gupta, T. K.; Jean, J.-H., Principles of the development of a silica dielectric for microelectronics packaging. *Journal of Materials Research* **2011,** *11* (1), 243-263.

72. Fang, Y.; Li, L.; Xiao, Q.; Chen, X. M., Preparation and microwave dielectric properties of cristobalite ceramics. *Ceramics International* **2012,** *38* (6), 4511-4515.

73. Pagliari, L.; Dapiaggi, M.; Pavese, A.; Francescon, F., A kinetic study of the quartz–cristobalite phase transition. *Journal of the European Ceramic Society* **2013,** *33* (15-16), 3403-3410.

74. Jean, J.-H.; Gupta, T. K., Devitrification inhibitors in borosilicate glass and binary borosilicate glass composite. *Journal of Materials Research* **1995,** *10* (5), 1312-1320.

75. I. Yanase, H. Kobayashi and T. Mitamura, Thermal property and phase transition of the synthesized new cubic leucite-type compounds. *Journal of Thermal Analysis and Calorimetry* **1999,** *57*, 695-705.

76. J. F. Schairer and N. L. Bowen, The system K_2O-Al_2O_3-SiO_2. *American Journal of Science* **1955,** *253*, 681-746.

77. Seong-Hun Choe, Shuji Tanaka and Masayoshi Esashi, A Matched Expansion MEMS Probe Card with Low CTE LTCC Substrate. In *2007 IEEE International Test Conference*, IEEE: Santa Clara, CA, USA, 2007; pp 1-6.

78. Vadim Gektin, Avram Bar-Cohen and Sorin Witzman, Coffin-Manson Based Fatigue Analysis of Underfilled DCAs. *IEEE Trans. Compon. Packag. Technol. A* **1998,** *21A*, 577-584.

79. Qing, Z.; Li, B.; Li, H.; Li, Y.; Zhang, S., Effects of MgO on properties of Li_2O–Al_2O_3–SiO_2 glass–ceramics for LTCC applications. *Journal of Materials Science: Materials in Electronics* **2014,** *25* (5), 2149-2154.

80. Torsten Rabe, Wolfgang A. Schiller, Thomas Hochheimer, Christina Modes and Annette Kipka, Zero shrinkage of LTCC by self constrained sintering. *Int. J. Appl. Ceram. Technol.* **2005,** *2 [5]*, 374-382.

81. Liu, X. D.; Wang, S. H.; Hou, Z. X.; Zhou, D.; Yang, L. Q., Overview of the Control Methods for LTCC Substrate Shrinkage. *Advanced Materials Research* **2014,** *989-994*, 2895-2898.

82. Di Zhou, Lixia Pang, Jing Guo, Xi Yao, A bismuth-based microwave dielectric ceramic sintered at low temperature and preparation method. China, ZL201210185088.X.

Chapter 2 Experimental and characterization methods

This chapter provides the information about the chemicals used in this project and describes the main synthesis process. We also illustrate the characterization methods and corresponding test conditions.

2.1 Chemicals

The information about the chemicals available to us for this project is listed in the Tab. 2-1. Herein we choose chemicals with purity as high as possible for the sake of low dielectric loss.[1] We also point out the CAS number of each chemical for right selection of chemicals possessing polymorphs, such as Al_2O_3, SiO_2 and ZrO_2.

Tab. 2-1 Information about chemicals involved in this thesis.

Chemicals	CAS number	Vender	Purity
Al_2O_3 (135nm)	1344-28-1	US Research Nanomaterials, Inc.	99.90%
Al_2O_3 (300nm)	1344-28-1	US Research Nanomaterials, Inc.	99.90%
Al_2O_3 (1μm)	1344-28-1	Alfa Ventron inorganics	99.99%
$Ba(NO_3)_2$	10022-31-8	Sigma-Aldrich	≥99%
$CaCO_3$	471-34-1	Chem-supply	≥99%
$Ca(NO_3)_2 \cdot 4H_2O$	13477-34-4	The British drug houses LTD.	≥98%
Ethanol	64-17-5	Merck KGaA	Absolute
HNO_3	7697-37-2	Ajax Finechem Pty LTD.	70%
H_3BO_3	10043-35-3	The British drug houses LTD.	≥99.5%
K_2CO_3	584-08-7	Chem-supply	≥99%
KNO_3	7757-71-1	The British drug houses LTD.	Analytical reagent
$NaNO_3$	7631-99-4	Sigma-Aldrich	≥99.999%

$NH_3 \cdot H_2O$	1336-21-6	The British drug houses LTD.	35%
Polyvinyl butyral	63148-65-2	Sigma-Aldrich	N/A
Fused SiO_2	60676-86-0	Sigma-Aldrich	99.50%
Tetraethyl orthosilicate	78-10-4	Sigma-Aldrich	98%
ZrO_2	1314-23-4	Sigma-Aldrich	99%

2.2 Experimental methods

In this thesis, we have developed five LTCC materials with dielectric constant ranging from 4 to 12. Four of them are based on the composites of amorphous phases and ceramics, while the other is the one only containing crystalline phases.

2.2.1 Amorphous phases and ceramics composites

In terms of the composites based on amorphous phases and ceramics, the amorphous phases are synthesized using the sol-gel method, instead of conventional melt-quench method. This is mainly because the amorphous phases can be synthesized at lower temperature by sol-gel method so that the evaporation of some components, such as B_2O_3, can be suppressed. The fabrication process, as shown in Fig. 2-1, can be divided into four steps.

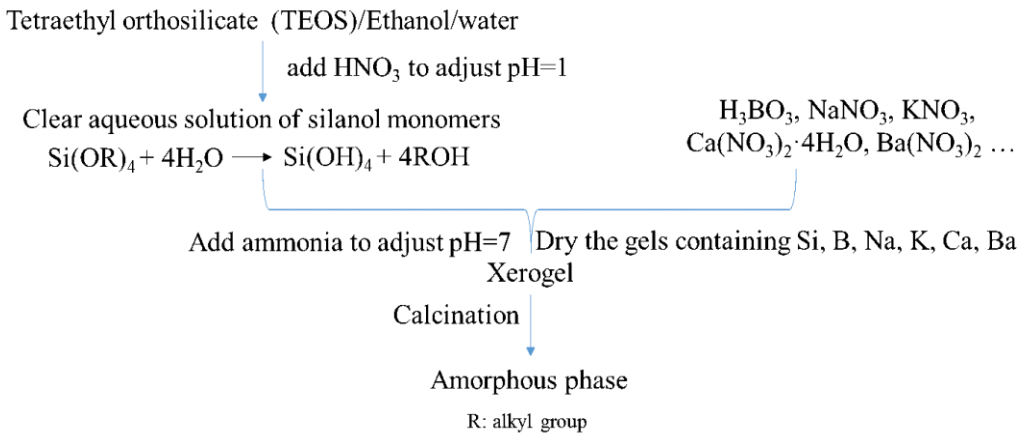

Fig. 2-1 Main process to synthesize multi-components amorphous phases using sol-gel method.

The first step relates to the hydrolysis of the tetraethyl orthosilicate (TEOS). The TEOS is mixed with deionized water and ethanol, where the ethanol works as the mutual solution since TEOS is insoluble in water. As illustrated in Fig. 2-2, both the hydrolysis and condensation rates of TEOS show evident dependence on the pH of solution. For the sake of hydrolysis, the pH of the solution mixture is adjusted to 1~2 by HNO_3 at this stage. Secondly, various amount of metal nitrates are introduced into hydrolysed solution according to designed composition. In this step, the metal ions will mix well with the hydrolysed silanol monomers. After that, the pH of mixed solution is adjusted to ~7 with ammonia solution for condensation. In this process, the silanol monomers condensate and the metal ions are randomly integrated into the silica gel. Finally, the multi-components gel is dried at ~60°C and the obtained xerogel is calcined between 600°C and 800°C to remove the organics.

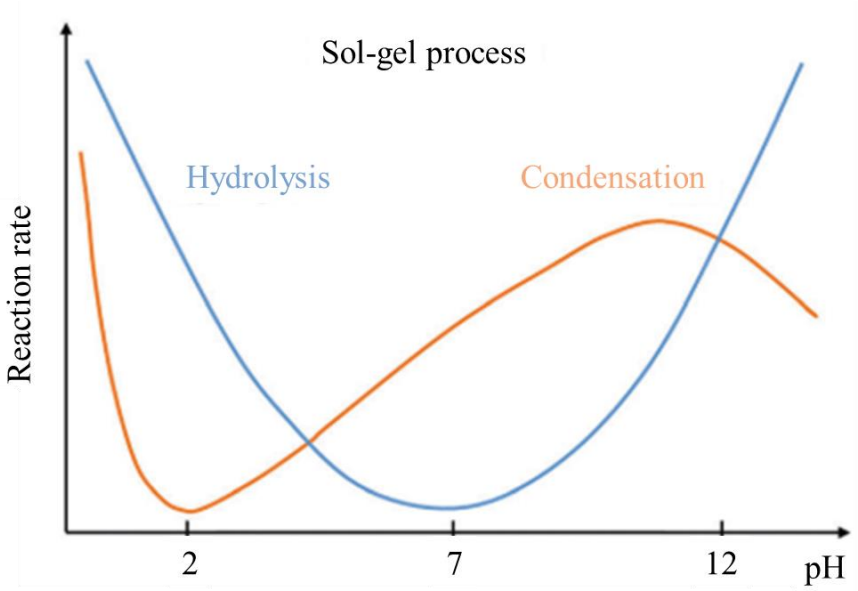

Fig. 2-2 Dependence of hydrolysis (blue curve) and condensation (orange curve) rates of tetraethyl orthosilicate on pH. (The figure is reproduced from Montheil T. et al.[2])

The obtained amorphous phase powders are ball milled with ceramics materials according to designed compositions in Teflon jars with yttrium stabilized zirconia balls for 15h. A certain amount of ethanol is added as the medium to achieve a homogeneous mixture. After milling, the mixture is transferred into the glass container and dried at about 100°C. The dried powder

mixtures are made into pellets with the diameter of 13mm under uniaxial pressure of 7MPa. The green pellets are then sintered between 850^{o}C and 900^{o}C with the heating rate of 3^{o}C/min. After sintering, the pellets are coated with silver paste and calcined at 700^{o}C for 15min to achieve better electrical contact.

2.2.2 Crystalline composite

With regard to the composite made up of crystalline phases, the important precursor $KBSi_2O_6$ phase is synthesized by the solid state reaction of the K_2CO_3, H_3BO_3 and SiO_2, which are mixed according to the stoichiometric formulation of $KBSi_2O_6$. To improve the reaction, the powder mixtures are uniaxially pressed into pellets for calcination. After that, the sintered pellets are ground and ball milled into fine powders again. Then Al_2O_3 with different particle sizes, as-synthesized $KBSi_2O_6$ and CaO are weighted according to designed composition and ball milled with absolute ethanol. After that, the dried powder mixtures are uniaxially pressed into pellets at 7MPa and sintered between 850^{o}C and 900^{o}C for 6h. Herein, we use CaO as the calcium resource, instead of $CaCO_3$, because we have found that the sintering temperature can be decreased by using CaO. The CaO is achieved by calcining the $CaCO_3$ at 1000^{o}C for 2h and then conserves in the furnace with the temperature of 150^{o}C. After sintering, the pellets are coated with silver paste and also calcined at 700^{o}C for 15min to achieve better electrical contact.

2.2.3 Compatibility with silver electrode

To check the compatibility with silver electrode, the milled powder mixtures of developed compositions are all granulated with 5wt% polyvinyl butyral (PVB). The granulated powders are placed there for one night before pressing into pellets. Afterwards, the silver paste is coated on the surfaces of the green pellets followed by co-firing at corresponding sintering temperature for the same soaking period. Herein the granulated particles can form more compacted pellets to prevent the diffusion of silver paste before sintering.

2.3 Structures and compositions characterization

2.3.1 X-ray diffraction

X-ray diffraction (XRD) is primarily employed to identify the phases of crystalline materials. In principle, as show in Fig. 2-3, when the monochromatic X-rays impinge onto the crystalline substances, which act as three-dimensional diffraction gratings, a constructive interference pattern is formed if the Bragg's law ($\lambda=2d\sin\theta$) is satisfied. Herein the λ is the wavelength of the X-ray, d is the inter-planar spacing of crystal and θ is the half angle between the diffracted beam and the incident beam.[3] With the knowledge of λ and θ, a series of d values can be deduced and then used for identification by comparing with reference patterns since every crystal has a set of unique d-spacings. In contrast, the amorphous phases feature a broad hump peak in the range from 10^o to 30^o due to the lack of long range ordering in structure.

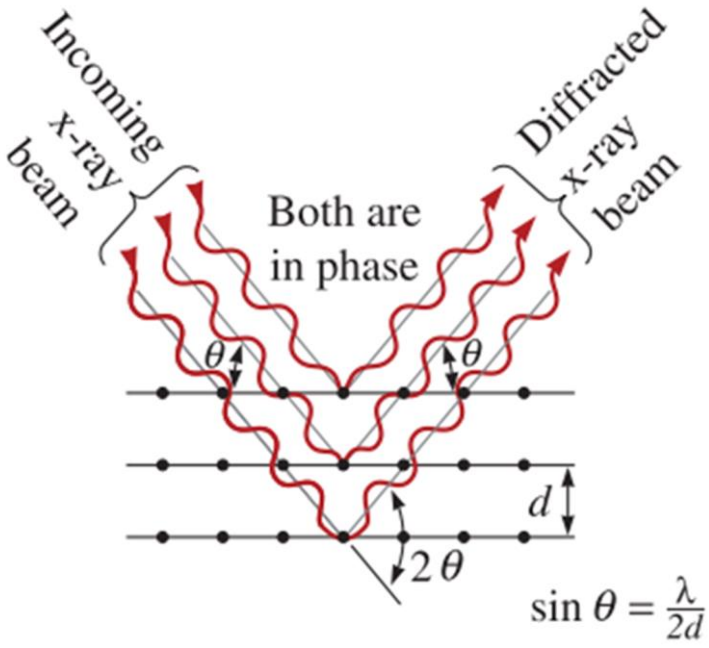

Fig. 2-3 Schematic of Bragg's law for X-ray diffractions. (The figure is reproduced from Askeland D. R. et al.[3])

Rietveld refinement is a technique to fit an experimental diffraction pattern with a structural model based on the non-linear least squares approach. When the calculated pattern matches well with the experimental pattern, more structural details can be revealed, such as the unit-

cell parameters, phase fractions and atomic coordinates. There are some statistic parameters to evaluate the quality of refined results, especially the profile R-factor (R_p), weighted profile R-factor (R_{wp}) and goodness of fit (GOF), which are calculated as follows:[4, 5]

$$R_p = \frac{\sum |y_i(obs) - y_i(cal)|}{\sum y_i(obs)}$$

$$R_{wp} = \sqrt{\frac{\sum w_i[y_i(obs) - y_i(cal)]^2}{\sum w_i\, y_i(obs)^2}}$$

$$GOF = \sum \frac{[y_i(obs) - y_i(cal)]^2}{N - P}$$

wherein y_i(obs) and y_i(cal) are the observed intensity and calculated intensity at the i^{th} step, respectively. The w_i equals $1/y_i$(obs), N is the number of observations and P is the number of parameters adjusted.

In this thesis, XRD is mainly used to identify the phases presented in the sintered samples, as well as the broad hump peaks of the sol-gel derived amorphous phases. The XRD patterns are carried out on a PANalytical Empyrean Diffractometer with CuKα radiation ($\lambda_{K\alpha1}$=1.5406Å and $\lambda_{K\alpha2}$=1.5443 Å). The applied voltage and current of X-ray diffractometer is 45 kV and 40 mA, respectively. The setup step size is 0.013 ° and the time per step is 150s. For the as-synthesized $KBSi_2O_6$ powder, the time per step is extended to 600s to achieve an experimental pattern of high quality. Then it is further refined using Rietveld method as implanted in Jana 2006 software.

2.3.2 Attenuated total reflectance Fourier transform infrared spectroscopy

Attenuated total reflectance Fourier transform infrared (ATR-FTIR) spectroscopy utilities the evanescent wave to detect the chemical bonds in samples. As illustrated in Fig. 2-4, a beam of infrared light comes into the ATR crystal at critical angle so that the light total reflects at the internal surface. In this case, the evanescent wave is formed and permeates into the sample with the thickness between 0.5 and 2 micrometres. The evanescent wave will be attenuated since part of the energy would be absorbed by specific chemical bond. This energy change will

be record by the detector in the IR spectrometer and generates corresponding infrared spectrum.

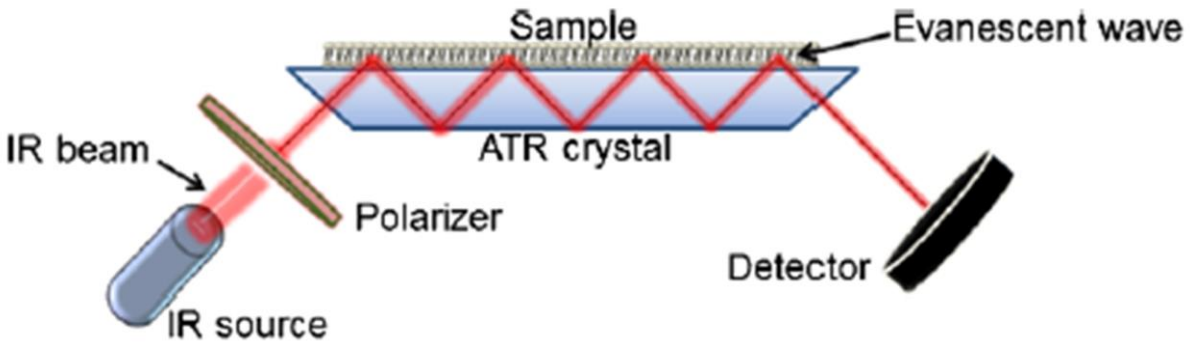

Fig. 2-4 Schematic representation of an ATR-FTIR system. (The figure is reproduced from Ausili A. et al.[6])

ATR-FTIR spectroscopy can be directly used to characterize the samples in the state of solid powder or liquid. In this work, the ATR-FTIR spectrums of sol-gel derived amorphous phase powders are investigated by PerkinElmer FT-IR spectrometer (Spectrum Two) from 400cm^{-1} to 4000cm^{-1}.

2.3.3 Laser scattering

Particle sizes of the powders have profound effects on the process and performance of final sintered samples. As shown in Tab. 2-2, there is a variety of characterization techniques that can be used to measure particle sizes.[7] Each method covers a characteristic size range and partly overlaps. In this work, the laser scattering method is employed thanks to its wide measuring range (from tens of nanometres up to several millimetres in size), rapid measurements and reliable results.

Tab. 2-2 Particle size characterization techniques and corresponding measuring range.

Characterization technique	Particle size range								
	0.1nm	1nm	10nm	100nm	1μm	10μm	100μm	1mm	10mm
Laser scattering			■	■	■	■	■	■	■
Dynamic light scattering	■	■	■	■	■	■			
Electrophoretic light scattering		■	■	■	■	■			
Automated imaging				■	■	■	■	■	■
Sedimentation			■	■	■	■			
Electron sensing			■	■	■	■	■		
Sieve analysis						■	■	■	■

When irradiated by a laser beam, a single particle scatters light and the intensity varies with the scattering angle. The formed spatial intensity distribution pattern depends on the particle size as shown in Fig. 2-5. Herein the particle size refers to a volume equivalent sphere diameter since particles are generally in irregular shapes. When a particle group is irradiated by laser, a specific light intensity distribution pattern is formed as the result of overlaid scattered light from every single particle. By analysing the pattern, the particle size distribution can be calculated based on the Mie scattering theory.

The characterization results can be presented by both frequency distribution and cumulative distribution. On one hand, the amount of particles existing in respective particle size intervals is described by frequency distribution. On the other hand, the percentage of particles with a specific particle size or below is presented by cumulative distribution.

In this project, the sol-gel derived amorphous phases powders are dispersed in ethanol and their particle size distributions are characterized by the laser scattering on a Malvern particle size analyser in the range between 0.02μm and 2000μm.

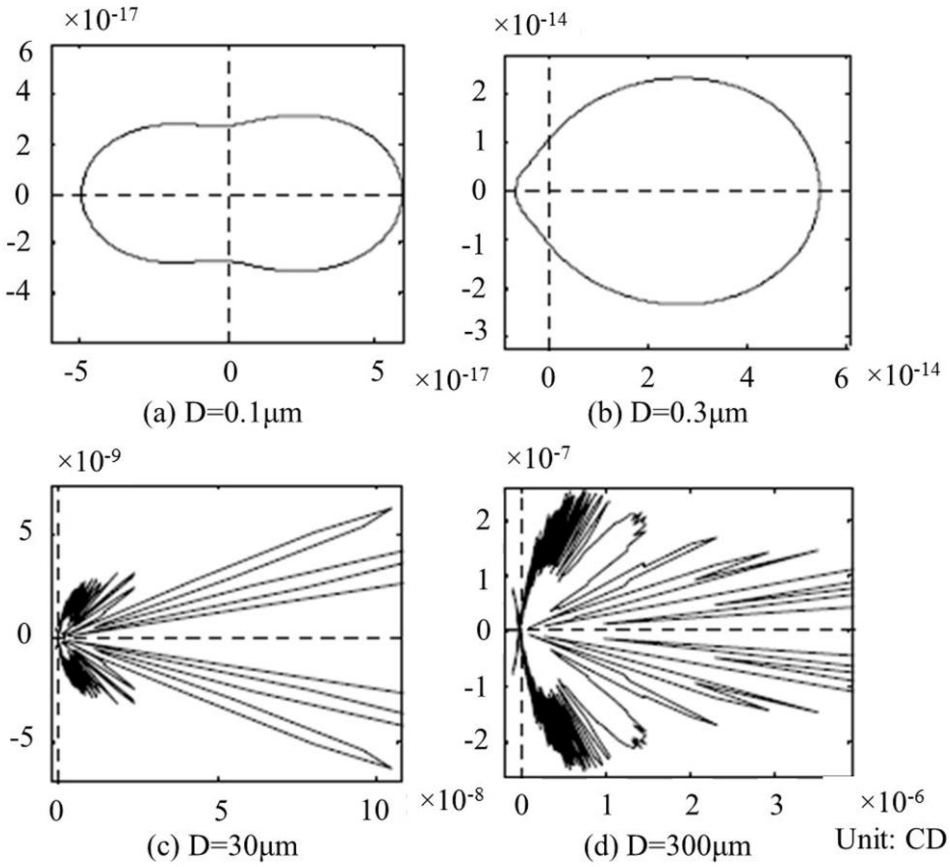

Fig. 2-5 Relationship between particle size (D) and light intensity distribution of scattered light. (The figure is reproduced from Shen S. et al.[8]).

2.3.4 Scanning electron microscope

Scanning electron microscope (SEM) is carried out to characterize the microstructure and chemical compositions. In principle, the electron beam produced in the electron gun is focused by a series of magnetic lenses and apertures. When the beam strikes the sample, the electrons interact with the atoms of the sample in a bulb shaped volume and generate a variety of signals as presented in Fig. 2-6. Among these signals, secondary electrons (SEs), backscattered electrons (BSEs) and characteristic X-rays are of great importance.

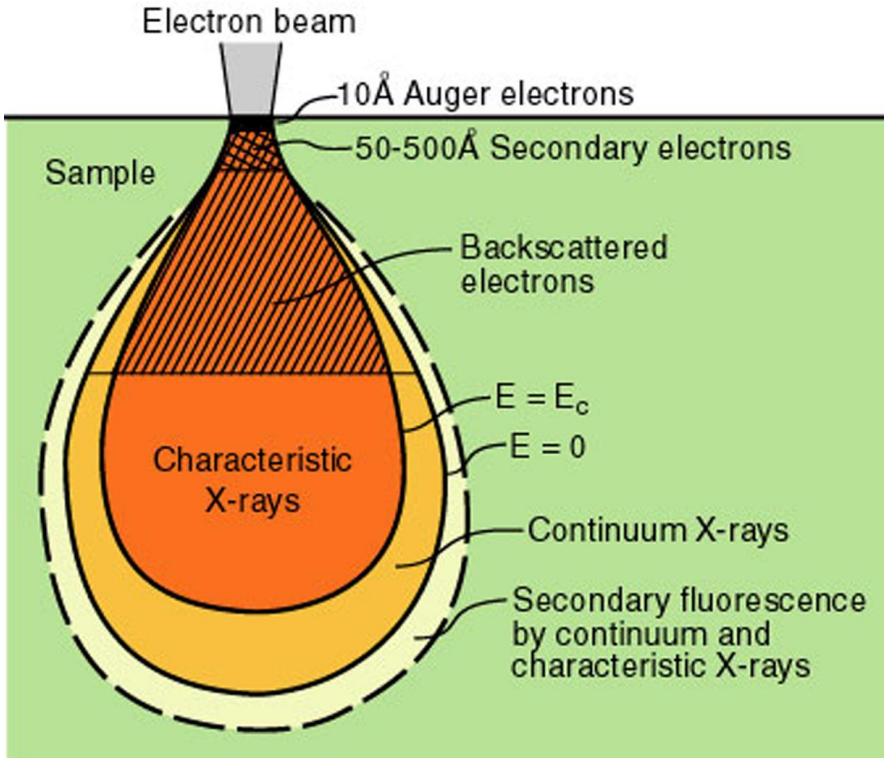

Fig. 2-6 Signals generated when the electron beam interacts with the sample. (The figure is reproduced from Zhang S.[9]).

SEs refer to the electrons that loosely bound at the outer shell of the sample atoms and knocked out from their orbits by an incident electrons.[10] They are generally used to characterize the

surface topographic information because they come from a shallow area with the similar size as that of the electron probe and can generate the images with highest spatial resolution.

BSEs are the electrons that scattered by the nucleuses of sample and re-emerge at the surface. Images based on BSEs have slightly lower resolution than those based on SEs because the BSEs come from relatively deeper position in the specimen.[11] They carry compositional information and show evident contrast on different phases since the backscatter co-efficient is proportional to the average atom number.

Characteristic X-rays are generated when the incident high-energy particle knocks out an inner-shell electron and an outer-shell electron moves into the empty orbit. For example, the incident electrons collide with K-shell electrons of elements, and K-shell electrons are ejected. Then electrons from higher energy level, such as L-shell, would drop to this vacancy and release the extra energy as X-ray. The energy-dispersive X-ray spectrometer (EDS) is the characterization method of chemical compositions based on the characteristic X-rays.

In our experiments, the microstructures of the sintered samples are mainly observed by the Zeiss UltraPlus field emission scanning electron microscope (FESEM) under the low operating voltages of 3 kV. The chemical compositions of sintered samples and element distribution of the Ag at the Ag/LTCC interface are characterized by Hitachi 4300 FESEM in conjunction with an EDS under operating voltages of 15kV. The detection limit of the EDS is typically at 0.1wt% level. In addition, the characteristic X-rays in our EDS characterization are directly detected by a lithium-drifted silicon crystal. To avoid the influence of rough surface and charging effect, the sintered pellets are finely polished and coated with thin carbon layer (20nm). The co-fired samples are amounted in the resin for better polishing of the cross section of Ag/LTCC interface. The standards used for calibration include $NaAlSi_3O_8$, $KAlSi_3O_8$, $MgCaSi_2O_6$, $BaSO_4$, pure Zr and Ag.

2.3.5 X-ray fluorescence spectrometer

The X-ray fluorescence (XRF) is based on the secondary X-rays from the sample when contacted with incident X-ray beam.[12] The XRF spectrometer provides fingerprints for

elemental analysis since each element has a unique XRF spectrum.

The detection limit of XRF spectrometer can reach the ppm level. The secondary X-rays in our XRF characterization are separated by diffraction on a single crystal before being detected. This implies that the XRF spectrometer herein can show a relatively better resolution for the peaks in close positions, such as the Kα peak of Si (1.740keV) and the Lα peak of Sr (1.806keV), and thus provide more accurate quantitative information.

However, neither EDS nor XRF is effective in detecting the light elements, such as boron. This is because the light elements show low X-ray productivity efficiency due to Auger effect. In this work, the XRF is mainly employed to identify the heavy elements (from Na) in sol-gel derived amorphous phases. The XRF is undertaken using a Panalytical (4kW) simultaneous XRF wavelength dispersive spectrometer, with a fixed analysing channel for each of the 24 reportable elements. Power setting is fixed at 40kV, 100mA and measuring time is 60 seconds.

2.3.6 Inductively coupled plasma atomic emission spectroscopy

The inductively coupled plasma atomic emission spectroscopy (ICP-AES) is mainly used to characterize the boron element in our samples. In theory, almost all elements except Argon can be identified by this method. This characterization method measures the emission when the excited species falling to ground state and it mainly covers three steps. Initially, stable Argon plasma with high temperature is formed in the intense electromagnetic field. Secondly, the sample is broken up into respective atoms and then excited by the plasma, emitting photons at characteristic wavelengths.[13] Finally, the corresponding intensity, which is proportional to the concentrations of the elements, is detected by optical spectrometer.

Boron in our samples is measured using the 208.956nm atomic emission line. Agilent 700-ES series ICP-AES radial instruments is used with a 1.5kW plasma. Sample introduction is through Duramist nebuliser (1mL/min) and Twister 50 mL borosilicate cyclonic spray chamber. Combining the XRF with ICP-AES characterization, the compositions of sol-gel derived amorphous phases are completely identified.

2.4 Electrical properties measurement

2.4.1 Dielectric measurement

Dielectric properties, including dielectric constant and dielectric loss, are characterized by a precision LCR meter (Agilent, E4980A) with 1V (AC) excitation from 100Hz to 2MHz. The LCR meter offers capacitance-dissipation factor measurement with a basic accuracy of ±0.05% and ±0.0005, respectively. There are parallel and series modes for measurement, and the former is chosen here due to the relatively small capacitance value of our samples. The samples are made into parallel-plate capacitors and the dielectric constants (ε_r) are calculated according to the equation: $C=\varepsilon_0 \cdot \varepsilon_r S/t$, where C is capacitance, ε_0 is the dielectric constant of free space, S is the area of electrode and t is thickness of the sample. The samples under test are mounted with Agilent 16034E fixture. Open and short circuit calibration is conducted before each new cable connection to perform the compensation of fixture. The temperature dependence of dielectric properties are investigated in the range from room temperature to 100ºC, which is the typical operation temperature range for devices, by the LCR meter connected with high temperature control system (developed by Xi'an Jiaotong University) with TH26011B fixture. The sample environment systems and LCR meter are controlled by a computer programme, which can record the temperature and dielectric data at the same time.

2.4.2 Resistivity measurement

The insulation resistance of a ceramic capacitor refers to the ratio between the applied DC voltage and the flow current after a set time. The flow current varies with time and mainly covers charge current, absorption current, as well as leak current.[14] When the DC voltage applied, the charge current flows immediately and decreases exponentially. Then absorption current keeps decreasing and finally leak current reaches a constant value. Therefore, the resistance is usually measured at a specific time.

In this thesis, resistance of sintered sample is characterized by Keithley 6517B electrometer

under 100V (DC) for 1min according to our industry partner's requirement. Then the electrical resistivity is calculated by the equation: $\rho=R\cdot S/l$, where R is the resistance, S is area of electrode and l is the thickness, respectively.

2.5 Thermal properties measurement

2.5.1 Thermal expansion measurement

The coefficient of thermal expansion (CTE) is defined as

$$\mathrm{CTE} = \frac{1}{L_0} \cdot \frac{dL}{dT}$$

Where L_0 is the initial length of sample under reference temperature T_0.[15] According to above formula, CTE can be concluded once length change of sample under different temperatures is identified. Push-rod dilatometer is generally employed to characterize this length change.[16]

In our experiments, the CTE was characterized by Setsys Evolution (TMA-16/18) from room temperature to 300°C. The test samples are with the diameter below 8mm and thickness between 2mm and 4mm.

2.5.2 Glass transition temperature measurement

The thermogravimetric and differential thermal analysis (TG-DTA) is mainly used to identify the glass transition temperature of the sol-gel derived amorphous phases in this work. The TG measures mass changes of the sample. The DTA records the temperature difference between sample and the inert reference substance in the form of endothermic peak or exothermic peak. Combining TG and DTA, the glass transition temperature, at which endothermic peak appears without mass change, of the amorphous phases can be identified. In this work, the TG-DTA is performed by NETZSCH STA (449F3) in the air environment from room temperature to 950°C with a heating rate of 10°C/min.

Reference

1. Imanaka, Y., *Multilayered low temperature cofired ceramics technology*. Springer US: 2005; p 229.

2. Montheil, T.; Echalier, C.; Martinez, J.; Subra, G.; Mehdi, A., Inorganic polymerization: an attractive route to biocompatible hybrid hydrogels. *Journal of Materials Chemistry B* **2018,** *6* (21), 3434-3448.

3. Donald R. Askeland, Pradeep P. Fulay, Wendelin J. Wright, *The science and engineering of materials*. 6 ed.; Cengage Learning: 2011.

4. Stefan Kemethmuller, Andreas Roosen, Friedlinde Goetz-Neunhoeffer, Jurgen Neubauer, Quantitative Analysis of Crystalline and Amorphous Phases in Glass–Ceramic Composites Like LTCC by the Rietveld Method. *Journal of the American Ceramic Society* **2006,** *89* (8), 2632-2637.

5. Young, R. A., *The Rietveld Method*. Oxford University Press: Oxford, United Kingdom, 1995.

6. Ausili, A.; Sánchez, M.; Gómez-Fernández, J. C., Attenuated total reflectance infrared spectroscopy: A powerful method for the simultaneous study of structure and spatial orientation of lipids and membrane proteins. *Biomedical Spectroscopy and Imaging* **2015,** *4* (2), 159-170.

7. Rupinder Kaur Dhamoon, Harvinder Popli, Geeta Aggarwal, Madhu Gupta, Particle size characterization techniques, factors and quality-by-design approach. *International Journal of Drug Delivery* **2018,** *10(1)*, 01-11.

8. Shaowei Shen, Shuhua Yan, Chunlei Zhou, E Li and Huipeng Tong, Research of laser particle sizer based on scattering theory. In *2008 International Conference on Information and Automation*, 2008; pp 1797-1800.

9. Zhang, S., Study of fluorine-doped tin oxide (FTO) thin films for photovoltaics applications. Technische Universität Darmstadt, 2017.

10. Inkson, B. J., Scanning electron microscopy (SEM) and transmission electron microscopy (TEM) for materials characterization. In *Materials Characterization Using Nondestructive Evaluation (NDE) Methods*, 2016; pp 17-43.

11. Vernon-Parry, K. D., Scanning electron microscopy: an introduction. *III-Vs Review* **2000,** *13* (4), 40-44.

12. Chen, H.; Rogalski, M. M.; Anker, J. N., Advances in functional X-ray imaging techniques and contrast agents. *Phys Chem Chem Phys* **2012,** *14* (39), 13469-86.

13. John C Lindon, George E Tranter, David W Koppenaal, *Encyclopedia of spectroscopy and spectrometry* Academic Press: 2016; p 3584.

14. Gill, P., *Electrical power equipment maintenance and testing*. Taylor & Francis Inc: 2009; p 1000.

15. J D James, J A Spittle, S G R Brown and R W Evans, A review of measurement techniques for thermal expansion coefficient of metals and alloys at elevated temperatures. *Meas. Sci. Technol.* **2001,** *12*, R1-R15.

16. Valentich, J., A virtreous silica tube dilatometer for the measurement of thermal expansion of solid from -195 to 1000ºC. *Journal of materials science* **1979,** *14*, 371-378.

Chapter 3 Sol-gel derived amorphous phases for Al_2O_3-based composites

3.1 Introduction

The research for device integration and miniaturization has been the focus of the microelectronic industry field in the past decades.[1, 2] The LTCC technology, which embeds the electronic components and electrodes into 3D stacked ceramics sheets, has been proved to be an effective method for device packaging and size downscaling.[3, 4] The LTCC technology features low sintering temperature, which mainly stems from the limitation of melting points of inner co-fired electrodes, such as silver, gold and copper. Considering the high cost of gold electrode and the easy oxidation of copper electrode in the air environment,[5] silver electrode is more widely used in the commercially application and thus the sintering temperature is required below 900°C.

Considering the limitation of sintering temperature, the materials can be selected for LTCC application is not much since most electronic ceramics have to be sintered above 1000°C. To reduce the sintering temperature, some methods, such as adding the glasses with low softening point, sintering aids and using raw materials with smaller particle size, are employed.[6-8] Among these methods, the addition of glass phase with low softening temperature is the most effective and most widely used strategy. Depending on the amount of glass, the materials can be classified into glass-ceramic or glass/ceramic composite.[9, 10] The former is made up of fully glassy phase which gets crystallized during sintering. For this kind of materials, the degree of crystallization should be finely controlled.[11] Otherwise, it will result in poor dielectric loss and mechanism properties.[12] The latter consists of a glass with low softening temperature and ceramic with good dielectric properties. In comparison, the glass/ceramic composite is more practical in performance tuning.

Before developing the glass/ceramic composite, it is inevitable to fabricate the glassy phase. Melt-quench method is now the most widely used glass making method, with which the raw materials are melted at high temperature (~1500°C) and then quenched to room temperature in

water.[9, 10, 13] But this method does not always work steadily because it lacks of the control on the evaporation of some glass components, such as B_2O_3, as well as undesired crystal nucleation due to change of quench rate.[14] In addition, some specific glass compositions, such as CaO-SiO_2 glasses, still have not been successfully prepared by this method because of the presence of the stable liquid-liquid immiscibility region in this system.[15] To make up these deficiencies, Abhilash P. et al. have proposed a novel quench-free method for a specific glass with composition of 10%ZnO-2% B_2O_3-8% P_2O_5-80%TeO_2.[16] This quench-free method derived glass shows the similar performance with that made by melt-quench method in their case. However, there is no further research to support this method could be extended to other glass compositions.

Alternatively, the multi-components amorphous phases can also be synthesized by the sol-gel method.[17] With this sol-gel method, the amorphous phases can be synthesized at lower temperature without quench process, thus the evaporation of B_2O_3 and undesired crystallization could be avoided. Additionally, the previously mentioned CaO-SiO_2 glass, which has not been successfully fabricated by the melt-quench method, can also be synthesized by the sol-gel method. This implies the sol-gel method should be applied to more glass compositions. However, it is seldom involved to fabricate the amorphous phase in LTCC application.

The properties of the amorphous phases should also meet following requirements. First of all, the softening temperature of amorphous phase should be around ~800ºC so that it can form viscous liquid and permeate into the gaps among the ceramic particles during the sintering process.[18, 19] Furthermore, the densification can be further promoted if the viscous liquid of amorphous phase has a good wetting behaviour with the grains of ceramic.[12, 20] Additionally, the network of the amorphous phase in the sintered sample can dissipate the energy in the high frequency, thus leading to deteriorated dielectric loss.[21] This can be improved by controlling the amorphous phase to get crystallized during sintering.[22]

To work as the ceramic packaging substrates, many properties of the glass/ceramic composites have to be balanced under strict conditions. Besides good dielectric properties, the developed LTCC materials should also have resistivity above $10^{12}\Omega\cdot$cm as a good insulator.[23] Even below

the melting point of co-fired electrode, there should be no any reaction or diffusion happened between electrode and the LTCC materials. Furthermore, the LTCC modules are generally connected with other modules, such as silica or alumina chips, to realize the specific function. Thus the coefficient of thermal expansion should match with each other for reliable performance.[24, 25]

In this work, we will develop a low temperature sol-gel approach to synthesize the amorphous phases, and use them to develop amorphous phase/Al_2O_3 composites for potential LTCC applications. In terms of discussion and communication with the industry partner based on current products, two SiO_2-dominated amorphous phase compositions are considered for reference for this development. We denote them as Amorphous phase-1 and Amorphous phase-2, respectively. The nominal chemical composition of Amorphous phase-1 is 80.01% SiO_2-0.78% Na_2O-2.33% K_2O-2.33% CaO-14.55% B_2O_3 (in mole ratio), while that of Amorphous phase-2 is 81.06% SiO_2-0.28% Na_2O-0.85% K_2O-3.40% CaO-5.09% BaO-9.32% B_2O_3 (in mole ratio). The biggest difference between these two phases is that Amorphous phase-2 contains BaO, which could actively influence the structures and thermal properties of amorphous phase.[26] We initially synthesized these two amorphous phases using the sol-gel method. Their structures, chemical compositions, particle size distributions and thermal properties were characterized. Then these two so-gel derived amorphous phases were further mixed with Al_2O_3, which is the most widely used ceramic for its good dielectric properties,[27] and the corresponding performance of composites was characterized. This work will provide two LTCC materials with comprehensive performance for commercial application.

3.2 Syntheses, structures and properties of sol-gel derived amorphous phases

3.2.1 Amorphous phase-1

Synthesis of Amorphous phase-1

The nominal composition of the Amorphous phase-1 is 80.01% SiO_2-0.78% Na_2O-2.33% K_2O-2.33% CaO-14.55% B_2O_3 (in mole ratio). It was synthesized by the sol-gel method as follows. Initially, 9.3mL tetraethyl orthosilicate (TEOS, 98%, Sigma-Aldrich) was mixed with 9.3mL deionized water, as well as 100mL ethanol. For the sake of hydrolysis, the pH value of above

mixed solution was adjusted to 1~2 by HNO_3 (70%, Ajax Finechem Pty LTD.). Until the clear solution appeared, 0.9169g H_3BO_3 (≥99.5%, The British drug houses LTD.), 0.0673g $NaNO_3$ (≥99.999%, Sigma-Aldrich), 0.2402g KNO_3 (Analytical reagent, The British drug houses LTD.) and 0.2806g $Ca(NO_3)_2 \cdot 4H_2O$ (≥98%, The British drug houses LTD.) were added. Next adjust the pH value of the mixed solution to ~7 with ammonia solution (35%, The British drug houses LTD.). Then xerogel containing Si, B, Na, K and Ca was obtained by drying at 60°C. Finally the xerogel was further calcined from 600°C to 800°C for 2h to remove organics.

Structures and properties of Amorphous phase-1

The XRD patterns of the xerogel and that calcined from 600°C to 800°C have been characterized in Fig. 3-1. The xerogel and the powders calcined below 700°C show typical amorphous structures with broad hump peaks in the range between 15° and 35°. However, when the calcined temperature is 800°C, a tiny but sharp peak appears at the top of the broad peak of amorphous phase, indicating the appearance of the crystalline phase. Although only one peak is obtained, considering the composition of Amorphous phase-1, this peak could be indexed to the cristobalite (SiO_2) phase (ICSD code: 77452). On balance, the Amorphous phase-1 calcined at 700°C is chosen for further experiments in this study.

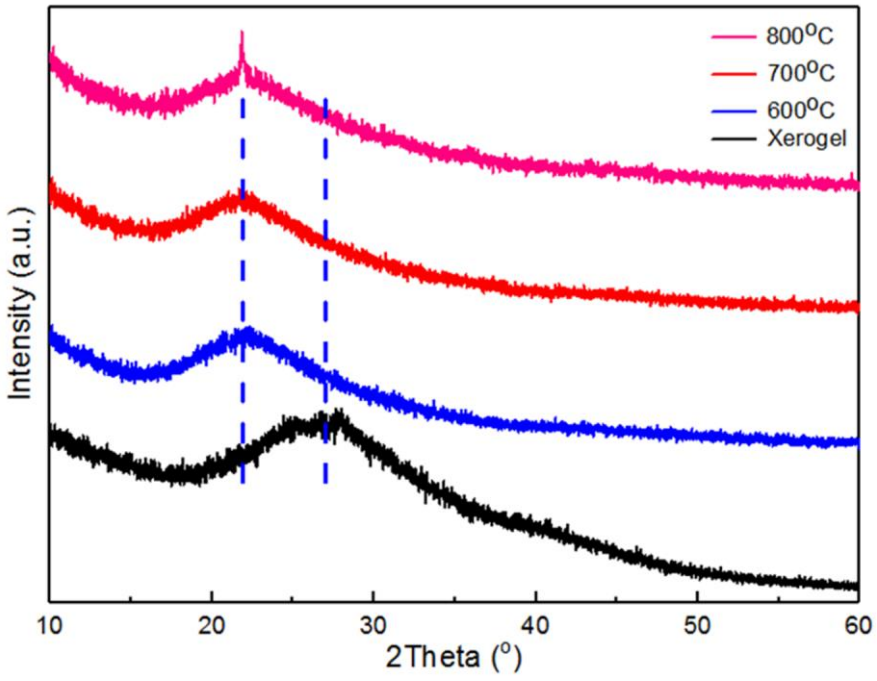

Fig. 3-1 XRD patterns of the Amorphous phase-1 xerogel and that calcined from 600°C to

800°C for 2h.

Fig. 3-2 presents the attenuated total reflectance Fourier transform infrared (ATR-FTIR) spectroscopy of calcined Amorphous phase-1 powder from 4000cm^{-1} to 400cm^{-1}. The peak centred at 460cm^{-1} is attributed to rocking Si-O-Si vibration, where the oxygen moves perpendicular to the Si-O-Si plane.[28] And the band at around 800cm^{-1} is identified as bending Si-O-Si vibration, in which the oxygen moves normal to the Si-Si line and remains in the Si-O-Si plane. The band located at 1070cm^{-1} is mainly associated with the asymmetric stretching Si-O-Si mode, where the oxygen moves roughly parallel to the Si-Si line.[29] In addition, the peaks at 671cm^{-1} and 1384cm^{-1} can be attributed to bending vibration and stretching vibration of B-O bond, respectively.[30, 31] The peak centred at 900cm^{-1} relates to the mode from Si-O with non-bridging oxygen (Si-O-NBO).[29] Therefore, the modified ions have been successfully introduced into the amorphous network with the sol-gel method. What is more, there is no any peaks related to the organic group, which means all of them should have been fully removed in the Amorphous phase-1 powder calcined at 700°C.

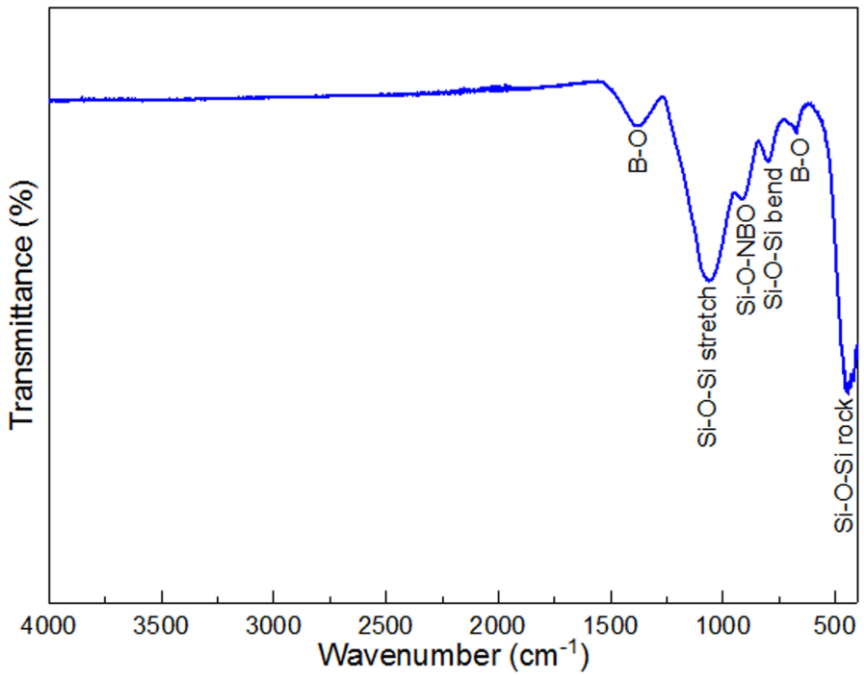

Fig. 3-2 Attenuated total reflectance Fourier transform infrared (ATR-FTIR) spectroscopy of the Amorphous phase-1 powder calcined at 700°C from 4000cm^{-1} to 400cm^{-1}.

The chemical composition of the Amorphous phase-1 powder calcined at 700°C is presented

in Tab. 3-1. The characterized chemical composition of this sol-gel derived amorphous phase is consistent with nominal one. In particular, there is no evaporation of low melting point elements, such as boron, during the synthesis. Compared with the glasses fabricated by the melt-quench method,[14] this amorphous phase synthesized by the sol-gel method has shown evident advantage in remaining stable chemical composition.

Tab. 3-1 Comparison of nominal composition and characterized composition of Amorphous phase-1.

Components	Nominal composition (mol%)	Characterization results (mol%)
Na_2O	0.78	0.81
K_2O	2.33	2.41
CaO	2.33	2.50
SiO_2	80.01	79.51
B_2O_3	14.55	14.77

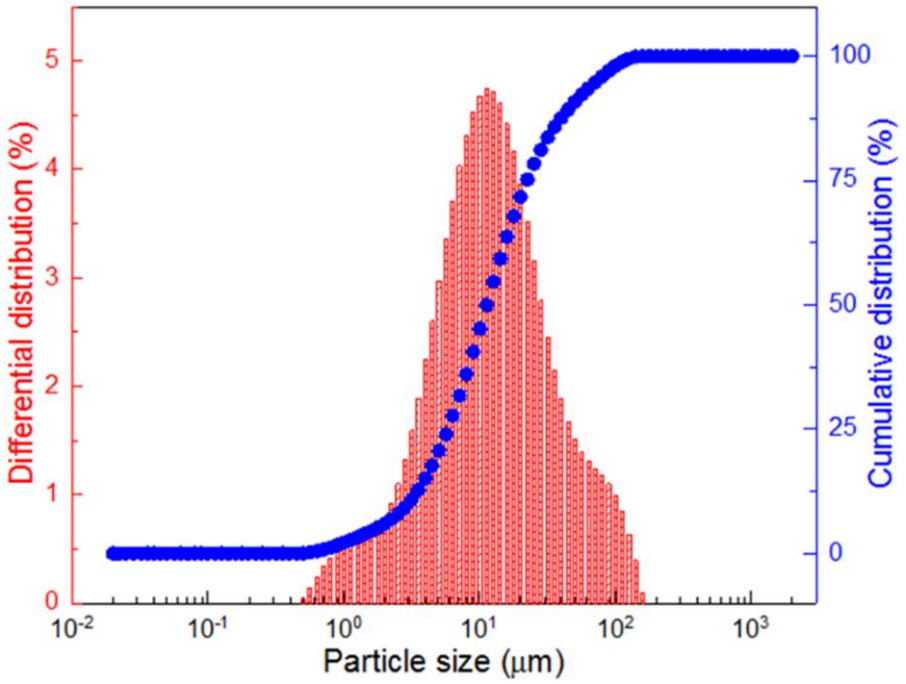

Fig. 3-3 Particle size distribution of the Amorphous phase-1 powders calcined at 700°C.

The particle size distribution of calcined Amorphous phase-1 powder is further characterized

in Fig. 3-3. It can be seen that the diameter of majority particle is ~10μm according to the differential distribution characterization and the mean size is 19.4μm. Based on the cumulative distribution characterization, 50% particle is with the size below 11.2μm.

The as-synthesized Amorphous phase-1 powder can be used in amorphous phase/ceramic based composites for LTCC application owing to its low softening temperature based on thermogravimetric-differential thermal analysis (TG-DTA) characterization. As illustrated in Fig. 3-4, there is no weight loss from room temperature to 950°C, which implies the organics have been completely removed after calcination. And this is consistent with the ATR-FTIR characterization that no any peak related to the organic group appears. The transition temperature and the softening temperature should be 745°C and 795°C, respectively. This low softening temperature implies that it can turn into vacuous liquid at this point and densify the ceramic during sintering. After 795°C, the amorphous phase begins to get crystallized with a characteristic exothermic process.

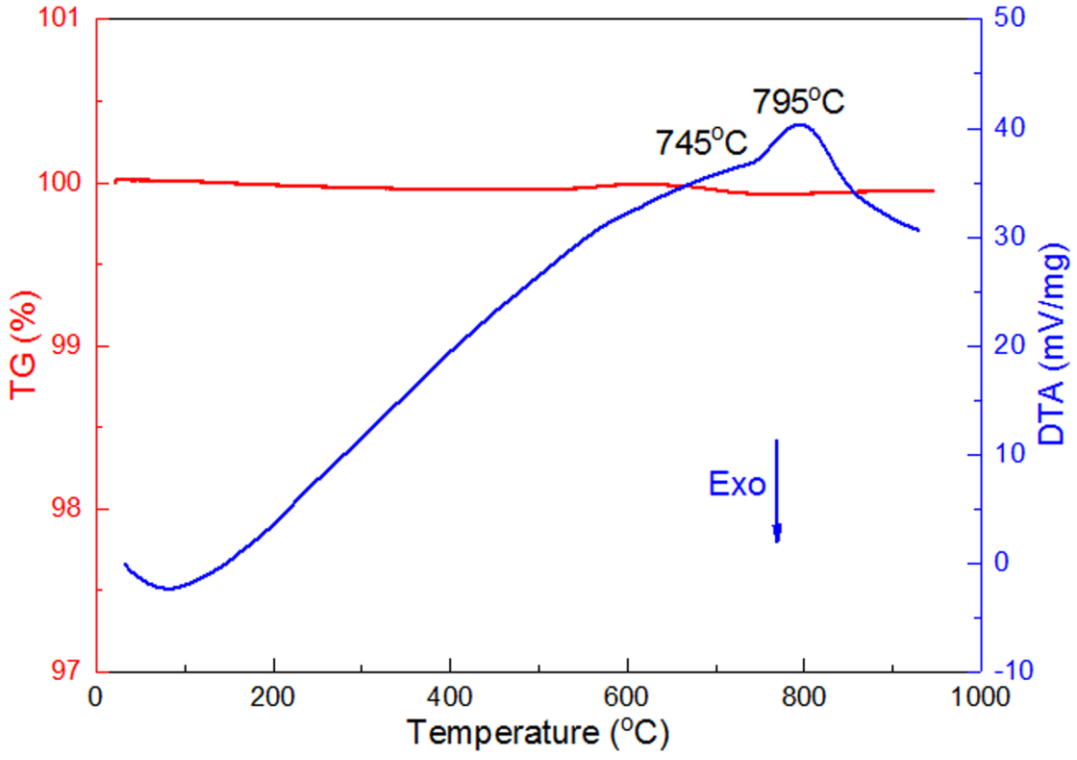

Fig. 3-4 Thermogravimetric-differential thermal analysis (TG-DTA) characterization of Amorphous phase-1 powder calcined at 700°C.

3.2.2 Amorphous phase-2

Synthesis of Amorphous phase-2

The nominal composition of Amorphous phase-2 is 81.06% SiO_2-0.28% Na_2O-0.85% K_2O-3.40% CaO-5.09% BaO-9.32% B_2O_3 (in mole ratio). It was synthesized using the sol-gel method with following procedures. Tetraethyl orthosilicate (TEOS, 98%, Sigma-Aldrich) was mixed with ethanol and deionized water with the volume of 9mL, 100mL and 9mL, respectively. Then HNO_3 (70%, Ajax Finechem Pty LTD.) was added to above solution to adjust pH value to 1~2 for the sake of hydrolysis. Until the clear solution appeared, 0.024g $NaNO_3$ (≥99.999%, Sigma-Aldrich), 0.084g KNO_3 (Analytical reagent, The British drug houses LTD.), 0.393g $Ca(NO_3)_2 \cdot 4H_2O$ (≥98%, The British drug houses LTD.), 0.652g $Ba(NO_3)_2$ (≥99%, Sigma-Aldrich) and 0.565g H_3BO_3 (≥99.5%, The British drug houses LTD.) were added. Next adjust the pH value of the mixed solution to ~7 with ammonia solution (35%, The British drug houses LTD.) and the gel formed. After dried at 60°C, the xerogel containing Si, Na, K, Ca, Ba and B was obtained. The final powders were achieved by calcining the xerogel between 600°C and 800°C with the heating rate of 2°C/min.

Structures and properties of Amorphous phase-2

The structure of the as-synthesized Amorphous phase-2 xerogel and that calcined between 600°C and 800°C are characterized by XRD in Fig. 3-5. It can be seen the powder calcined at 600°C for 2h shows a broad hump peak in the range from 15° to 35° without any crystal peak. However, a small crystal peak at 27° appears when calcined at 700°C for 2h. This peak remains there even calcined at 600°C for 12h. A more evident crystal peak comes out at 22° when sintered at 800°C for 2h. This result indicates that the xerogel calcined at 600°C for 2h is of typical amorphous structure, while it begins to get crystallized at higher temperature or at 600°C for a loner time. Therefore, the powders calcined at 600°C for 2h is selected for further work.

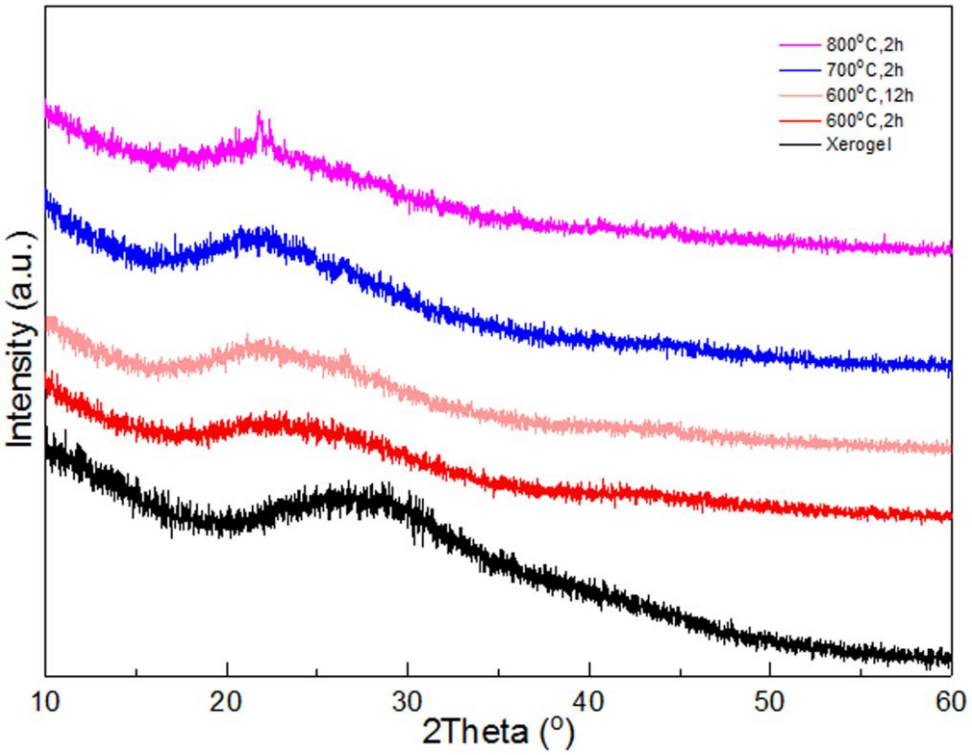

Fig. 3-5 XRD patterns of the Amorphous phase-2 xerogel and that calcined between 600°C and 800°C.

Fig. 3-6 presents the ATR-FTIR spectroscopy of Amorphous phase-2 powder calcined at 600°C from 4000cm^{-1} to 400cm^{-1}. Three main peaks in the region between 450cm^{-1} and 1300cm^{-1} are related to the Si-O-Si vibration modes. In detail, the peak centred at 460cm^{-1} is attributed to rocking Si-O-Si vibration, where the oxygen moves perpendicular to the Si-O-Si plane.[28] And the band at around 800cm^{-1} is identified as bending Si-O-Si vibration, in which the oxygen moves normal to the Si-Si line but remains in the Si-O-Si plane. The band located at 1070cm^{-1} is mainly associated with the asymmetric stretching Si-O-Si mode, where the oxygen moves roughly parallel to the Si-Si line.[29] The peaks at 671cm^{-1} and 1384cm^{-1} can be attributed to vibration of B-O bond.[30] The band at 900cm^{-1} is concerned with the mode from Si-O with non-bridging oxygen (Si-O-NBO).[29]

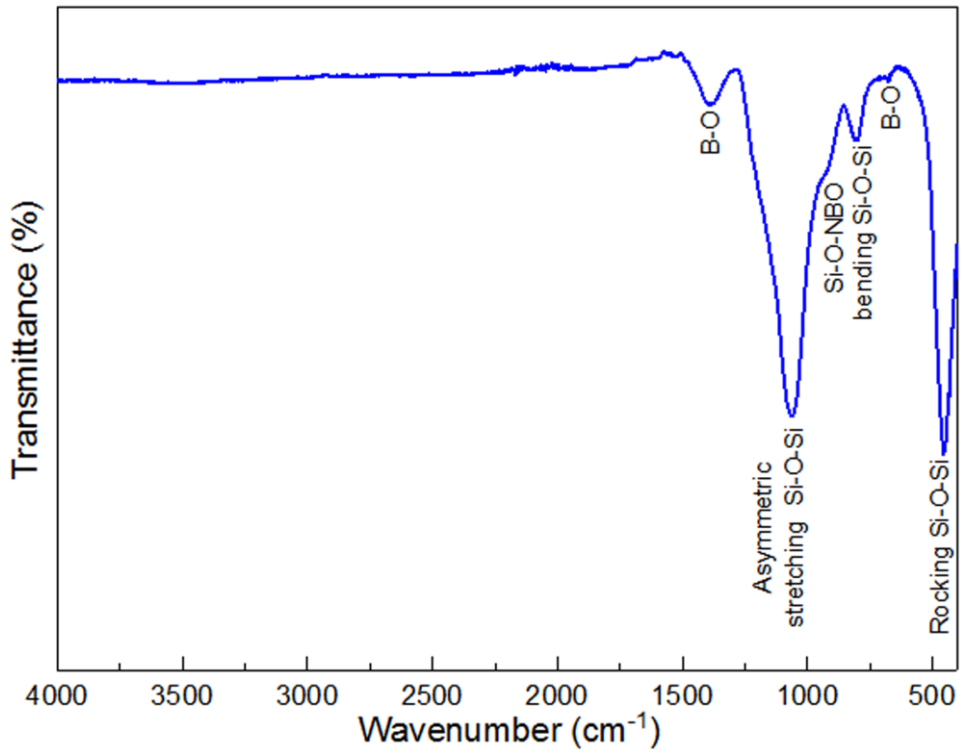

Fig. 3-6 Attenuated total reflectance Fourier transform infrared (ATR-FTIR) spectroscopy of Amorphous phase-2 powder calcined at 600°C from 4000cm^{-1} to 400cm^{-1}.

The chemical composition of the Amorphous phase-2 powder calcined at 600°C is shown in Tab. 3-2. Similar with the sol-gel derived Amorphous phase-1, no evaporation of any low melting point elements happened during the synthesis process. In addition, the identified composition is consistent with the nominal one.

Tab. 3-2 Comparison of nominal composition and characterized composition of Amorphous phase-2.

Components	Nominal composition (mol%)	Characterization results (mol%)
Na_2O	0.28	0.27
K_2O	0.85	0.87
CaO	3.40	3.45
BaO	5.09	5.25
SiO_2	81.06	80.78

B_2O_3	9.32	9.38

The particle size distribution of the Amorphous phase-2 powder calcined at 600°C for 2h is shown in Fig. 3-7. It illustrates that the diameters of the majority particles are concentrated in the range between 10μm and 40μm based on the differential distribution results. And the mean particle size is about 29μm. In addition, 50% of the particles are with size below 17.7μm according to the cumulative distribution results.

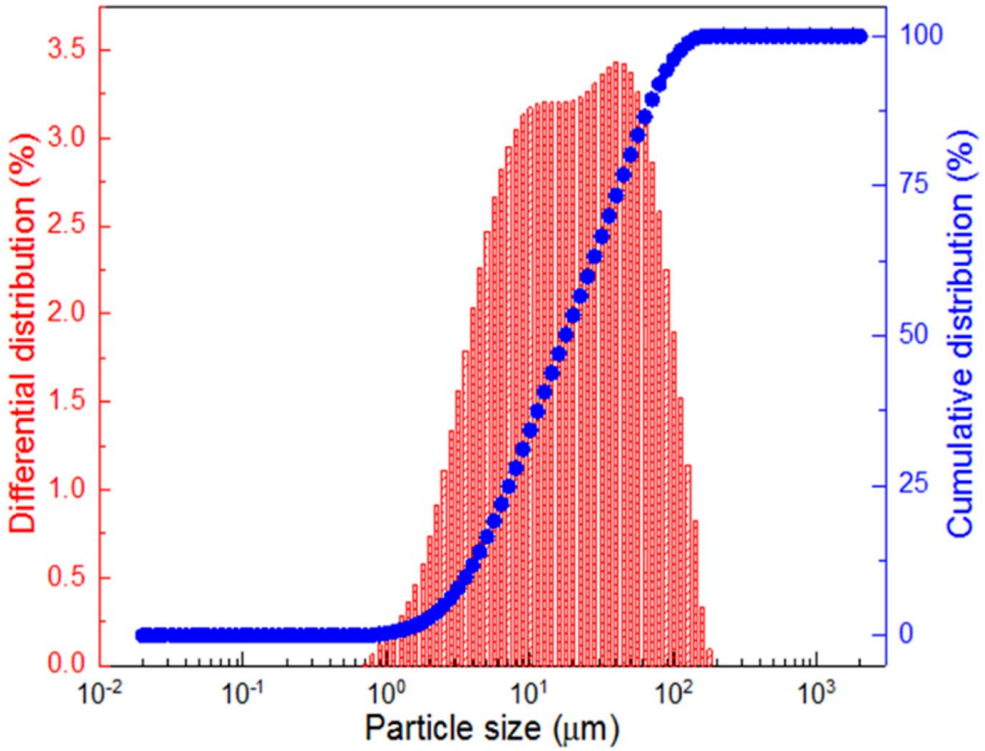

Fig. 3-7 Particle size distribution of the Amorphous phase-2 powder calcined at 600°C for 2h.

The calcined Amorphous phase-2 powder is suitable for the LTCC application since it possesses low softening temperature. The thermal property of the calcined powder is characterized by the thermogravimetric-differential thermal analyses (TG-DTA) in Fig. 3-8. In terms of the TG curve, around 2% mass loss of the sample is happened below 250°C, which mainly attributes to desorption of the water on the particle surface. And 0.3% weight loss between 600°C and 700°C should be caused by the residual organics. According to the DTA

curve, the transition temperature is ~728°C. The endothermic peak at about 789°C can be attributed to the softening temperature, at which it forms low viscous liquid and densifies the ceramic. After this temperature, the amorphous phase begins to get crystallized and the exothermic peak located at 898°C is concerning with the crystallization process, which features the release of heat due to lower free energy of crystal.

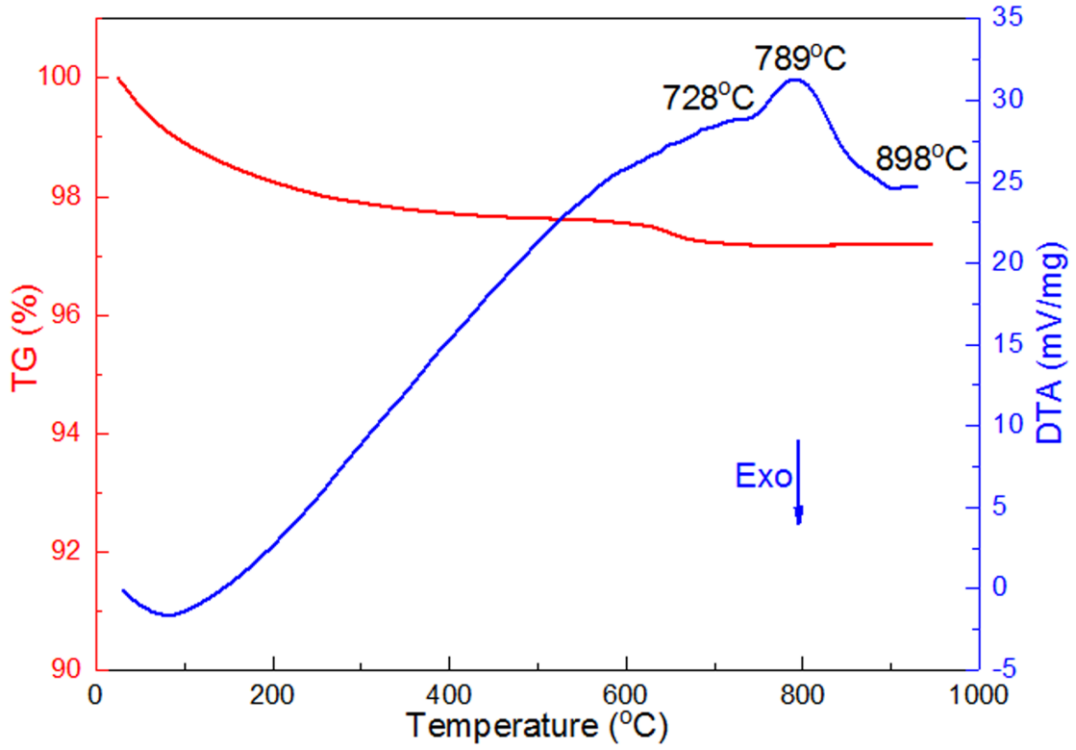

Fig. 3-8 Thermogravimetric-differential thermal analyses (TG-DTA) curve of the calcined Amorphous phase-2 powder at the heating rate of 10°C/min.

3.3 Synthesis, structure and performance of Amorphous phase-1/Al_2O_3 composite

3.3.1 Synthesis of Amorphous phase-1/Al_2O_3 composite

In order to mix well, 49.81wt% Al_2O_3 (99.9%, 135nm, US Research Nanomaterials, Inc.) and 50.19wt% Amorphous phase-1 powder (obtained in 3.2.1) were ball milled in Teflon jars for 15h. The powder mixture was uniaxially pressed at 7MPa to make into pellets with the diameter of 13mm. The green pellets were then sintered between 850°C and 900°C for 6h with the

heating rate of 3°C/min. To check the compatibility with silver electrode, the raw materials were granulated with 5wt% polyvinyl butyral (PVB) and then pressed into pellets under the uniaxial pressure of 7MPa. Afterwards, the silver paste was coated on the surfaces of the green pellets followed by co-firing at 450°C for 2h to burn out the binders. Finally, the samples were heated between 850°C and 900°C and then naturally cooled to room temperature.

3.3.2 Structure and performance of Amorphous phase-1/Al_2O_3 composite

The dielectric properties and resistivities of the Amorphous phase-1/Al_2O_3 composite are characterized in Fig. 3-9. When sintered from 850°C to 900°C, the samples show dielectric constant of ~7 and dielectric loss below 0.003 at 1MHz in Fig. 3-9a. These dielectric properties are good for rapid signal transition with high fidelity. In addition, the resistivities of sintered samples in Fig. 3-9b are above $10^{13}\Omega\cdot$cm, which means they are good insulating and can prevent the coupling among adjacent components. On balance, the sintering temperature, dielectric properties and resistivity of this sol-gel derived Amorphous phase-1/Al_2O_3 composite have met the requirements for LTCC application.

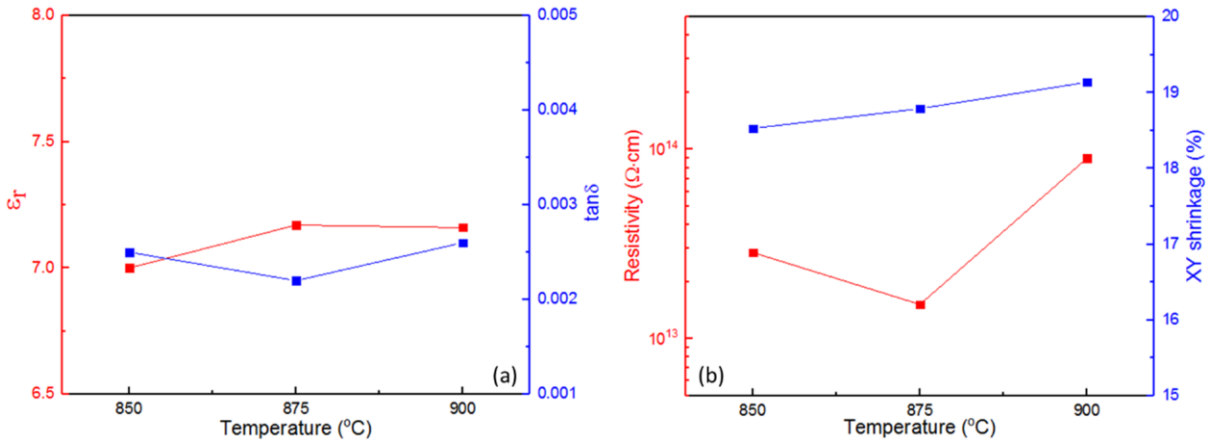

Fig. 3-9 (a) Dielectric properties (@1MHz); (b) Resistivities and XY shrinkages of samples with composition of 49.81wt% Al_2O_3 and 50.19wt% Amorphous phase-1 powder sintered from 850°C to 900°C.

The XRD patterns of the Amorphous phase-1/Al_2O_3 composite sintered from 850°C to 900°C

are shown in Fig. 3-10. Among these sintered samples, the hexagonal Al_2O_3 phase (ICSD code: 31548) remains the main phase, and the hexagonal quartz SiO_2 phase (ICSD code: 155243) is found as the secondary phase. Additionally, there is also a glassy phase left in the sintered sample according to the board hump peak from 20^o to 35^o. The quartz phase comes from the amorphous phase and the amount of the quartz phase grows with the sintering temperature increasing, which is the result of enhanced crystallization of amorphous phase at higher temperature.

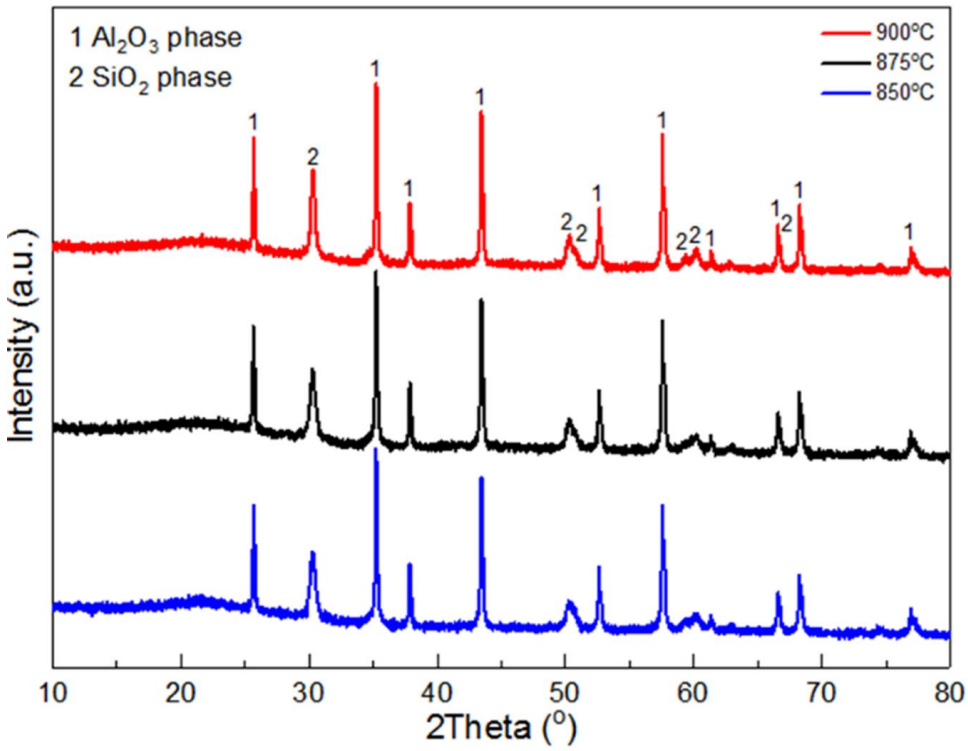

Fig. 3-10 XRD patterns of the Amorphous phase-1/Al_2O_3 composite sintered between 850^oC and 900^oC.

The microstructures of the Amorphous phase-1/Al_2O_3 composite sintered between 850^oC and 900^oC are characterized in Fig. 3-11. The microstructures of the sintered samples all show densified structures in the sintering temperature range, which is consistent with above good dielectric properties and high resistivities. Crystal particles are distributed in amorphous matrix but the corners of the particle grains remain sharp, indicating the little of them dissolved into the amorphous phase during densification.[32]

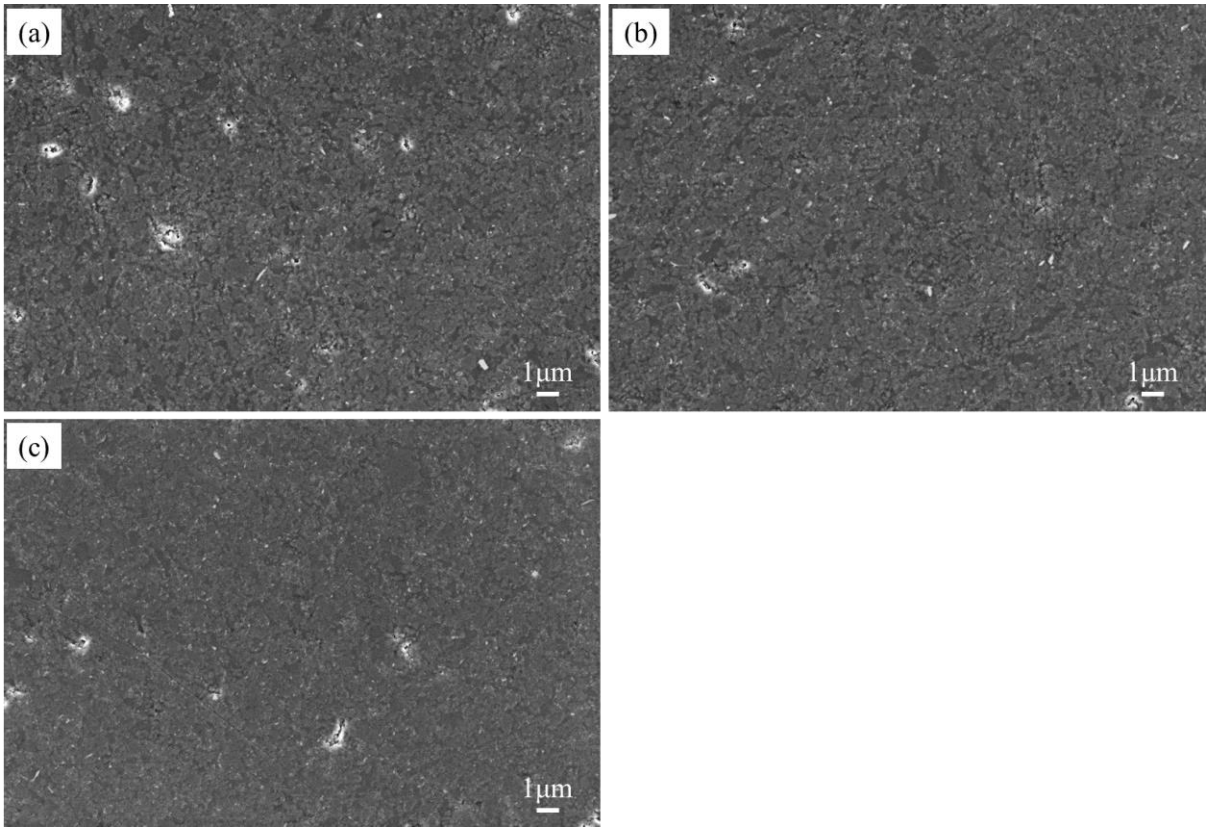

Fig. 3-11 SE image of Amorphous phase-1/Al_2O_3 composite sintered at (a) 850^oC, (b) 875 ^oC and (c) 900^oC.

Apart from above good performance, the developed Amorphous phase-1/Al_2O_3 composite is also compatible with silver electrode in the sintering temperature range. As illustrated in Fig. 3-12, the silver was tightly integrated with ceramic without obvious cracking or delamination. This means the silver conductive patterns can well attach on this LTCC composite and both of them share the similar shrinkage rate during sintering. Furthermore, the atomic percentage of silver at the spot closest to the boundary drops and is quite close to that far away from the interface when co-fired at 850^oC. Such a dramatically decreased Ag profile at the interface indicates that there is no diffusion of Ag into the ceramics. Even when co-fired at 900^oC, the atomic percentage of Ag at the interface also presents similar sharp decline profile. Therefore, the developed Amorphous phase-1/Al_2O_3 composite is compatible with the silver electrode when co-fired between 850^oC and 900^oC.

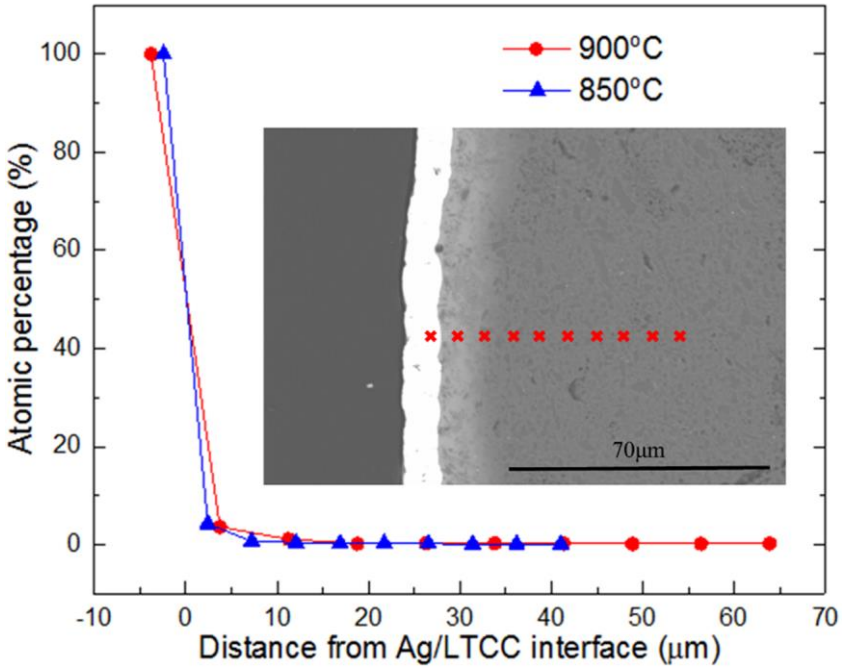

Fig. 3-12 SEM of the cross section of cofired Ag/LTCC interface and the atomic percentage of Ag at the interface.

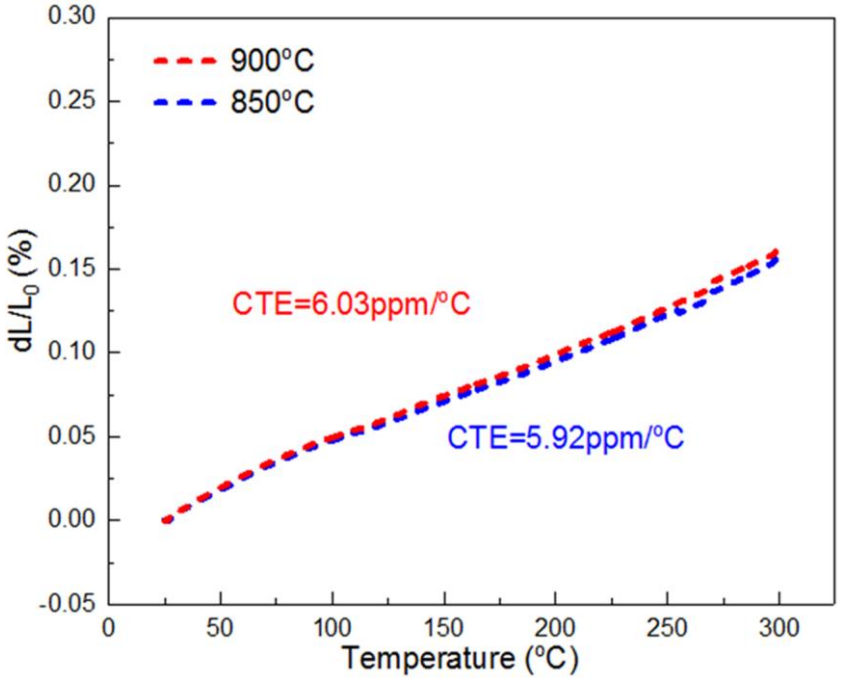

Fig. 3-13 Coefficient of thermal expansion (CTE) of Amorphous phase-1/Al_2O_3 composite sintered at 850°C and 900°C.

In real application, the chips are usually mounted on the LTCC substrates and the success of cooperation is determined by the match of their coefficients of thermal expansion. Fig. 3-13

illustrates the thermal expansion is linear without any abrupt change, which means the developed composite is quite stable and no phase change happened in this range. And the samples show the CTE of 5.92ppm/^{o}C and 6.03ppm/^{o}C when sintered at 850^{o}C and 900^{o}C, respectively. These values are quite close to that of alumina and GaAs substrates,[33, 34] which are usually used to integrate the active components. Thus, the developed Amorphous phase-1/Al_2O_3 composite can perform well with them.

3.4 Synthesis, structure and performance of Amorphous phase-2/Al_2O_3 composite

3.4.1 Synthesis of Amorphous phase-2/Al_2O_3 composite

53.35wt% Al_2O_3 (99.9%, 135nm, US Research Nanomaterials, Inc.) was ball milled with 46.65wt% as-synthesized Amorphous phase-2 powder (obtained in 3.2.2) in ethanol for 15h. Then the dried powder mixtures were pressed into cylindrical compacts with the diameter of 13mm under the uniaxial pressure of 7MPa. The green samples were sintered from 825^{o}C to 900^{o}C for 6 hours with heating rate of 3^{o}C/min. To check the compatibility with silver electrode, the raw materials were granulated with 5wt% polyvinyl butyral (PVB) and then pressed into pellets under the uniaxial pressure of 7MPa. Then the silver electrode was coated on the surfaces of the green samples followed by co-firing at 450^{o}C for 2 hours to burn out the binders. Finally, the samples were further heated from 850^{o}C to 900^{o}C and then naturally cooled to room temperature.

3.4.2 Structure and performance of Amorphous phase-2/Al_2O_3 composite

Fig. 3-14 shows the XRD patterns of the Amorphous phase-2/Al_2O_3 composite sintered between 825^{o}C and 900^{o}C. When sintered at 825^{o}C, the main phase is hexagonal Al_2O_3 phase (ICSD code: 10425) and the secondary phase is hexagonal quartz SiO_2 phase (ICSD code: 155243), respectively. These two phases remain there and the amount of the quartz phase keeps growing with the sintering temperature increasing to 875^{o}C. This quartz phase comes from the

amorphous phase and this crystallization is in favour of reducing the dielectric loss since less glassy networks left in the sintered sample. When sintered at 900°C, a new monoclinic $KAlSi_3O_8$ phase (ICSD code: 80793) appears, which should be the reaction product of amorphous phase and Al_2O_3. This reaction implies the as-synthesized amorphous phase has a good wetting condition with Al_2O_3.[35]

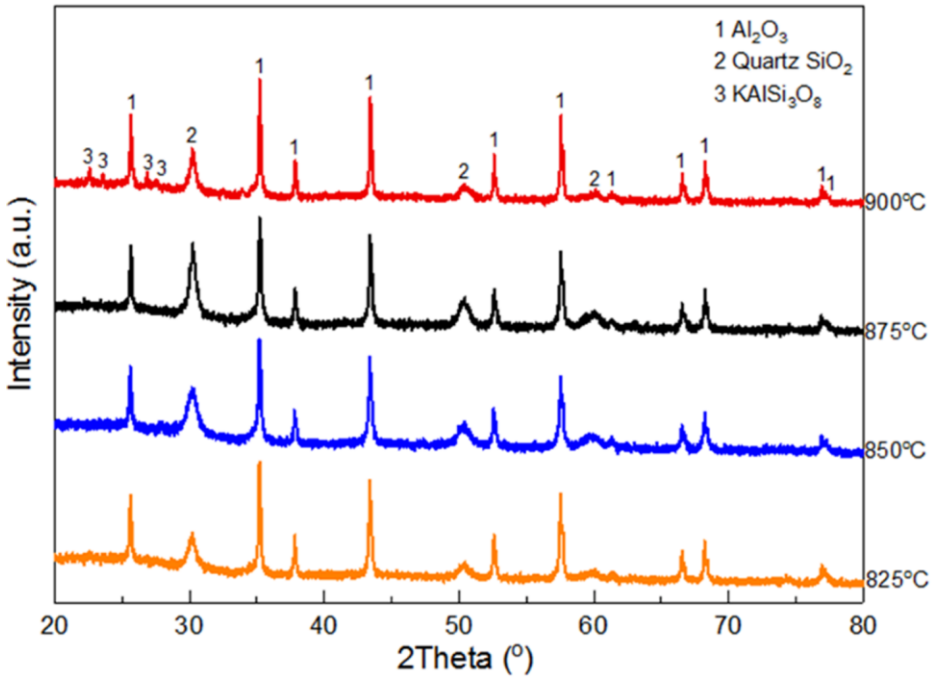

Fig. 3-14 XRD patterns of the sample with composition of 53.35wt% Al_2O_3 and 46.65wt% Amorphous phase-2 powder sintered from 825°C to 900°C.

The specimen with composition of 53.35wt% Al_2O_3 and 46.65wt% Amorphous phase-2 powder show good dielectric properties and high resistivities when sintered between 850°C and 900°C. As illustrated in Fig. 3-15a, the samples show stable dielectric constant (7~8) and low dielectric loss from 100Hz to 2MHz when sintered above 850°C. Besides, their resistivities in Fig. 3-15b are all above $10^{13}\Omega\cdot cm$, which means these samples are highly insulating. In contrast, the sample sintered at 825°C shows unstable dielectric constant and poor dielectric loss, especially in the low frequency range. And the resistivity is as low as $10^{11}\Omega\cdot cm$. As a conclusion, this Amorphous phase-2/Al_2O_3 composite has to be sintered between 850°C and 900°C.

Microstructure of the samples sintered from 825°C to 900°C are illustrate in Fig. 3-16. It can

be seen that there are some cracks in the middle part of the sample sintered at 825°C, which should be caused by insufficient sintering. And these defects should be the reason for unstable dielectric properties and poor resistivity. In contrast, the samples sintered between 850°C and 900°C all present relative densified structure with few isolated pores. Their densified microstructures are consistent with their good dielectric properties and resistivity.

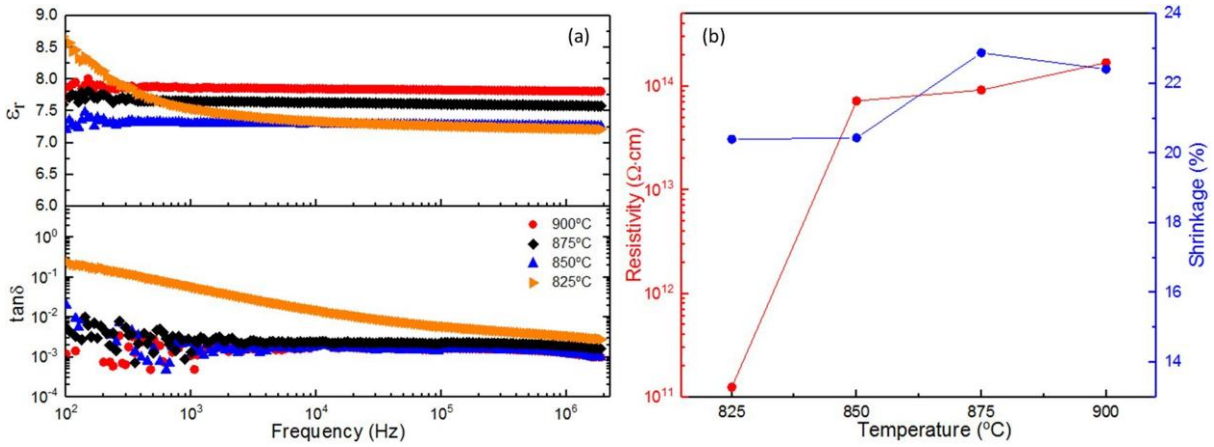

Fig. 3-15 (a) Dielectric properties of samples with composition of 53.35wt% Al_2O_3 and 46.65wt% Amorphous phase-2 powder sintered between 825°C and 900°C; (b) Resisitivities and XY shrinkages of the corresponding samples.

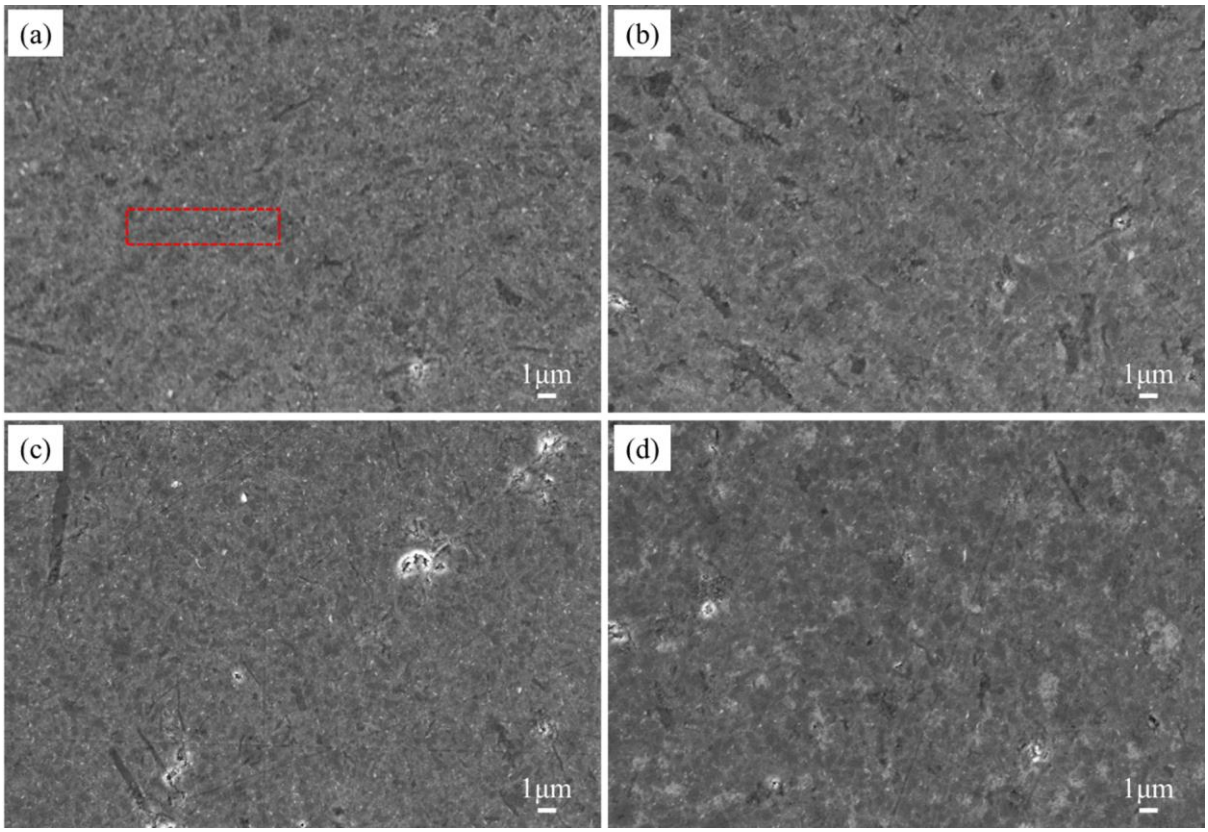

Fig. 3-16 SEM image of samples with composition of 53.35wt% Al_2O_3 and 46.65wt% Amorphous phase-2 powder sintered at (a) 825°C, (b) 850°C, (c) 875°C, (d) 900°C.

In addition to above excellent performance, the developed sample is compatible with the silver electrode in this sintering temperature range. Fig. 3-17 presents the cross section of the Ag/LTCC interface and the silver electrode is tightly integrated with ceramic without any cracking or delamination. Therefore, the firing behaviour of the Amorphous phase-2/Al_2O_3 composite matches with that of silver. Furthermore, the atomic profile of Ag decreases dramatically at the interface, which means the Ag should not diffuse into the ceramics during sintering. Consequently, this composite is compatible with co-fired Ag electrode. It is worthwhile pointing out that the accurate Ag profile might be more shaper because the profile we characterized here might be affected by smearing effect caused by soft silver electrode during polishing.

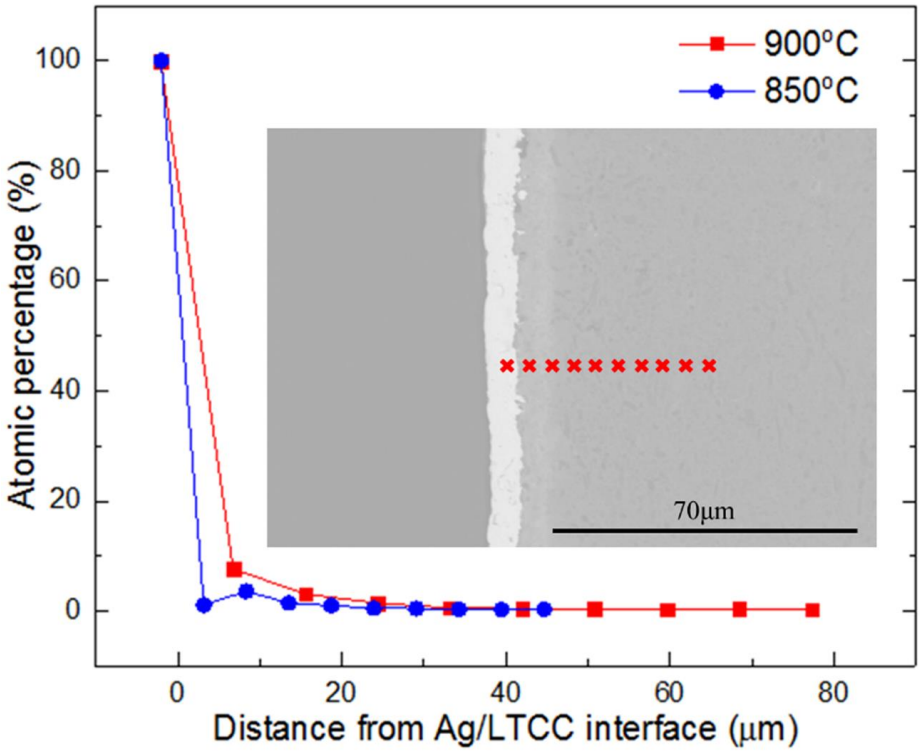

Fig. 3-17 SEM imgae of the cross section of Ag electrode/ LTCC interface and corresponding atomic percentage of Ag at the interface.

As illustrated in Fig. 3-18, the thermal expansion of developed Amorphous phase-2/Al_2O_3 composite is linear and CTE values are ~6ppm/^oC when sintered between 850^oC and 900^oC. These values match with that of alumina, so it would be reliable for the developed Amorphous phase-2/Al_2O_3 composite connecting or amounting on the alumina board.[36] As reported, the CTE of composite is determined by that of each phase present, as well as their fraction. It is worth to point out that the CTE here does not change too much in the sample sintered at 850^oC and 900^oC, although the phases present are different. This is because that the amount of $KAlSi_3O_8$ phase is quite small, as well as the ratios between Al_2O_3 phase and quartz SiO_2 phase in these samples are quite similar (in Fig. 3-14).

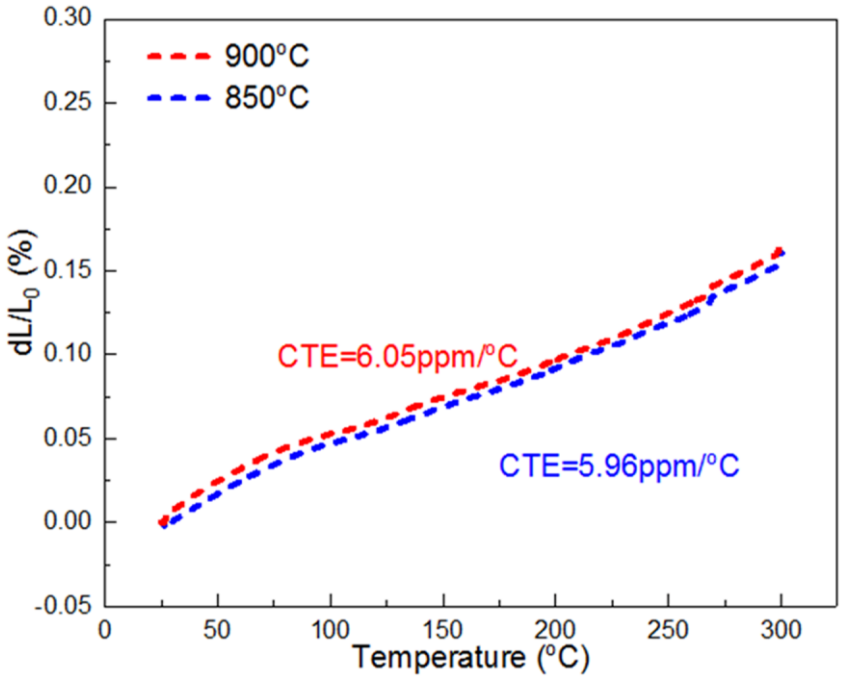

Fig. 3-18 Coefficient of thermal expansion (CTE) of samples with the composition of 53.35wt% Al_2O_3 and 46.65wt% Amorphous phase-2 powder sintered at 850^oC and 900^oC.

3.5 Conclusion

In this study, we have successfully synthesized Amorphous phase-1 and Amorphous phase-2 using the sol-gel method. Their structures, chemical compositions, particle size distributions and thermal properties have been characterized by XRD, ATR-FTIR, XRF, ICP-AES, laser scattering and TG-DTA.

With the sol-gel derived amorphous phases, we further developed two amorphous phase/Al_2O_3 composites with comprehensive and positive performance. In detail, Amorphous phase-1 is mixed with 49.81wt% Al_2O_3 for LTCC application. This composite shows dielectric constant of ~7, dielectric loss below 0.003 @1MHz, resistivity above $10^{13}\Omega\cdot$cm and coefficient of thermal expansion (CTE) of ~6ppm/^{o}C when sintered between 850^{o}C and 900^{o}C. Amorphous phase-2 is combined with 53.35wt% Al_2O_3 and sintered between 825^{o}C and 900^{o}C. It gets densified from 850^{o}C and 900^{o}C and shows dielectric constant of 7~8 @1MHz, dielectric loss below 0.002 @1MHz, resistivity above $10^{13}\Omega\cdot$cm and CTE of ~6ppm/^{o}C. Both of these two composites are compatible with silver electrode and promising for the commercial LTCC application.

At this point, we have successfully used different sol-gel derived amorphous phases and crystalline Al_2O_3 to develop LTCC materials with relative permittivity of 7~8. In the next chapter, we will use the amorphous phase with ZrO_2 and pure fused SiO_2 to developed composites with relative permittivity of 11 and 5, respectively.

Reference

1. Knickerbocker, J. U.; Andry, P. S.; Dang, B.; Horton, R. R.; Interrante, M. J.; Patel, C. S.; Polastre, R. J.; Sakuma, K.; Sirdeshmukh, R.; Sprogis, E. J.; Sri-Jayantha, S. M.; Stephens, A. M.; Topol, A. W.; Tsang, C. K.; Webb, B. C.; Wright, S. L., Three-dimensional silicon integration. *IBM Journal of Research and Development* **2008,** *52* (6), 553-569.

2. Jian-Xin Chen, Yang Zhan and Quan Xue, Novel LTCC distributed element wideband bandpass filter based on the dual mode stepped impedance resonator. *IEEE Transactions on Components, Packaging and Manufacturing Technology* **2015,** *5* (3), 372-380.

3. Wen-Hao Jiang, Jian-Hong Liu, Yin Liu, Ge Jin, Jun Zhang, Jian-Wei Pan, 1.25GHz sine wave gating InGaAs/InP single photo detector with a monolithically integrated readout circuit. *Optics Letter* **2017,** *42*, 5090-5093.

4. Zheng, P.; Liu, Z.; Ma, M.; Wang, Y.; Liu, F.; Li, Y., Kα-Band LTCC Stacked Substrate Integrated Waveguide Bandpass Filter. *Wireless Communications and Mobile Computing* **2018,** *2018*, 1-7.

5. Liu, M.; Zhou, H.-q.; Zhu, H.-k.; Yue, Z.-x.; Zhao, J.-x., Tape casting of borosilicate glass/Al_2O_3 composites for LTCC substrate with various relative molecular masses of PVB. *Journal of Central South University* **2013,** *20* (1), 37-43.

6. Zuo, H.; Tang, X.; Zhang, H.; Lai, Y.; Jing, Y.; Su, H., Low-dielectric-constant $LiAlO_2$ ceramics combined with LBSCA glass for LTCC applications. *Ceramics International* **2017,** *43* (12), 8951-8955.

7. Zeng, Q.; Li, W.; Shi, J.-l.; Guo, J.-k., Microwave Dielectric Properties of $5Li_2O$-$0.583Nb_2O_5$-$3.248TiO_2$ Ceramics with V_2O_5. *Journal of the American Ceramic Society* **2006,** *89* (10), 3305-3307.

8. Seo, Y. J.; Jung, J. H.; Cho, Y. S.; Kim, J. C.; Kang, N. K., Influences of Particle Size of Alumina Filler in an LTCC System. *Journal of the American Ceramic Society* **2007,** *90* (2), 649-652.

9. Li, B.; Qing, Z.; Li, Y.; Li, H.; Zhang, S., Effect of CaO content on structure and properties of low temperature co-fired glass–ceramic in the Li_2O–Al_2O_3–SiO_2 system. *Journal of Materials Science: Materials in Electronics* **2015,** *27* (3), 2455-2459.

10. Qing, Z.; Li, B.; Li, H.; Li, Y.; Zhang, S., Fabrication and properties of Li_2O–Al_2O_3–SiO_2 glass/Al_2O_3 composites for low temperature co-fired ceramic applications. *Journal of Materials Science: Materials in Electronics* **2014,** *26* (3), 1789-1794.

11. Katsumasa Yasukawa, Yoshitake Terashi and Akira Nakayama, Crystallinity analysis of glass-ceramics by the Rietveld method. *J. Am. Ceram. Soc.* **1998,** *81*, 2978-82.

12. Sebastian, M. T.; Jantunen, H., Low loss dielectric materials for LTCC applications: a review. *International Materials Reviews* **2013,** *53* (2), 57-90.

13. Shao, H.; Zhou, H.; Zhu, H.; Shen, X., Preparation and properties of crystallizable Glass/Al_2O_3 composites for LTCC material. *Journal of Wuhan University of Technology-Mater. Sci. Ed.* **2011,** *26* (6), 1174-1178.

14. Ashis Kumar Mandal, Prasanta Kumar Sinha, Santanu Sen, Sitendu Mondal, Chandan Guha and Ranjan Sen, Microwave preparation of SiO_2-B_2O_3-Na_2O-K_2O-CaO-Fe_2O_3-TiO_2 glass system. *J. Chem. Chem. Eng.* **2014,** *8*, 349-357.

15. Takashi Hayashi, Hajime Saito, Preparation of CaO-SiO_2 glasses by the gel method. *JOURNAL OF MATERIALS SCIENCE* **1980,** *15*, 1971-1977.

16. Abhilash, P.; Thomas, D.; Surendran, K. P.; Sebastian, M. T.; Pinckney, L., Facile Synthesis of “Quench-Free Glass” and Ceramic-Glass Composite for LTCC Applications. *Journal of the American Ceramic Society* **2013,** *96* (5), 1533-1537.

17. Dislich, H., New routes to multicomponent oxide glasses. *Angew. Chem. internat. Edit.* **1971,** *10*, 363-370.

18. Dileep Kumar, C. J.; Sunny, E. K.; Raghu, N.; Venkataramani, N.; Kulkarni, A. R., Synthesis and Characterization of Crystallizable Anorthite-Based Glass for a Low-Temperature Cofired Ceramic Application. *Journal of the American Ceramic Society* **2008,** *91* (2), 652-655.

19. Imanaka, Y., *Multilayered low temperature cofired ceramics technology*. Springer US: 2005; p 229.

20. Liu, M.; Zhou, H.; Zhu, H.; Yue, Z.; Zhao, J., Microstructure and dielectric properties of glass/Al_2O_3 composites with various low softening point borosilicate glasses. *Journal of Materials Science: Materials in Electronics* **2012,** *23* (12), 2130-2139.

21. Louis Navias and R. L. Green, Dielectric properties of glasses at ultra-high frequencies and their relation to composition. *Journal of the Americun Ceramic Society* **1946,** *29*, 267-276.

22. Rajesh, S.; Jantunen, H.; Letz, M.; Pichler-Willhelm, S., Low Temperature Sintering and Dielectric Properties of Alumina-Filled Glass Composites for LTCC Applications. *International Journal of Applied Ceramic Technology* **2012,** *9* (1), 52-59.

23. Hamieh T, Kawtharani F., Kassas A, Quercioli R, Houivet D, Bernard J, Lakiss H, Toufaily J, Aoun R and Reda M, Ultrafine Grinding of $MgTiO_3$ Based Ceramic Influencing the Material Properties. *Journal of Physical Chemistry & Biophysics* **2013,** *03* (03), 13.

24. Seong-Hun Choe, Shuji Tanaka and Masayoshi Esashi, A Matched Expansion MEMS Probe Card with Low CTE LTCC Substrate. In *2007 IEEE International Test Conference*, IEEE: Santa Clara, CA, USA, 2007; pp 1-6.

25. Qing, Z.; Li, B.; Li, H.; Li, Y.; Zhang, S., Effects of MgO on properties of Li_2O–Al_2O_3–SiO_2 glass–ceramics for LTCC applications. *Journal of Materials Science: Materials in Electronics* **2014,** *25* (5), 2149-2154.

26. Zhu, H.; Fu, R.; Agathopoulos, S.; Fang, J.; Li, G.; He, Q., Crystallization behaviour and properties of BaO-CaO-B_2O_3-SiO_2 glasses and glass-ceramics for LTCC applications. *Ceramics International* **2018,** *44* (9), 10147-10153.

27. Hitishi Ohsato, Tsutomu Tsunooka, Minato Ando, Yoshihiro Ohishi, Yasuharu Miyauchi and Ken-ichi Kakimoto, Millimeter-wave dielectric ceramics of alumina and forsterite with high quality factor and low dielectric constant. *Journal of the Korean Ceramic Society* **2003,** *40*, 350-353.

28. Innocenzi, P., Infrared spectroscopy of sol-gel derived silica-based films: a spectra microstructure overiew. *Journal of non-crystalline solids* **2003,** *316*, 309-319.

29. Aguiar, H.; Serra, J.; González, P.; León, B., Structural study of sol–gel silicate glasses by IR and Raman spectroscopies. *Journal of Non-Crystalline Solids* **2009,** *355* (8), 475-480.

30. Rivera, E.; Prado, M. O.; Nuñez, M., Adherence of Molecules to Silica Glass Surface: Experimental Results and Theoretical Calculations. *Physics Procedia* **2013,** *48*, 206-213.

31. M. Toderas, S. Filip, I. Ardelean, Structural study of the Fe_2O_3-B_2O_3-BaO glass system by FTIR spectroscopy. *Journal of Optoelectronics and Advanced Materials* **2006,** *8*, 1121 - 1123.

32. Jau-ho Jean, T. K. Gupta, Liquid-phase sintering in the glass-cordierite system. *Journal of Materials Science* **1992,** *27*, 1575-1584.

33. Pierron, E. D.; Parker, D. L.; McNeely, J. B., Coefficient of Expansion of GaAs, GaP and Ga(As, P) Compounds from −62° to 200 ℃. *Journal of Applied Physics* **1967,** *38* (12), 4669-4671.

34. Vadim Gektin, Avram Bar-Cohen and Sorin Witzman, Coffin-Manson Based Fatigue Analysis of Underfilled DCAs. *IEEE Trans. Compon. Packag. Technol. A* **1998,** *21A*, 577-584.

35. Chen, X.; Zhang, W.; Bai, S.; Du, Y., Densification and characterization of SiO_2-B_2O_3-CaO-MgO glass/Al_2O_3 composites for LTCC application. *Ceramics International* **2013,** *39* (6), 6355-6361.

36. Turnmala, R. R., Ceramic and glass-ceramic packaging in the 1990s. *J. Am. Ceram. Soc.* **1991,** *74*, 895-908.

Chapter 4 Tuning of dielectric constant for amorphous phase-based composites

The previous chapter focused on the development of two LTCC materials with dielectric constant of 7~8 (@1MHz) based on the crystalline Al_2O_3 and two amorphous phases synthesized by sol-gel method. The materials with different dielectric constants are also highly demanded for applications in design of high frequency circuits and high speed communication. In this chapter, we will develop the amorphous phase-based composites with the dielectric constant around 11 and 5 for the LTCC applications. The amorphous phase used in this chapter is the sol-gel derived Amorphous phase-1, whose relative permittivity is around 6.2 at 1MHz. According to the empirical formula (in 1.3.2), the composites with the relative permittivity around 11 and 5 are achievable via mixing Amorphous phase-1 with ZrO_2 (ε_r=20) and pure fused SiO_2 (ε_r=4), respectively.

4.1 Monoclinic ZrO_2 for composite with high dielectric constant

4.1.1 Background

LTCC technology is becoming the mainstream in the field of industry components integration.[1, 2] Due to the restriction of low sintering temperature, the choice of materials can be used for LTCC application is rather few. Among reported materials, the glass/ceramic composites, which are composed of a glassy phase and ceramic material, have played a vital role in the LTCC application.[3, 4] Herein the glass is fabricated by the melt-quench method which usually induces unstable compositions. To resolve this deficiency, we have successfully synthesized the amorphous phases by the sol-gel method in Chapter 3.

Apart from the amorphous phase, the ceramic material is another important component in the LTCC composite, showing the complicated impacts on the sintering temperature, crystallization and dielectric properties.[5] For example, ceramic materials with diverse particle size require various amount of the amorphous phases for densification and crystallization process due to different specific surface areas.[6] In addition, it is of great significance to select

the suitable polymorph of the ceramic materials. Taking the alumina as an example, it contains several polymorphs, such as cubic (γ-Al_2O_3), monoclinic (θ-Al_2O_3) and hexagonal (α-Al_2O_3) phase.[7] And the one most widely used is the hexagonal (α-Al_2O_3) phase with relative permittivity of 10 and low dielectric loss of 0.0002 at 1MHz.

Similar to Al_2O_3, ZrO_2 is also a compound with the good dielectric properties. It can exist in three crystalline structures, that is, monoclinic, tetragonal and cubic phase, and they have the relative permittivity of 20, 47 and 37, respectively.[8] The monoclinic phase is stable at room temperature, while the monoclinic-to-tetragonal and tetragonal-to-cubic phase transitions occur at 1150^{o}C and 2400^{o}C, respectively.[9] Although the cubic and tetragonal phases of ZrO_2 can be stabilized at room temperature via chemical modification, the lattice defects, such as oxygen vacancies, often cause high dielectric loss and electrical conductivity.[10, 11] Thus, pure monoclinic ZrO_2 is more commonly used. Most of the research about the ZrO_2 in LTCC application is focused on the glass-ceramics composite, where the ZrO_2 is added as a component of glass to work as the nucleating agent.[12-15] Cho (2009) introduced the ZrO_2 as the ceramic filler into the specific calcium aluminoborosilicate glass.[16] However, the performance is still not good enough (dielectric loss is ~0.006) for commercial application and it lacks of detailed investigation of ZrO_2 on crystallization process, dielectric and thermal properties. In addition, the glassy phases in these reports are synthesized by the melt-quench method and the evaporation of some glass components, such as B_2O_3, are not prevented during melting process, which means the composition of the resultant glass possibly has a divergence with the nominal value.[17, 18]

In this section, we used Amorphous phase-1, which had been fabricated by the sol-gel method in Chapter 3, and monoclinic ZrO_2 to develop the composite with relative permittivity of ~11 for application in high frequency circuits. We started from the composition of ZrO_2: Amorphous phase-1=49.81: 50.19 (mass ratio), which is based on the previously developed Al_2O_3/Amorphous phase-1 composite (in Chapter 3), replacing the Al_2O_3 by the same amount of ZrO_2. Moreover, we have conducted a series of investigations to optimize the ratio between the ZrO_2 and Amorphous phase-1 in the composites and synthesis conditions, and finally obtained the sample with balanced performance which are suitable for LTCC commercial

application.

4.1.2 Synthesis of the ZrO_2/amorphous phase composite

Various amount of ZrO_2 (99%, Sigma-Aldrich) and Amorphous phase-1 powder (obtained in Chapter 3) were ball milled in Teflon jars for 15h. The dried powder mixture was uniaxially pressed at 7MPa into pellets with the diameter of 13mm. The green pellets were then sintered at 850^{o}C for 0.5h~6h with the heating rate of 3^{o}C/min. To check the compatibility with silver electrode, the raw materials were granulated with 5wt% polyvinyl butyral (PVB) and then pressed into pellets under the uniaxial pressure of 7MPa. Afterwards, the silver paste was coated on the surfaces of the green samples followed by co-firing at 450^{o}C for 2h to burn out the binders. Finally, the samples were further heated at 850^{o}C for 0.5h and then naturally cooled to room temperature.

4.1.3 Compositions, structures and properties of ZrO_2/amorphous phase composite

Fig. 4-1 shows the XRD patterns of samples with different ZrO_2/Amorphous phase-1 ratios sintered at 850^{o}C for 6h. For the sintered sample with the mass ratio of ZrO_2: Amorphous phase-1=49.81: 50.19, the main phase can be identified as the monoclinic ZrO_2 (ICSD collection code: 172161) and the secondary phase is the tetragonal cristobalite (C-SiO_2, ICSD collection code: 34933), as well as small amount of tetragonal zircon phase ($ZrSiO_4$, ICSD collection code: 96090). When the proportion of ZrO_2 in raw materials increases to 55%, the relative peak intensities which are associated with the cristobalite phase, labelled in 2 in Fig. 4-1, drop and those from the $ZrSiO_4$ are barely observed. Because the cristobalite is one polymorph of SiO_2, this phase is mainly originated from the Amorphous phase-1. Moreover, it seems that the decrease of cristobalite phase's peak intensity is resulted from reducing proportion of Amorphous phase-1 in raw materials. Therefore, we deduce that the amount of Amorphous phase-1 used in the raw materials determines the resultant cristobalite phase. It is reported that ZrO_2 is more inclined to react with the cristobalite phase compared with the amorphous SiO_2 to produce $ZrSiO_4$ phase.[19] As a result, the $ZrSiO_4$ phase possibly is the

product of reaction between ZrO_2 and the cristobalite phase. And the decrease of cristobalite phase in the series of samples should be the reason for the disappearance of the $ZrSiO_4$ phase.

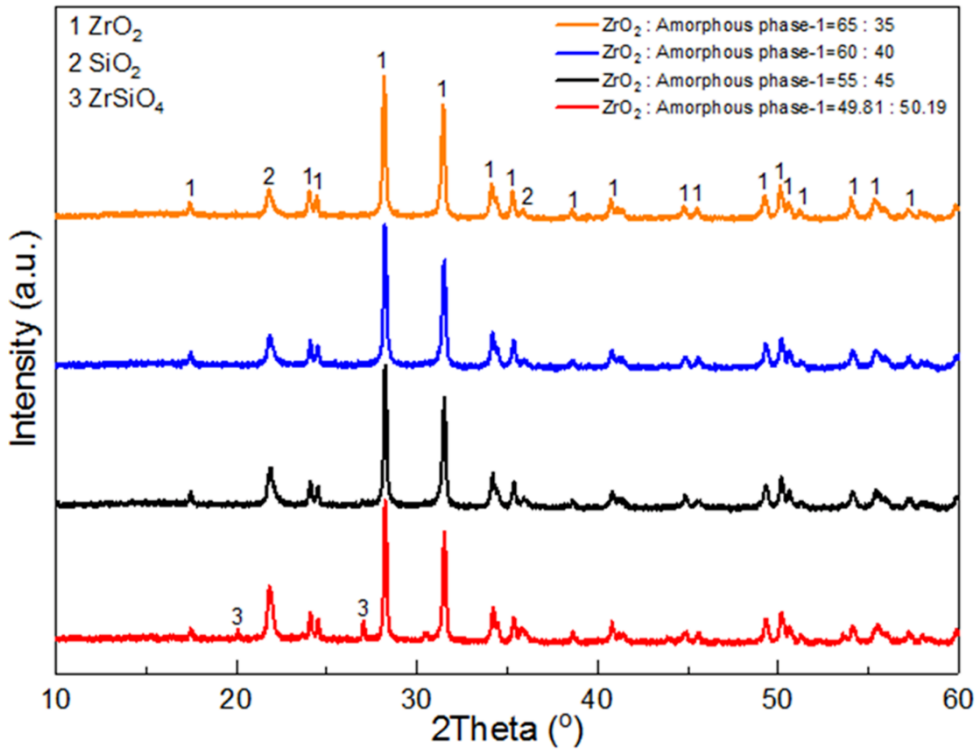

Fig. 4-1 XRD patterns of samples with various ZrO_2/Amorphous phase-1 ratio sintered at 850°C for 6h.

The electrical properties of sintered samples with various ZrO_2/Amorphous phase-1 ratio are shown in Fig. 4-2. It can be seen in Fig. 4-2a that the dielectric constant increases as the amount of ZrO_2 in the staring materials increasing. Compared with the ZrO_2 whose relative permittivity is as high as 20, the ε_r of C-SiO_2 and $ZrSiO_4$ phase are quite small, around 4 and 10.5 respectively.[20, 21] In the XRD patterns, it can be obtained that relative peak intensities of C-SiO_2 and $ZrSiO_4$ phase become weak, denoting the decreasing phase fractions, when increasing the ZrO_2/Amorphous phase-1 ratio in raw material. According to the empirical formula, the relative permittivity of a composite depends on the dielectric constant of each phase and their fractions.[22] Therefore, the variation of the dielectric constant is in consistent with the XRD analyses. In addition, the dielectric loss remains in the low level no matter how much ZrO_2 involved. Besides, the percentage of ZrO_2 shows influence on the resistivity in Fig. 4-2b.

Among the four ZrO_2/Amorphous phase-1 ratios, the resistivity of the sample reaches the maximum value when 55% ZrO_2 is introduced and gradually decreases with more amount of ZrO_2.

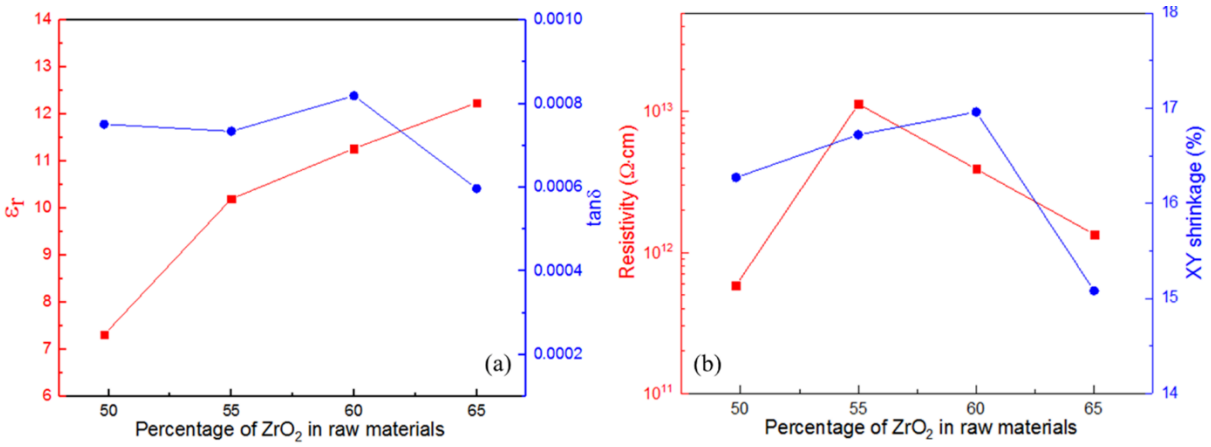

Fig. 4-2 (a) Dielectric properties (@1MHz) and (b) Resistivities (100V, DC) and XY shrinkages of samples with various amount of ZrO_2 in the raw materials and sintered at 850°C for 6h.

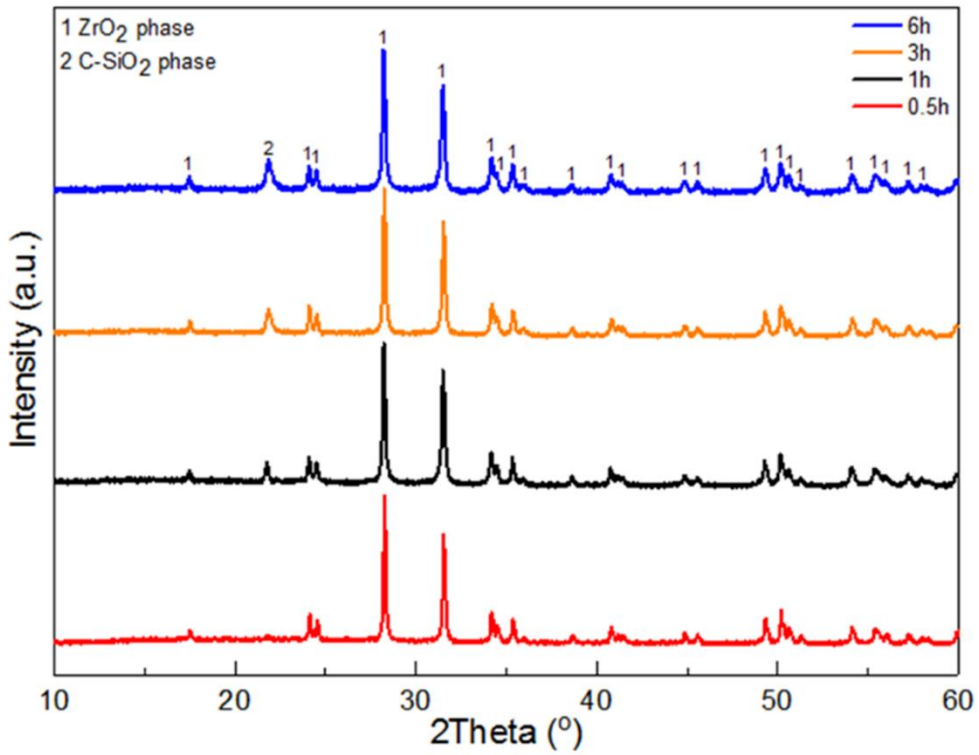

Fig. 4-3 XRD patterns of sampls with composition of ZrO_2: Amorphous phase-1= 60: 40

sintered at 850°C with soaking period from 0.5h to 6h.

For above compositions, although they show good dielectric properties and high resistivities, the undesired cristobalite phase remains in the sintered sample (in Fig. 4-1). The presence of the cristobalite phase would hinder its application for LTCC because of its high coefficient of thermal expansion of 50×10^{-6}/°C. Since the sample with the composition of ZrO_2: Amorphous phase-1=60: 40 (mass ratio) shows the dielectric constant we desired and high resistivity, we will adopt this composition and further optimize its resultant phase composition by reducing the soaking period. It can be seen in Fig. 4-3 that the cristobalite phase in the sintered sample can be inhibited by reducing the soaking period as its peaks' intensities reduce with decreasing of the sintering time. Moreover, the peak associated with the cristobalite phase is hardly obtained when the soaking period reduces to 0.5h.

The microstructures of the samples sintered for 6h and 0.5h are further characterized by the scanning electron microscope. As shown by the backscattered electron (BSE) image in Fig. 4-4a, the sample sintered for 6h mainly contains three distinguishable regions, that is, the white, grey and dark area, based on the image contrast. Compared with the secondary electron (SE) image in Fig. 4-4b, some dark regions might result from not only the compositional contrast but also the pore or swell structures. Point analyses, as labelled by the numbers in Fig. 4-4a, are conducted on each region and the corresponding results are listed in Tab. 4-1.

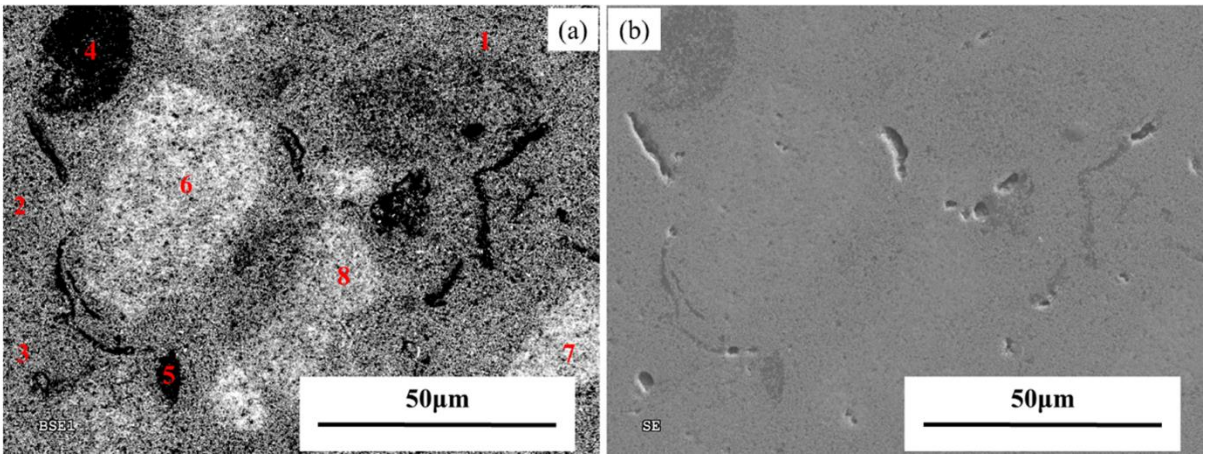

Fig. 4-4 (a) Backscattered electron (BSE) image and (b) secondary electron (SE) image of samples with composition of ZrO_2: Amorphous phase-1= 60: 40 sintered at 850°C for 6h.

Tab. 4-1 Atomic percentage of elements in different regions of the sample with composition of ZrO_2: Amorphous phase-1= 60: 40 sintered at 850°C for 6h.

	Spectrum	O	Na	Si	K	Ca	Zr	Na/Si	K/Si	Ca/Si
Grey region	Spectrum 1	66.43	0.19	13.00	0.68	0.45	19.25	0.01	0.05	0.03
	Spectrum 2	70.72	0.26	15.83	0.99	0.39	11.82	0.02	0.06	0.02
	Spectrum 3	67.38	0.38	16.69	0.98	0.50	14.07	0.02	0.06	0.03
	Average	68.18	0.28	15.17	0.88	0.45	15.04	0.02	0.06	0.03
Dark region	Spectrum 4	67.23	0.37	25.14	1.37	0.74	5.15	0.01	0.05	0.03
	Spectrum 5	66.31	0.28	25.67	1.16	0.49	6.08	0.01	0.05	0.02
	Average	66.77	0.33	25.41	1.27	0.62	5.62	0.01	0.05	0.02
White region	Spectrum 6	66.51	0.24	8.98	0.48	0.40	23.39	0.03	0.05	0.05
	Spectrum 7	65.56	0.17	10.28	0.57	0.41	23.01	0.02	0.06	0.04
	Spectrum 8	65.65	0.23	11.22	0.64	0.42	21.85	0.02	0.06	0.04
	Average	65.90	0.21	10.16	0.56	0.41	22.75	0.02	0.06	0.04

Except the pore or swell structures, the dark areas are rich in Si based on point analyses in Tab. 4-1. The Na/Si, K/Si and Ca/Si in the raw Amorphous phase-1 are 0.02, 0.06 and 0.03, respectively. However, these ratios in the dark region shown in Fig. 4-4 are slightly different from those in the raw Amorphous phase-1. We further checked this dark area at higher magnification and found some white particles on the dark surface as shown in Fig. 4-5. The point analyses in Tab. 4-2 illustrate the chemical composition of the dark area can be SiO_2 and contents of Na, K and Ca are rare. The white particles on the surface is rich in Zr and Si based on point analyses, which should be the ZrO_2 particles covered by the amorphous phase during sintering. More importantly, the Na/Si, K/Si and Ca/Si ratio in this particle are higher than

those in raw Amorphous phase-1. These results indicate the Amorphous phase-1 phase has separated into two different phases during sintering. One phase is rich in Na, K and Ca, while the other is deficient. This phenomenon is the characteristic of multi-components amorphous phase devitrification and in line with that Jean J. found in C7740 glass.[23] Combining the EDS results and XRD patterns, the dark regions shown in Fig. 4-4 should be related to the cristobalite phase.

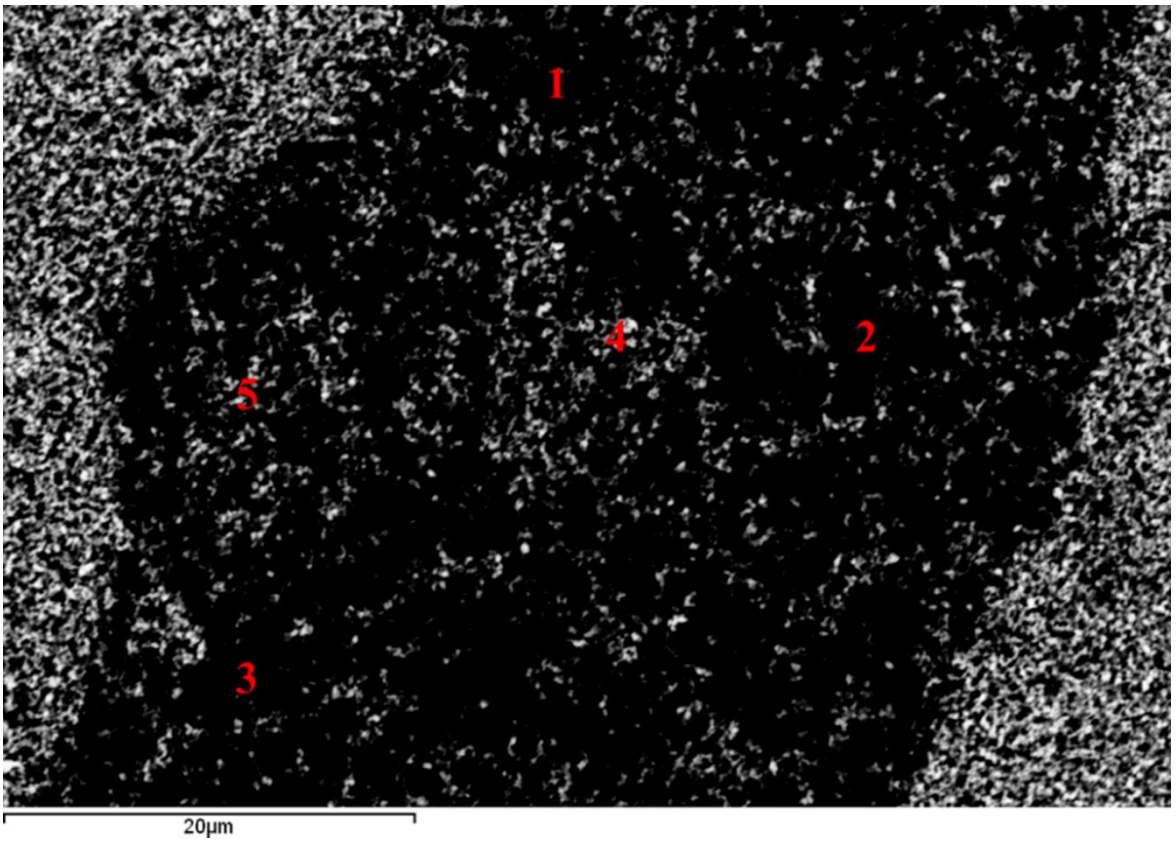

Fig. 4-5 Backscattered electron (BSE) image of the dark region in the sample with composition of ZrO_2: Amorphous phase-1= 60: 40 sintered at 850°C for 6h.

Tab. 4-2 Atomic percentage of elements in the dark region of the sample with composition of ZrO_2: Amorphous phase-1= 60: 40 sintered at 850°C for 6h.

Spectrum	O	Na	Si	K	Ca	Zr	Na/Si	K/Si	Ca/Si
Spectrum 1	68.56	0.15	25.11	0.36	0.29	5.52	0.01	0.01	0.01

Spectrum 2	68.11	0.10	26.04	0.30	0.23	5.22	0.00	0.01	0.01
Spectrum 3	68.36	0.08	28.07	0.11	0.15	3.23	0.00	0.00	0.01
Average	68.34	0.11	26.41	0.26	0.23	4.66	0.00	0.01	0.01
Spectrum 4	69.15	0.55	12.72	1.84	0.64	15.09	0.04	0.14	0.05
Spectrum 5	70.64	0.42	16.45	1.39	0.74	10.36	0.03	0.08	0.05

According to the point analyses in Tab. 4-1, the grey and white regions are rich in both Si and Zr. The Na/Si, K/Si and Ca/Si values in both regions are equivalent to those in the raw Amorphous phase-1, which implies the Si should be in the form of the amorphous phase. Referring to the XRD pattern, the Zr should exist as the ZrO_2 phase. The typical microstructure is shown in Fig. 4-6, where small particles showing the white colour are randomly embedded in the grey matrix. The two regions should be the ZrO_2 particles covered by the molten Amorphous phase-1 and some parts of them agglomerates, forming the white regions.

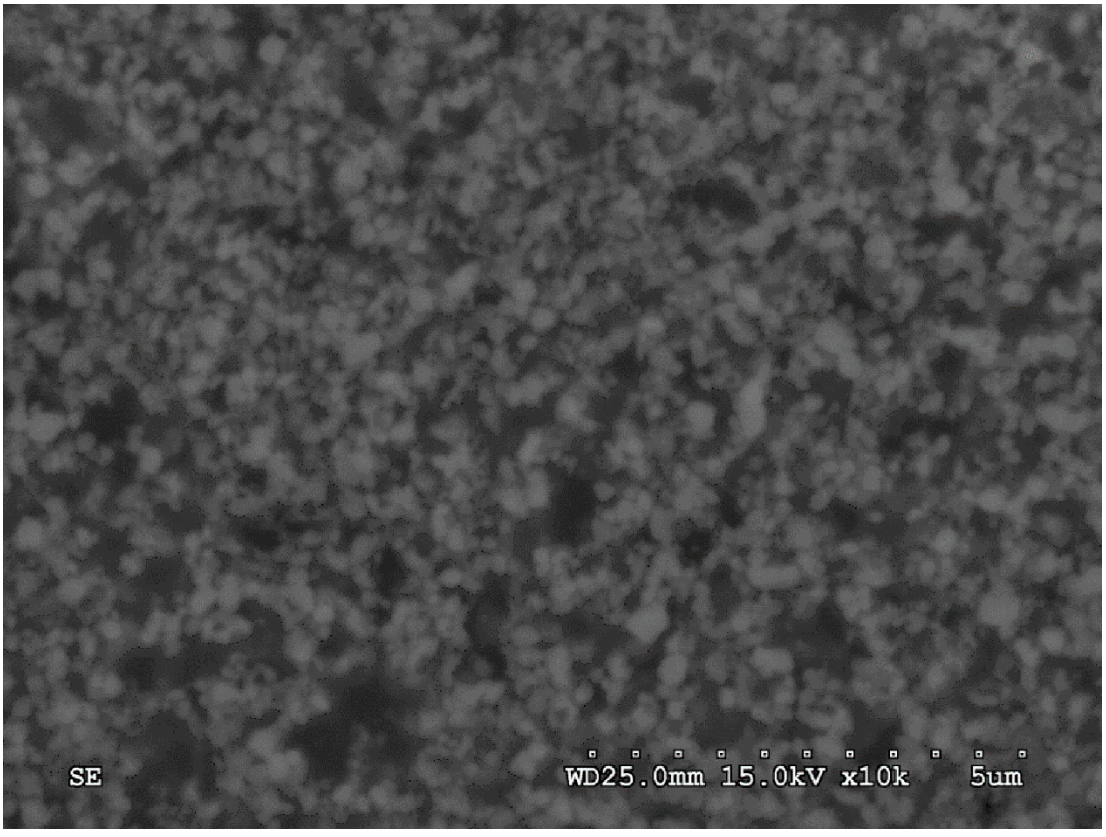

Fig. 4-6 Microstructure of the Si-Zr-rich region in the sample with composition of ZrO_2: Amorphous phase-1= 60: 40 sintered at 850^oC for 6h.

For comparison, the microstructure of the sample sintered for 0.5h is also characterized (Fig. 4-7). It is evident that compared with the sample sintered for 6h, this sample only contains a few regions with the black area. With further investigating the SE image in Fig. 4-7b, it can be deduced that the black dots in the BSE image are related to the pore or swell structures. In other words, the black dots in Fig. 4-7a do not belong to the pure SiO_2, which is associated with the cristobalite phase, and this result is in line with the XRD result in Fig. 4-3.

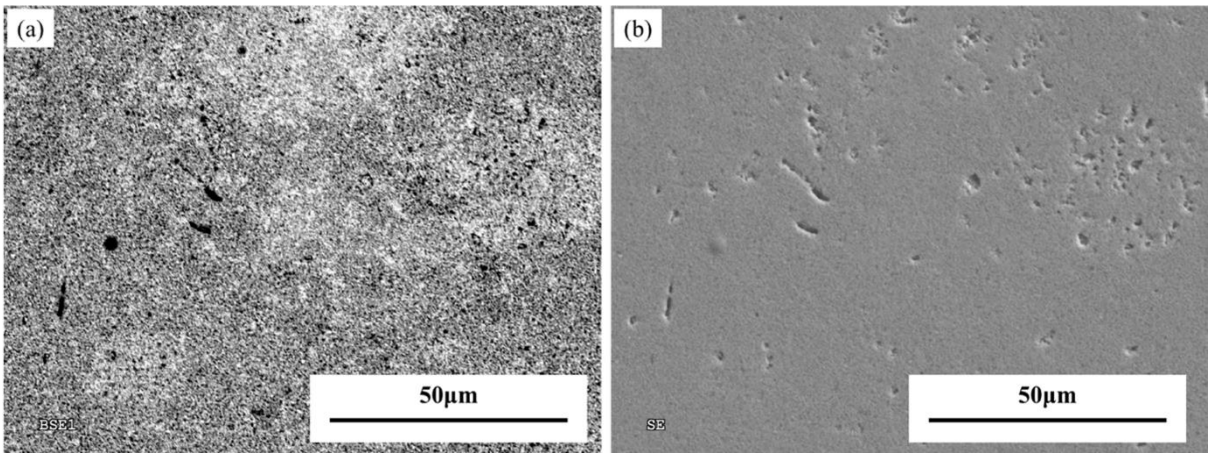

Fig. 4-7 (a) Backscattered electron image (BSE) and (b) secondary electron (SE) image of samples with composition of ZrO_2: Amorphous phase-1= 60: 40 sintered at 850^oC for 0.5h.

Fig. 4-8 illustrates the coefficient of thermal expansion (CTE) of the sample sintered at 850^oC for different soaking periods. For the samples with sintering time longer than 3h, their slopes of CTE experience a sudden increase between 100^oC and 200^oC, which is the typical temperature range for the displacive transformation of the cristobalite phase.[24] When decreasing the sintering time to less than 1 h, the slope change is constrained. With further reducing the soaking period to 0.5h, the abrupt change of the slope has disappeared, which is in line with the XRD results in Fig. 4-3, as well as the microstructure analyses. In addition, this value matches with that of alumina board and chip, which is an important factor for LTCC

applications.

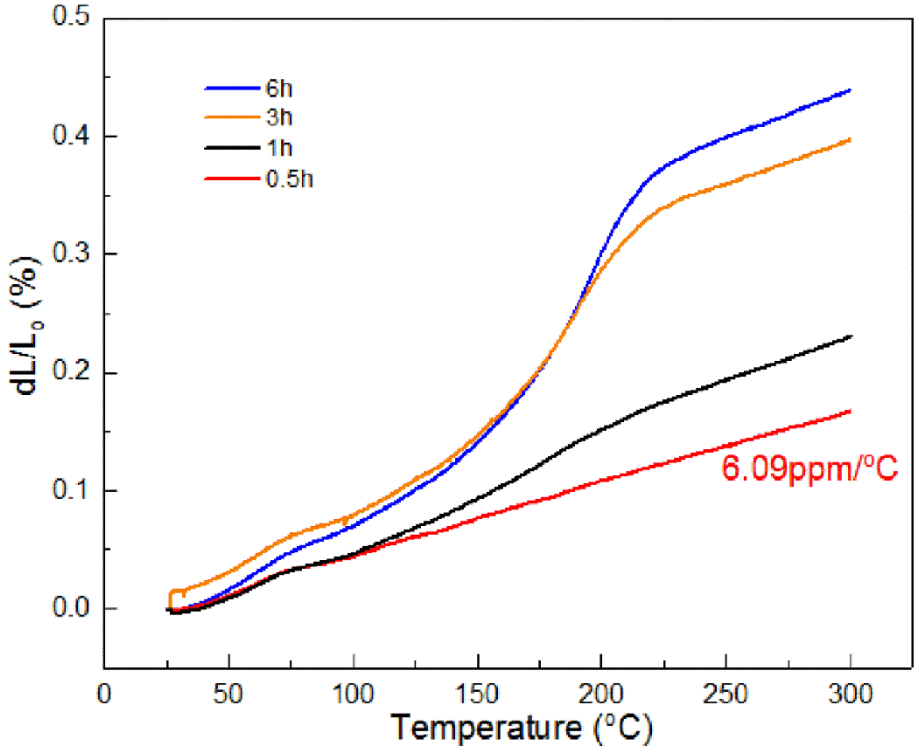

Fig. 4-8 Coefficient of thermal expansion of the samples with composition of ZrO_2: Amorphous phase-1= 60: 40 sintered at 850°C for various soaking period.

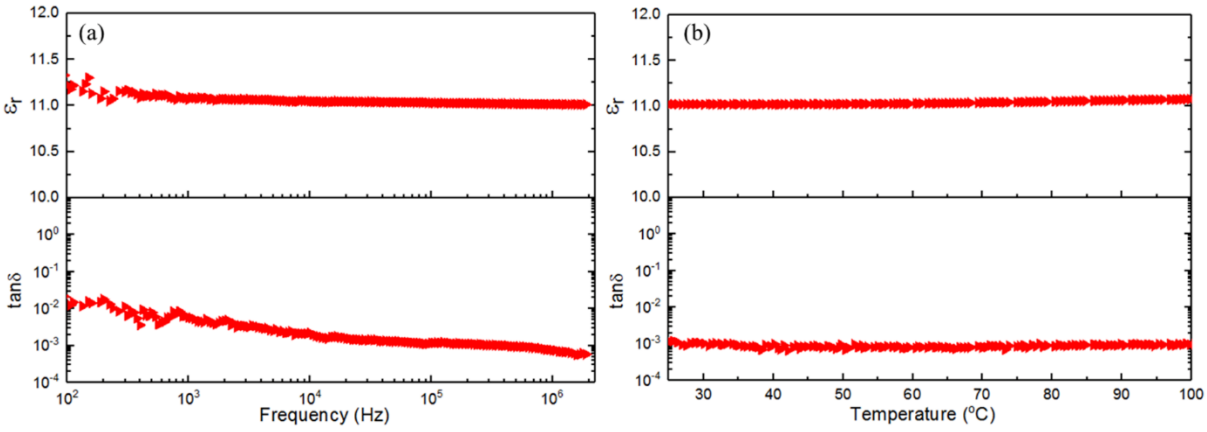

Fig. 4-9 (a) Frequency and (b) temperature dependence of dielectric properties of samples with composition of ZrO_2: Amorphous phase-1= 60: 40 sintered at 850°C for 0.5h.

The dielectric properties of the sample sintered for 0.5h are very stable and show low dependence on either frequency or temperature. Fig. 4-9a shows dielectric properties of samples under room temperature from 100Hz to 2MHz. The dielectric constant is quite stable. showing low dependence of frequency, and the loss is small. Thus, the samples could be used in a wide frequency range. Additionally, the temperature-dependent dielectric properties are also characterized (Fig. 4-9b). In the typical temperature range for device operation (25^{o}C-100^{o}C), the variation of dielectric constant (@1MHz) is as low as 0.5%. Besides, it also shows the resistivity of $2.3\times10^{12}\Omega\cdot$cm under 100V (DC), which meets the requirement for LTCC applications.

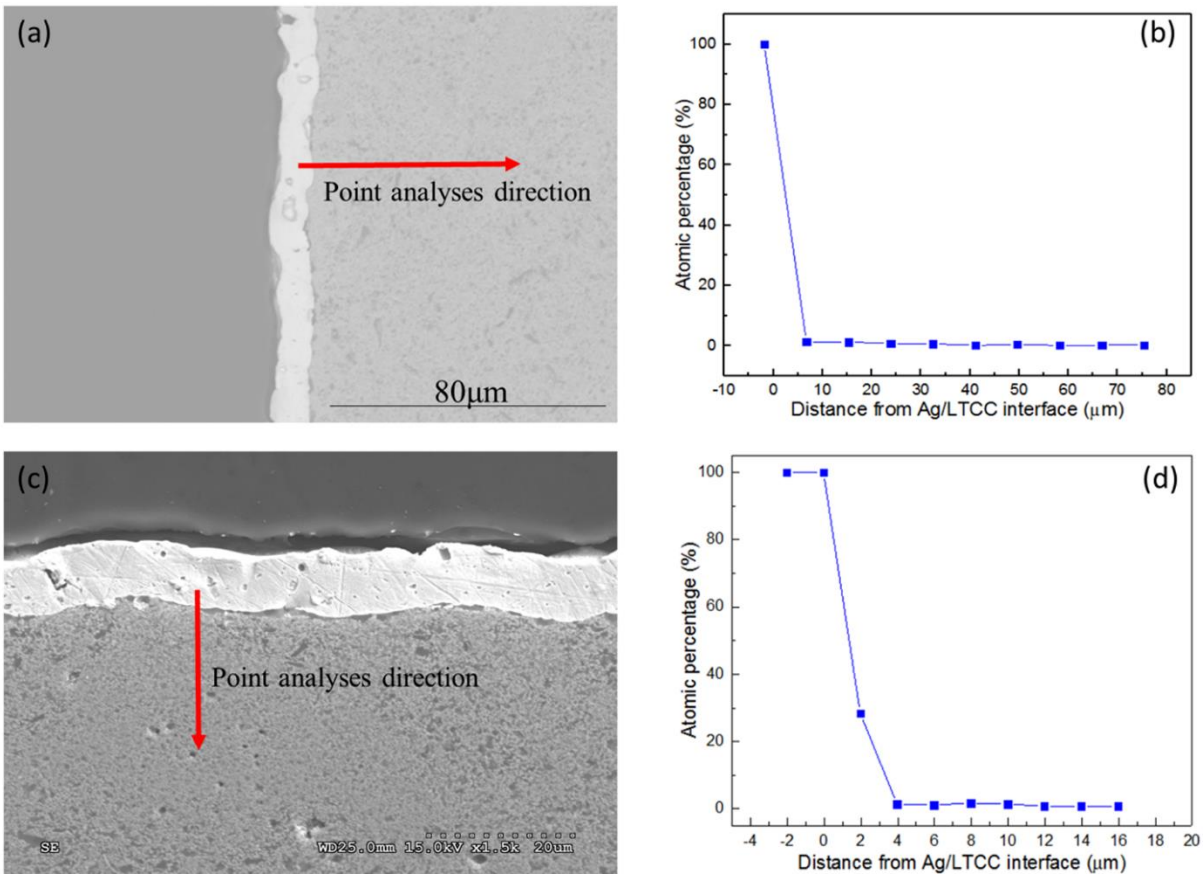

Fig. 4-10 (a) and (c) SEM image of the cross section of the LTCC/Ag interface; (b) and (d) Atomic percentage of Ag at the interface.

The compatibility of the developed sample with the silver electrode is further checked in Fig. 4-10, although it can be sintered at 850^{o}C which is below the melting point of co-fired Ag

electrode. It can be seen that the silver electrode is tightly integrated with ceramic (ZrO_2: Amorphous phase-1= 60: 40) in Fig. 4-10a, without any obvious cracking or delamination. A series of the point analyses are conducted along the Ag/LTCC sample interface and the Ag profile decreases dramatically as crossing the interface (Fig. 4-10b). Fig. 4-10c presents a much closer image of the interface. The atomic percentage of Ag also drops sharply at the interface in Fig. 4-10d, which means the Ag did not diffuse into the ceramics during sintering. It is worthy pointing out that the measurement results will be disturbed by the Ag electrode when the test point is too close to the interface, such as the third point in Fig. 4-10d, because of the EDS interaction volume.[25]

So far, the composite based on ZrO_2/Amorphous phase-1 composite has been developed. It shows relative permittivity of ~11 at 1MHz and comprehensive performance for application in design of high frequency circuits. In the next section, we used pure fused SiO_2 and Amorphous phase-1 to develop the composite with low dielectric constant for rapid signal transition.

4.2 Pure fused SiO_2 for composite with low dielectric constant

4.2.1 Background

Generally, LTCC materials with relative permittivity in the range from 4 to 12 are used for substrate layers while those with higher dielectric constant are mainly used as capacitor layers or resonating structures.[17] In terms of the application in substrates, those with lower permittivity are more favour of rapid signal transition since the signal propagation delay is proportional to the square root of relative permittivity of the ceramic.[26] By far, the reported LTCC materials focus on the composites comprising the ceramic and glass phase.[27, 28] For these composites, the dielectric constants can be empirically described by the dielectric constant and volume fraction of each phase, that is $\log \varepsilon_r = \Sigma v_i \log \varepsilon_i$, where ε_r represents for the dielectric constant of the composite, the v_i is volume fraction and ε_i is relative permittivity of each phase, respectively.[22]

Due to the complex composition of glass, it is relatively easier to modulate the dielectric constant of the composite by selecting appropriate ceramic materials. In previous work, we have developed amorphous phase/ceramic composite with permittivity of 7 and 11, using Al_2O_3 and ZrO_2 as the ceramic material, respectively. For the sake of rapid signal transition, LTCC materials with smaller permittivity is highly demanded. Therefore, silica can be introduced as the ceramic materials because of its low dielectric constant. Silica also involves many polymorphs, such as quartz, cristobalite and fused silica. Among them, cristobalite exhibits displacive transformation at ~200ºC [23, 29, 30] and the high coefficient of thermal expansion of 50×10^{-6}/ºC,[31, 32] which leads to unwanted thermal stress and mechanical damage. As a result, the presence of cristobalite phase should be avoided during sintering.

In this section, we used sol-gel derived Amorphous phase-1 and pure fused SiO_2 to develop a composite with dielectric constant as low as ~5 for the substrates used in rapid signal transition. Also, the developed LTCC materials had resistivity above $10^{12}\Omega\cdot$cm as a good insulator, good compatibility with Ag electrode and suitable coefficient of thermal expansion with Si chips. We began with the composition of Amorphous phase-1: pure fused SiO_2=50.19: 49.81(mass ratio), which replaced Al_2O_3 in the developed Amorphous phase-1/Al_2O_3 composite (in Chapter 3) with the same mass of pure fused SiO_2. The compositions were optimized according to target performance. The final developed composite possesses comprehensive performance and provides an alternative for industrial products.

4.2.2 Synthesis of amorphous phase/fused SiO_2/Al_2O_3 composite

Various amount of Amorphous phase-1 powder (obtained in Chapter 3), pure fused SiO_2 (99.5%, 325mesh, Sigma-Aldrich) and Al_2O_3 (99.9%, 135nm, US Research Nanomaterials, Inc.) were ball milled in ethanol for 15h. Then the dried powder mixtures were pressed into cylindrical compacts with the diameter of 13mm under the uniaxial pressure of 7MPa. The green samples were sintered from 800ºC to 900ºC for 6h with heating rate of 3ºC/min. To check the compatibility with silver electrode, the raw materials were granulated with 5wt% polyvinyl butyral (PVB) and then pressed into pellets under the uniaxial pressure of 7MPa. The

green sample coated with the silver paste was first heat-treated at 450ºC for 2h to burn out the binders then further heated at 850ºC for 6h and finally cooled down to room temperature naturally.

4.2.3 Compositions, structures and properties of amorphous phase/fused SiO_2/Al_2O_3 composite

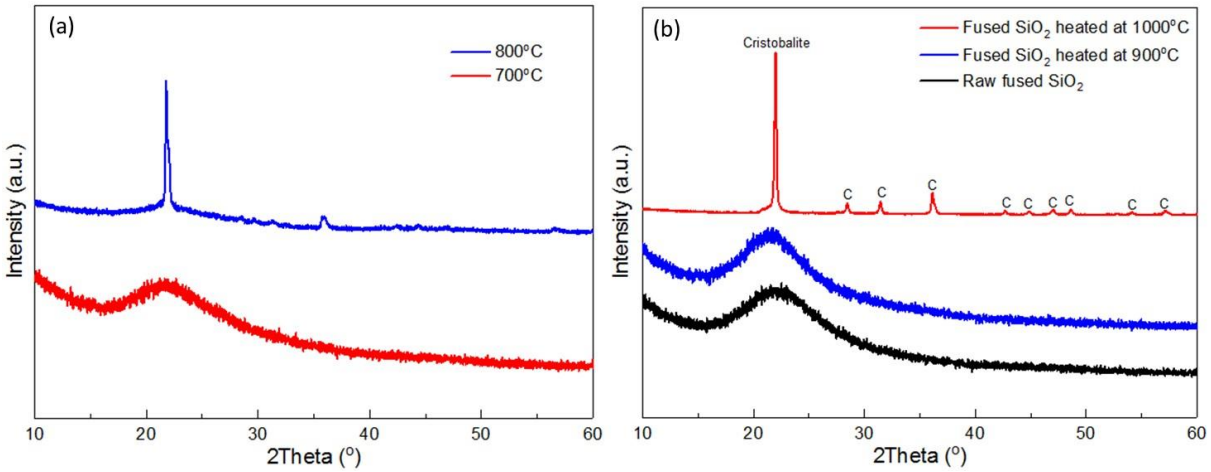

Fig. 4-11 (a) XRD patterns of Amorphous phase-1 powder heated from 700ºC to 800ºC. (b) XRD patterns of raw fused SiO_2 and that heated between 900ºC and 1000ºC.

Fig. 4-11 illustrates the XRD patterns of heat-treated Amorphous phase-1 powder and the pure fused SiO_2. For the Amorphous phase-1 (obtained in 3.2.1), as illustrated in Fig. 4-11a, it remains the amorphous structure when further heated at 700ºC for 2h. However, two crystal peaks appear when heated at 800ºC. Considering the composition of Amorphous phase-1, these peaks could be indexed to the cristobalite (SiO_2) phase (ICSD code: 77452). In terms of the pure fused SiO_2, it remains amorphous structure even sintered at 900ºC for 2h (Fig. 4-11b), but it dramatically gets crystallized when heated at 1000ºC. All the crystal peaks can be indexed to the tetragonal cristobalite (SiO_2) phase (ICSD code: 77452). As a result, it can be deduced that the Amorphous phase-1 is more inclined to get crystallized at lower temperature than the pure fused SiO_2.

With the composition of Amorphous phase-1: pure fused SiO_2=50.19: 49.81(mass ratio), the

sample shows the relative permittivity of ~5 (@1MHz) and dielectric loss well below 0.003 (@1MHz) in Fig. 4-12 when sintered at 800°C, 850°C and 900°C. Such good dielectric properties are quite favour of rapid signal transition in LTCC application. However, the XRD pattern of above sample sintered at 800°C in Fig. 4-13 shows the crystal structure which can be identified as the cristobalite phase. As abovementioned, the generated cristobalite phase is unfavourable to the application in LTCC due to its phase transformation and large CTE of ~50 $\times 10^{-6}$/°C, and therefore, another composition is required to suppress the crystallisation of the cristobalite phase.

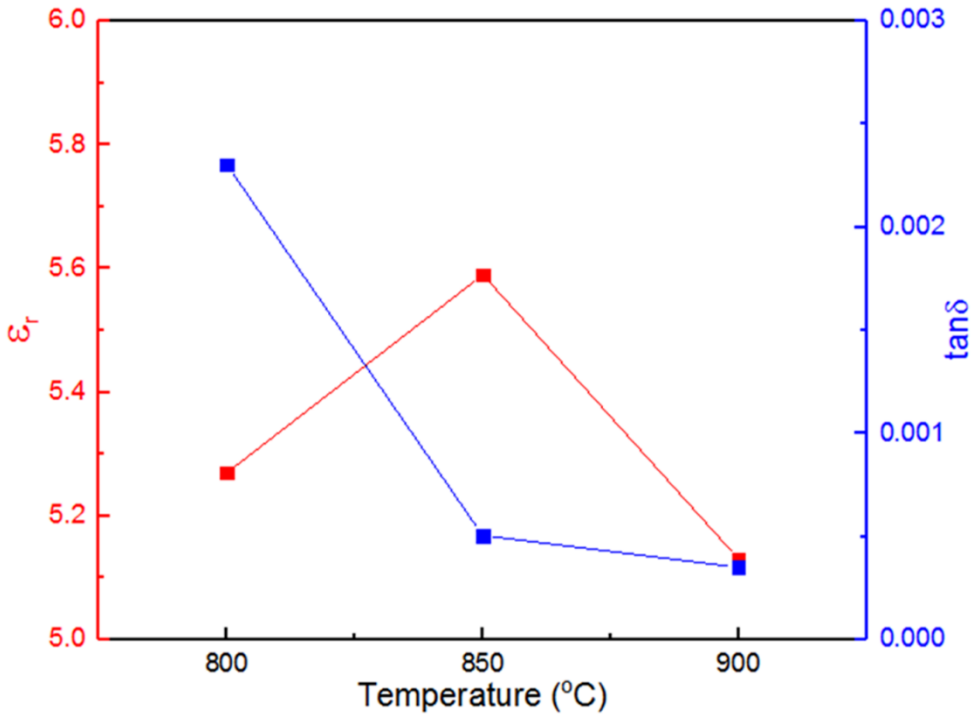

Fig. 4-12 Dielectric properties (@1MHz) of samples with the composition of Amorphous phase-1: pure fused SiO_2=50.19: 49.81and sintered from 800°C to 900°C.

It is reported that the aluminium-containing compounds can inhibit the formation of cristobalite phase.[33, 34] Therefore, various amount of Al_2O_3 is introduced into the sample with composition of Amorphous phase-1: pure fused SiO_2=50.19: 49.81. It can be seen in the Fig. 4-13 that peaks from the cristobalite phase remain in the sample with 1wt% addition of Al_2O_3. With 3wt% addition of the Al_2O_3, the grain size of the cristobalite phase should have been decreased since

the peak width is broadening. This implies the addition of Al_2O_3 could restrain the crystal growth of cristobalite phase. While 5wt% Al_2O_3 is introduced, the shape peaks associated with the cristobalite phase are barely obtained, indicating this unfavourable phase has been fully suppressed. Furthermore, some tiny peaks which can be indexed as the hexagonal corundum (Al_2O_3) phase (ICSD code: 52647) and hexagonal quartz (SiO_2) phase (ICSD code: 155243) appear.

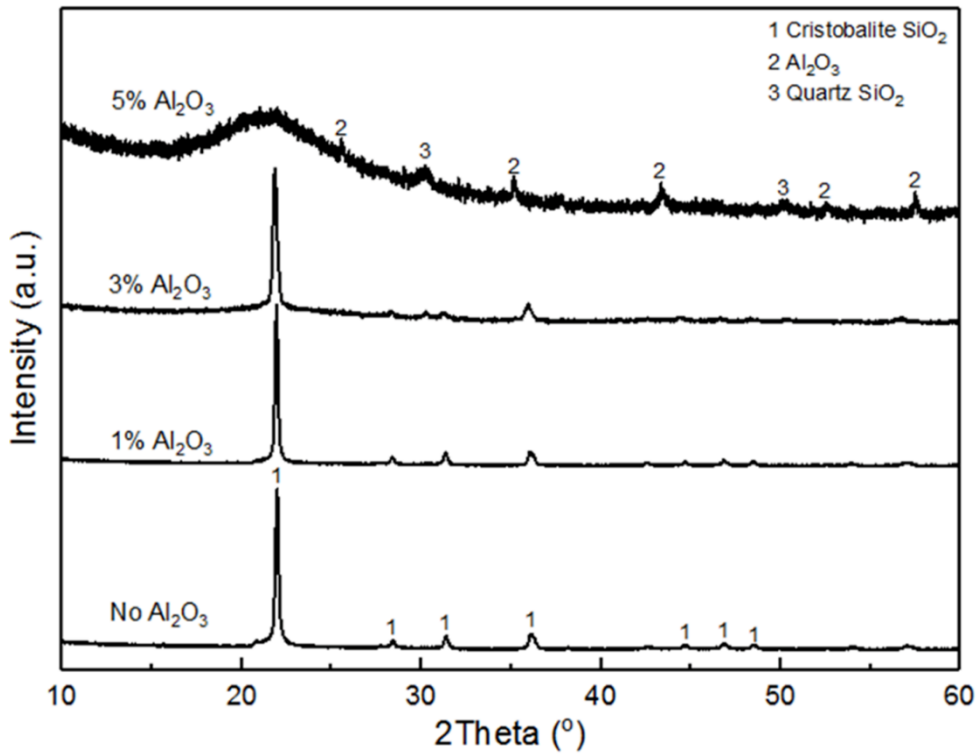

Fig. 4-13 XRD patterns of samples (Amorphous phase-1: pure fused SiO_2=50.19: 49.81) with 0~5wt% addition of Al_2O_3 sintered at 800°C.

The sintering temperature of LTCC materials is generally required to be above 800°C to fully get rid of the organic group involved in the industrial tape-casting process.[26] However, in Fig. 4-14a, it can be found that with increasing the sintering temperature to 850°C, the cristobalite phase reappears, which means this developed composition optimized by the additional Al_2O_3 can only be sintered at 800°C. This phenomenon is in accordance with Jean's result that the formation of cristobalite phase exhibits a characteristic incubation period that decreases with the temperature increasing.[23] As illustrated in Fig. 4-11, the undesired cristobalite phase should

come from the Amorphous phase-1 phase since it will get crystallized at lower temperature compared with the pure fused SiO_2. In order to synthesize the sample without cristobalite phase at higher temperature, the proportion of Amorphous phase-1 in the composite is modulated. As illustrated in Fig. 4-14b, when sintered at 850°C, the increase of the Amorphous phase-1 ratio in the raw materials results in more cristobalite phase since its peak intensities are increasing. In contrast, when the Amorphous phase-1/fused SiO_2 ratio decreases to 45/55 or 40/60, the undesired cristobalite phase is fully inhibited. This is consent with the above assumption that the undesired cristobalite phase is mainly originated from the Amorphous phase-1 phase in raw material.

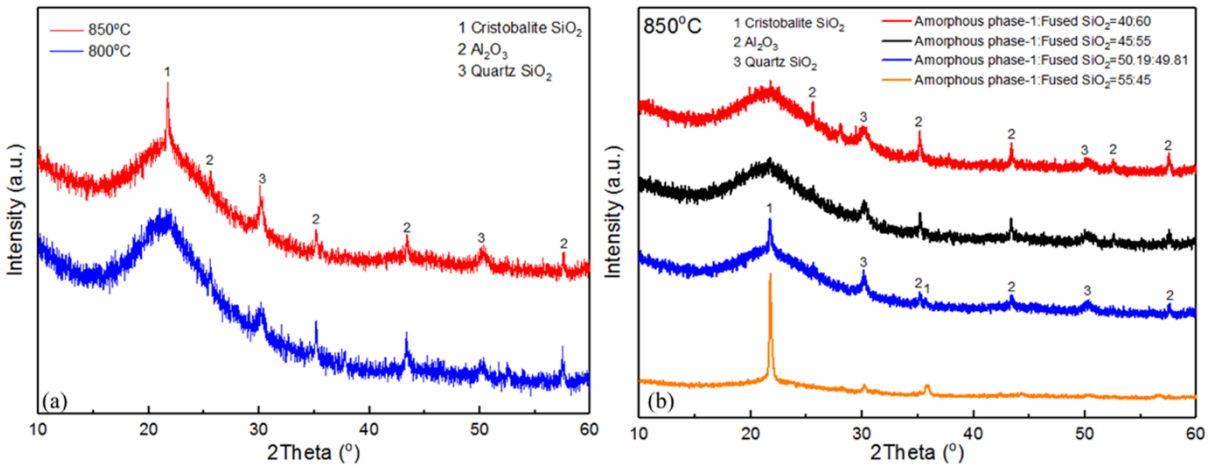

Fig. 4-14 (a) XRD patterns of samples with composition of Amorphous phase-1: fused SiO_2=50.19: 49.81and 5wt% Al_2O_3 sintered between 800°C and 850°C; (b) XRD patterns of samples with various Amorphous phase-1/fused SiO_2 ratio and 5wt% Al_2O_3 sintered at 850°C.

The SEM image in Fig. 4-15 shows the microstructures of the samples with various Amorphous phase-1/fused SiO_2 ratio and 5wt% Al_2O_3. It can be seen that for the samples with Amorphous phase-1 ratio higher than 50.19%, they show well densified microstructure (Fig. 4-15e-h). The sample with Amorphous phase-1: fused SiO_2=45:55 in Fig. 4-15c and Fig. 4-15d also shows the relatively densified structure with some irregular pores. In contrast, the one with Amorphous phase-1: fused SiO_2 =40: 60 in Fig. 4-15a and Fig. 4-15b shows a less dense microstructure, where some interconnected pores with larger size are presented. This is because

that the amount of Amorphous phase-1 is not enough to densify the structure compared with those involving more amorphous phase.

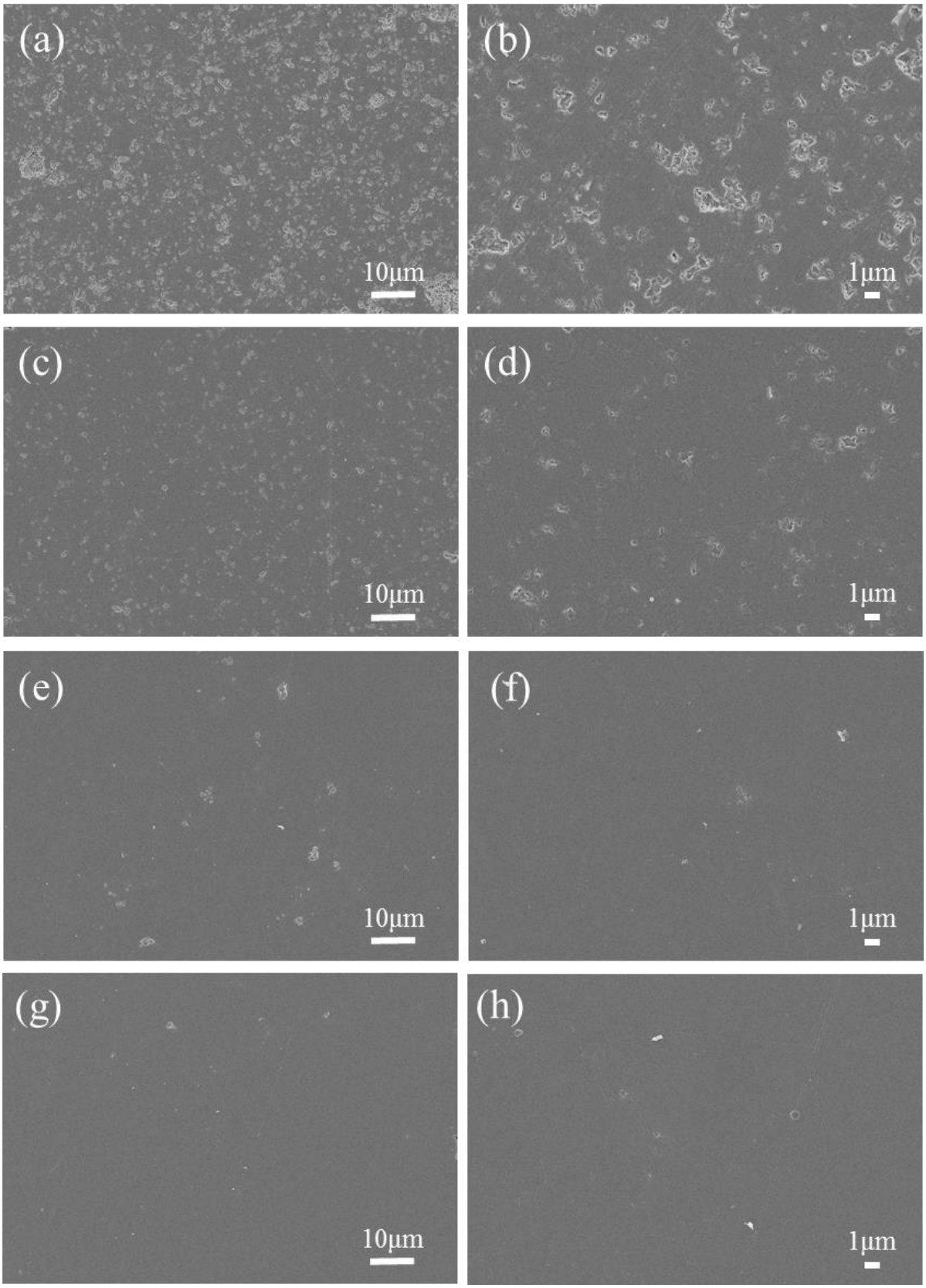

Fig. 4-15 SEM images of samples with various Amorphous phase-1/fused SiO_2 ratio and 5wt% Al_2O_3: (a) and (b) Amorphous phase-1: fused SiO_2=40:60; (c) and (d) Amorphous phase-1: fused SiO_2=45:55; (e) and (f) Amorphous phase-1: fused SiO_2=50.19:49.81; (g) and (h) Amorphous phase-1: fused SiO_2=55:45.

The electrical properties of samples with respect to the Amorphous phase-1/fused SiO_2 ratio and 5wt% Al_2O_3 sintered at 850°C are shown in Fig. 4-16. As illustrated in Fig. 4-16a, the dielectric constant of the samples are ~5 and show slight reduction with decreasing the proportion of Amorphous phase-1 in raw materials. This result is quite consistent with that deduced from the empirical formula shown in 4.2.1 since the dielectric constant of the Amorphous phase-1 is higher than that of pure fused SiO_2. The shrinkage and resistivity have the positive correlation with the ratio of Amorphous phase-1/fused SiO_2. When the percentage of Amorphous phase-1 is higher than 45%, the samples show resistivity above $10^{12}\Omega\cdot cm$. While the Amorphous phase-1/SiO_2 ratio decreases to 40:60, the resistivity drops below $10^{12}\Omega\cdot cm$ in Fig. 4-16b. This low resistivity can relate to its porous microstructure as shown in Fig. 4-15. Taking all benchmarks into consideration, the sample with composition of (45wt% Amorphous phase-1 - 55wt% fused SiO_2)-5wt% Al_2O_3 (i.e. 42.86wt% Amorphous phase-1-52.38wt% fused SiO_2- 4.76wt% Al_2O_3) shows the best performance. In detail, it shows relative permittivity of 4.89 @1MHz, dielectric loss of 0.0025 @1MHz, resistivity of $2.52\times10^{12}\Omega\cdot cm$ under 100V DC and shrinkage of 21% in XY plane when sintered at 850°C.

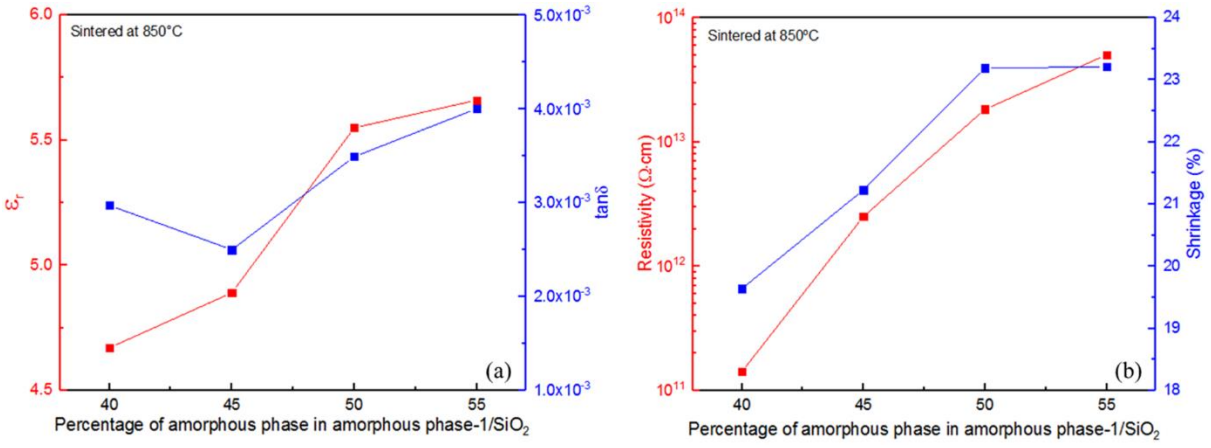

Fig. 4-16 (a) Dielectric properties and (b) resistivities and XY shrinkages of samples with

various Amorphous phase-1/fused SiO_2 ratio and 5wt% Al_2O_3 sintered at 850°C.

Additionally, the dielectric properties of the sample with the best performance also show low dependence of either frequency or temperature in Fig. 4-17, which is good for real application. The dielectric properties under room temperature are characterized in the frequency range from 100Hz to 2MHz in Fig. 4-17a. Both the relative permittivity and dielectric loss are quite stable throughout the range, which indicates it is an excellent insulator and can be used in a wide range. In addition, its dependence on temperature ranging from room temperature to 100°C is illustrated in Fig. 4-17b. The variation of dielectric constant (@1MHz) is as low as 0.98%.

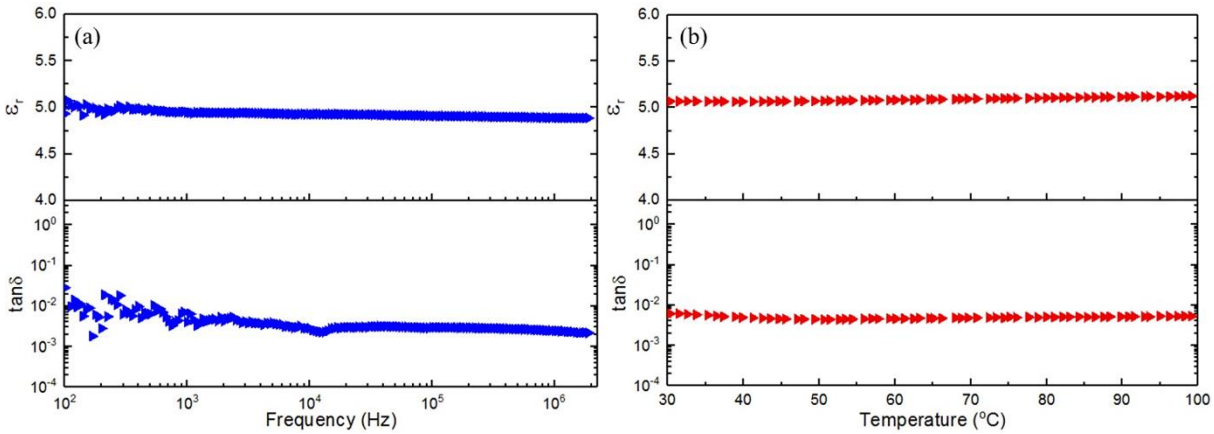

Fig. 4-17 (a) The dielectric properties (at room temperature) of the samples with composition of 42.86wt% Amorphous phase-1- 52.38wt% pure fused SiO_2- 4.76wt% Al_2O_3 sintered at 850°C; (b) The temperature dependence of dielectric properties (@1MHz) from 30°C to 100°C.

Although the developed materials can be sintered at 850°C, which is below the melting point of silver electrode, it must be compatible with electrode since any reactions between them can degrade the device performance. Fig. 4-18 illustrates the cross section of the sample co-fired with Ag electrode. It can be seen that silver electrode is tightly integrated with ceramic without any obvious cracking or delamination. Also, a series of point analyses were done in the direction perpendicular to the interface to characterize the diffusion of silver. As shown in Fig. 4-18, the Ag profile decreases dramatically at the interface, which means the Ag should not diffuse into the ceramics during sintering. It is worth to point out that the accurate Ag profile might be shaper in consideration of smearing effect caused by soft silver electrode during

polishing.

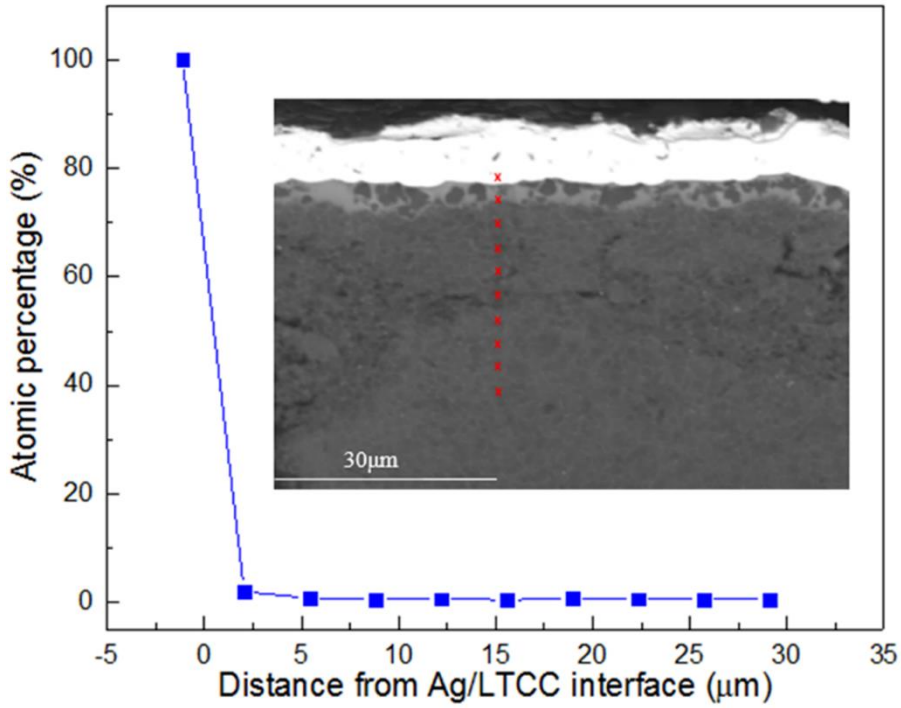

Fig. 4-18 Backscattered image of the cross section of sintered sample and the atomic percentage of Ag at the LTCC/Ag electrode interface.

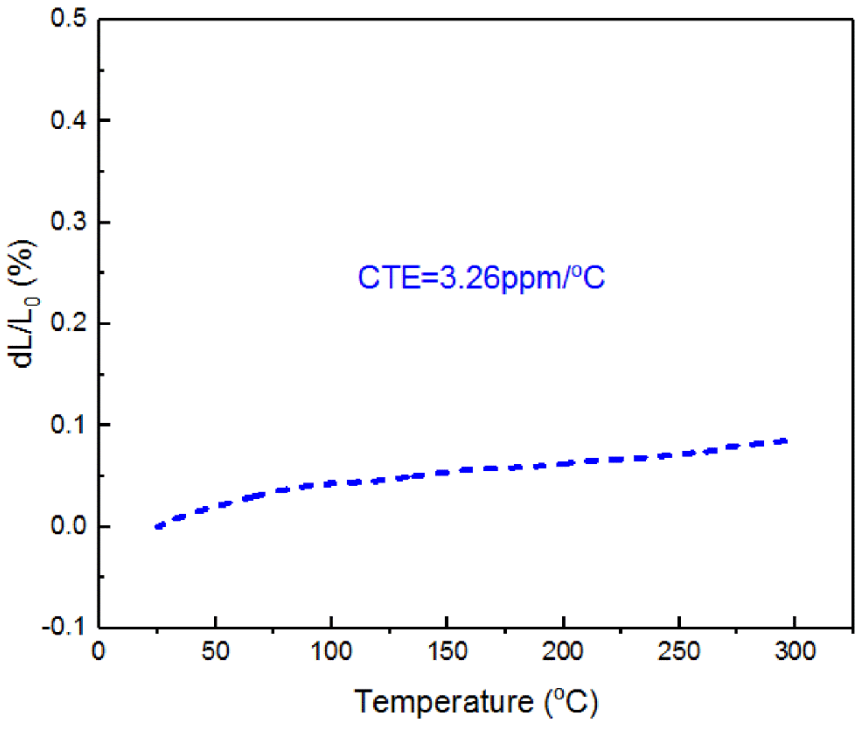

Fig. 4-19 Coefficient of thermal expansion of the samples with composition of 42.86wt% Amorphous phase-1- 52.38wt% pure fused SiO_2- 4.76wt% Al_2O_3 sintered at 850°C.

In real application, the coefficient of thermal expansion (CTE) is an important parameter for LTCC modules because the difference of CTE between the top-mounted Si chip and LTCC module will generate the misfit strain, leading to electrical contact failure or substrate crack. The CTE of the composites also depend on that of each constituent and their volume fractions. The CTE of the developed composite is shown in Fig. 4-19 in the temperature ranging from room temperature to 300°C. The abrupt slope change in 100°C~200°C, which is the typical displacive transition of the cristobalite phase,[24] is absent here. This agrees with the XRD results in Fig. 4-14b that the cristobalite phase is fully suppressed. The result shows the sample sintered at 850°C has the average CTE of ~3.26ppm/°C which is compatible and suitable with the Si chip.

4.3 Conclusion

In this chapter, we have developed two composites with relative permittivity of 11 and 5 based on amorphous phase/ZrO_2 and amorphous phase/fused SiO_2/Al_2O_3 composite, respectively.

Firstly, we developed an Amorphous phase-1/ZrO_2 composite where the Amorphous phase-1 phase is synthesized by the sol-gel method instead of common melt-quench method. The influences of ZrO_2 amount, as well as soaking period, on the crystallization and properties have also been investigated based on XRD, SEM and thermal expansion characterization. The ZrO_2 shows evident influence on the phases presented in the sintered sample and the electrical properties. In addition, the undesired cristobalite phase can be successfully inhibited by reducing the soaking period. Finally, a new composite with composition of ZrO_2: Amorphous phase-1=60: 40 (mass ratio) has been developed. It shows relative permittivity of ~11 (@1MHz), dielectric loss ~0.0008 (@1MHz), resistivity of $2.3\times10^{12}\Omega\cdot$cm, shrinkage in the XY-plane of 15.47% and CTE of 6.09ppm/°C when sintered at 850°C for 30min. Besides these, it is compatible with silver electrode and the dielectric properties show low dependence on either frequency or temperature. This good performance is promising for application in design

of high frequency circuits.

In addition, an Amorphous phase-1/fused SiO_2/Al_2O_3 composite with low dielectric constant has been developed for LTCC application. Although the composition based on Amorphous phase-1 and pure fused SiO_2 shows good dielectric properties, the XRD results illustrate the sintered sample contains undesired cristobalite phase. Addition of 5wt% Al_2O_3 in this case is effective to suppress the formation of cristobalite phase but the sintering temperature is limited at 800^oC, which is not good for fully removing of organic group involved in the industrial tape-casting process. Finally the ratio of the Amorphous phase-1/fused SiO_2 is adjusted to modulate the sintering temperature and restrain the formation of cristobalite phase. On balance, the sample with composition of 42.86wt% Amorphous phase-1- 52.38wt% fused SiO_2- 4.76wt% Al_2O_3 sintered at 850^oC exhibits the relative permittivity of ~5, dielectric loss below 0.003 (@1MHz), resistivity above $10^{12}\Omega\cdot cm$ and coefficient of thermal expansion of 3.26ppm/^oC from room temperature to 300^oC. Besides these, it is also compatible with silver electrode during sintering based on the EDS characterization. With such good and comprehensive performances, it is very promising for rapid signal transition.

At this point, we have developed four amorphous phase-based LTCC materials with relative permittivity from 4 to 12. All of them show comprehensive performance for commercial application. In the next chapter, we will try to develop a novel composite without any amorphous phase for LTCC application.

Reference

1. Ma, M.; Khan, H.; Shan, W.; Wang, Y.; Ou, J. Z.; Liu, Z.; Kalantar-zadeh, K.; Li, Y., A novel wireless gas sensor based on LTCC technology. *Sensors and Actuators B: Chemical* **2017,** *239*, 711-717.

2. Akanksha Bhutani, Heiko Gulan, Benjamin Goettel, Christoph Heine, Torsten Thelemann, Mario Pauli, Thomas Zwick, 122GHz aperture coupled stacked patch microstrip antenna in LTCC technology. In *10th European Conference on Antennas and Propagation* IEEE: Davos, Switzerland, 2016.

3. Rajesh, S.; Jantunen, H.; Letz, M.; Pichler-Willhelm, S., Low Temperature Sintering and Dielectric Properties of Alumina-Filled Glass Composites for LTCC Applications. *International Journal of Applied Ceramic Technology* **2012,** *9* (1), 52-59.

4. Luo, X.; Ren, L.; Xie, W.; Qian, L.; Wang, Y.; Sun, Q.; Zhou, H., Microstructure, sintering and properties of $CaO–Al_2O_3–B_2O_3–SiO_2$ glass/Al_2O_3 composites with different CaO contents. *Journal of Materials Science: Materials in Electronics* **2016,** *27* (5), 5446-5451.

5. Hong, K. P.; Choi, I. J.; Jung, J. W.; Choi, H. R.; Cho, Y. S.; Kwak, J.; Kang, D. H., Densification, Crystallization, and Dielectric Properties of AlN, BN and Si_3N_4 Filler-Containing LTCC Materials. *International Journal of Applied Ceramic Technology* **2013,** *10*, E25-E32.

6. Seo, Y. J.; Jung, J. H.; Cho, Y. S.; Kim, J. C.; Kang, N. K., Influences of Particle Size of Alumina Filler in an LTCC System. *Journal of the American Ceramic Society* **2007,** *90* (2), 649-652.

7. Gangwar, J.; Gupta, B. K.; Tripathi, S. K.; Srivastava, A. K., Phase dependent thermal and spectroscopic responses of Al_2O_3 nanostructures with different morphogenesis. *Nanoscale* **2015,** *7* (32), 13313-44.

8. Vanderbilt, D.; Zhao, X.; Ceresoli, D., Structural and dielectric properties of crystalline and amorphous ZrO_2. *Thin Solid Films* **2005,** *486* (1-2), 125-128.

9. A. Feinberg and C. H. Perry, Structural disorder and phase transutions in ZrO_2-Y_2O_3 system. *J. Phys. Chem. Solids* **1981,** *42*, 513-518.

10. M. T. Lanagan, J. K. Yamamoto, A. Bhalla, S. G. Sankar, The dielectric properties of ytitria-stabilized zirconia. *Materials Letters* **1989,** *7*, 437-440.

11. D. P. Thompson, A. M. Dickins, J. S. Thorp, The dielectric properties of zirconia. *Journal of Materials Science* **1992,** *27*, 2267-2271.

12. Li, B.; Duan, D.; Long, Q., Influences of ZrO_2 on microstructures and properties of $Li_2O–Al_2O_3–SiO_2$ glass–ceramics for LTCC applications. *Journal of Materials Science: Materials in Electronics* **2015,** *27* (1), 134-139.

13. Liu, J. Z.; Yao, Z. H.; Xu, N. X.; Zhang, Q. L.; Yang, H., Densification Behavior and Dielectric Properties of $CaO-B_2O_3-SiO_2$ System Glass-Ceramics Containing ZrO_2. *Key Engineering Materials* **2016,** *697*, 253-256.

14. Hsiang, H.-I.; Yung, S.-W.; Wang, C.-C., Crystallization, densification and dielectric properties of $CaO–MgO–Al_2O_3–SiO_2$ glass with ZrO_2 as nucleating agent. *Materials Research Bulletin* **2014,** *60*, 730-737.

15. Li, B.; Long, Q.; Duan, D., Effects of ZrO_2 on properties of $BaO–Al_2O_3–B_2O_3–SiO_2$ composites for LTCC applications. *Journal of Materials Science: Materials in Electronics* **2015,** *27* (3), 2824-2829.

16. Ik Jin Choi ·Yong Soo Cho, Effects of various oxide fillers on physical and dielectric properties of calcium aluminoborosilicate-based dielectrics. *Journal of Electroceramics* **2008,** *23* (2-4), 185-190.

17. Sebastian, M. T.; Jantunen, H., Low loss dielectric materials for LTCC applications: a review. *International Materials Reviews* **2013,** *53* (2), 57-90.

18. Ashis Kumar Mandal, Prasanta Kumar Sinha, Santanu Sen, Sitendu Mondal, Chandan Guha and Ranjan Sen, Microwave preparation of $SiO_2-B_2O_3-Na_2O-K_2O-CaO-Fe_2O_3-TiO_2$ glass system. *J. Chem. Chem. Eng.* **2014,** *8*, 349-357.

19. C. E. Curtis, H. G. Sowman, Investigation of therma dissociation, reassociation, and synthesis of zircon. *Journal of the American Ceramic Society* **1953,** *36*, 190-198.

20. Varghese, J.; Joseph, T.; Sebastian, M. T., $ZrSiO_4$ ceramics for microwave integrated circuit applications. *Materials Letters* **2011,** *65* (7), 1092-1094.

21. Robertson, J., High dielectric constant oxides. *The European Physical Journal Applied Physics* **2004,** *28* (3), 265-291.

22. Chung-Lun Lo, Jenq-Gong Duh, Bi-Shiou Chiou, Wen-Hsi Lee, Low-temperature sintering and microwave dielectric properties of anorthite-based glass-ceramics. *J. Am. Ceram. Soc.* **2002,** *85(9)*, 2230 –35.

23. Jean, J.-H.; Gupta, T. K., Devitrification inhibitors in borosilicate glass and binary borosilicate glass composite. *Journal of Materials Research* **1995,** *10* (5), 1312-1320.

24. Xia, G.; He, L.; Yang, D., Preparation and characterization of $CaO–Al_2O_3–SiO_2$ glass/fused silica composites for LTCC application. *Journal of Alloys and Compounds* **2012,** *531*, 70-76.

25. David C. Joy, Alton D. Romig, Jr. and Josepb I. Goldstein, *Principles of Analytical Electron Microscopy*. 1 ed.; Springer US: 1986; p 448.

26. Turnmala, R. R., Ceramic and glass-ceramic packaging in the 1990s. *J. Am. Ceram. Soc.* **1991,** *74*, 895-908.

27. Xia, Q.; Zhong, C.-W.; Luo, J., Low temperature sintering and characteristics of $K_2O–B_2O_3–SiO_2–Al_2O_3$ glass/ceramic composites for LTCC applications. *Journal of Materials Science: Materials in Electronics* **2014,** *25* (10), 4187-4192.

28. Qing, Z.; Li, B.; Li, H.; Li, Y.; Zhang, S., Fabrication and properties of $Li_2O–Al_2O_3–SiO_2$ glass/Al_2O_3 composites for low temperature co-fired ceramic applications. *Journal of Materials Science: Materials in Electronics* **2014,** *26* (3), 1789-1794.

29. Fang, Y.; Li, L.; Xiao, Q.; Chen, X. M., Preparation and microwave dielectric properties of cristobalite ceramics. *Ceramics International* **2012,** *38* (6), 4511-4515.

30. Pagliari, L.; Dapiaggi, M.; Pavese, A.; Francescon, F., A kinetic study of the quartz–cristobalite phase transition. *Journal of the European Ceramic Society* **2013,** *33* (15-16), 3403-3410.

31. Kumar, C. J. D.; Sowmya, T. K.; Sunny, E. K.; Raghu, N.; Venkataramani, N.; Kulkarni, A. R., Influence of Nature of Filler on Densification of Anorthite-Based Crystallizable Glass+Ceramic System for Low Temperature Cofired Ceramics Application. *Journal of the American Ceramic Society* **2009,** *92* (3), 595-600.

32. Gupta, T. K.; Jean, J.-H., Principles of the development of a silica dielectric for microelectronics packaging. *Journal of Materials Research* **2011,** *11* (1), 243-263.

33. Jean, J.-H.; Gupta, T. K., Kinetics of interfacial reaction between borosilicate glass and sapphire substrate. *Journal of Materials Research* **1992,** *7* (9), 2514-2520.

34. Yoshihiko Imanaka, Shigenori Aoki, Nobuo Kamehara, Koichi Niwa, Cristobalite phase formation in glass/ceramics composites. *J. Am. Ceram. Soc.* **1995,** *78*, 1265-1271.

Chapter 5 A crystalline composite for LTCC application

In previous chapters, we have designed four amorphous phase-based composites with dielectric constants ranging from 4 to 12 for LTCC application. In this chapter, instead of using the sol-gel derived amorphous phases, we introduced a cubic $KBSi_2O_6$ phase with simpler composition as the precursor to develop the LTCC materials for the first time. The composite can be sintered between 850°C and 900°C and the resultant sample presents the moderate dielectric performance which is promising for LTCC application in high frequency circuit.

5.1 Introduction

LTCC technology is attracting more and more attention in the field of electronics packaging.[1, 2] But the materials applicable for LTCC are rare because of the low sintering temperature and most conventional electronic ceramics are sintered above 1000°C. To reduce the sintering temperature, some methods are reported, including using low melting point glasses,[3, 4] sintering aids[5, 6] and raw materials with smaller particle size.[7, 8] Among these methods, the intensive reported LTCC materials are based on the glass and ceramic composites since Takada's first report in 1994.[9] Instead of using glasses fabricated by the melt-quench method, we have made the amorphous phases by sol-gel method at lower temperature in previous chapters and the resultant composites exhibit promising performance for LTCC application.

Because the presence of the amorphous phases with complicated compositions might reduce the ease of the LTCC system, some efforts have been made to develop the composites only consisted of crystalline phases.[10, 11] But some problems remain unsolved so that few of them can be used for commercial application. For example, the $ZnNb_2O_6$/CuO composites where CuO acts as the sintering aids,[12, 13] have been reported that they can be sintered at around 900°C, whose temperature satisfies the requirements of LTCC. Nonetheless, most of these materials are with the dielectric constants higher than 20, which is not in favour of rapid signal transmission as the packaging substrates. In addition, it is reported that the TeO_2-based composites can also be sintered below 900°C due to its intrinsic low sintering temperature.[14]

But its toxicity and incapability with silver electrodes have hindered its way to commercial application.[15] Moreover, it has been reported that some compounds with the specific structures, such as the spinel-like $NaAgMoO_4$, can be sintered below 800°C.[16] However, such a low sintering temperature is unfavourable of completely removing the organic compounds which is used for tape casting process of manufacturing LTCC devices.[11, 17] The residual organics are harmful to the dielectric properties. Besides these, the LTCC substrate requires the potential candidates to be highly insulating. Intuitively, the potential candidates for LTCC should have high intrinsic resistivity. However, investigation about improving the resistivity of the LTCC materials is rather few.

In this work, we developed an amorphous phase-free composite which has the moderate dielectric constant (~8) and associated performance when sintered between 850°C and 900°C. Herein, the $KBSi_2O_6$ phase, which was found by Voldan J.,[18] was synthesized by the solid state reaction and introduced as the main matrix for the LTCC material. The advantage of this silicate is in its good tolerance for ionic substitutions (such as Al substituting B) under low temperature, which can lead to intimate contact of phases in the sintered sample to achieve well densified microstructure.[19, 20] With this silicate, we combined it with Al_2O_3, as well as CaO, to develop a novel composite for LTCC application and the resistivity of this composite was also investigated.

5.2 Experimental procedures

The $KBSi_2O_6$ phase was initially synthesized by the solid-state reaction as follows. The K_2CO_3 (≥99%, Chem-supply), H_3BO_3 (≥99.5%, the British drug houses LTD.) and SiO_2 (99.50%, Sigma-Aldrich) were weighted according to the stoichiometric formulation of $KBSi_2O_6$ and then ball milled in the Teflon jars for 12h. The dried powder mixtures were uniaxially pressed into pellets and then heated at 800°C for 2h. After that, the sintered pellets were ground and ball milled into fine powders again.

The CaO was obtained by calcining $CaCO_3$ at 1000°C for 2h and naturally cooling to 200°C followed by transferring into the furnace with the temperature of 150°C for storage. Then

various amount of Al_2O_3, as-synthesized $KBSi_2O_6$ and CaO were weighted and ball milled with absolute ethanol in the Teflon jars. The resultant mixture was first dried and then uniaxially pressed into pellets at 7MPa and sintered between 850°C and 900°C for 6h. To check the compatibility with silver electrode, the raw material with composition of Al_2O_3: $KBSi_2O_6$: CaO=1.07:1:0.4 (mole ratio) was granulated with 5wt% polyvinyl butyral (PVB) and then pressed into pellets under 7MPa. The silver electrodes were coated on the surfaces of the green samples followed by co-firing at 450°C for 2h to get rid of the major binders. Finally, the samples were further heated between 850°C and 900°C.

5.3 Compositions, structures and electrical properties of the crystalline composite

To illustrate that there is no amorphous phase in this composite, the phases of raw materials are first characterized by XRD to check their crystallinity. In our experiments, Al_2O_3 with particle size of 135nm, 300nm and 1μm are involved. Fig. 5-1a presents the XRD patterns of raw Al_2O_3 powder with different particle sizes and all the peaks can be indexed to hexagonal corundum phase (ICSD code: 52647). And the peak-width is getting finer when the particle size changing from 135nm to 1μm. Fig. 5-1b shows the XRD patterns of $CaCO_3$ raw powders where all the main peaks can be indexed referring to the hexagonal $CaCO_3$ phase (ICSD code: 158257) and no secondary phase is detected. After calcined at 1000°C, $CaCO_3$ is decomposed completely and all peaks can be indexed to cubic CaO phase (ICSD code: 51409) as illustrated in Fig. 5-1b. The pure $KBSi_2O_6$ phase is also successfully synthesized at 800°C by the solid state reaction. Fig. 5-2 shows the XRD pattern of as-synthesized $KBSi_2O_6$ powder and all the observed peaks can be indexed to the single cubic $KBSi_2O_6$ phase (ICSD code: 39105). Therefore, all the three components, which will be involved in our composite, are crystalline materials.

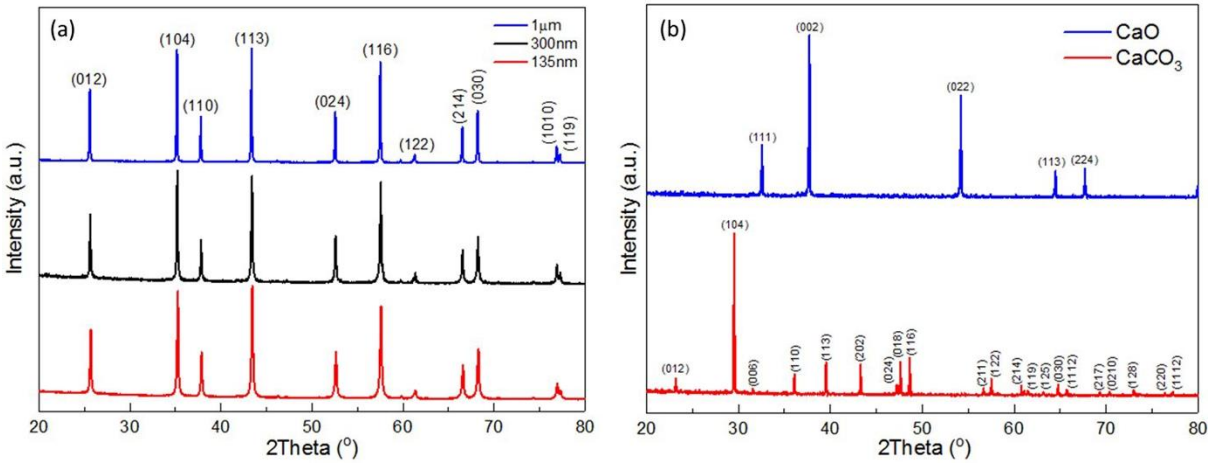

Fig. 5-1 XRD patterns of raw materials (a) Al_2O_3 powders with different particle sizes; (b) $CaCO_3$ powders before and after calcination at 1000°C.

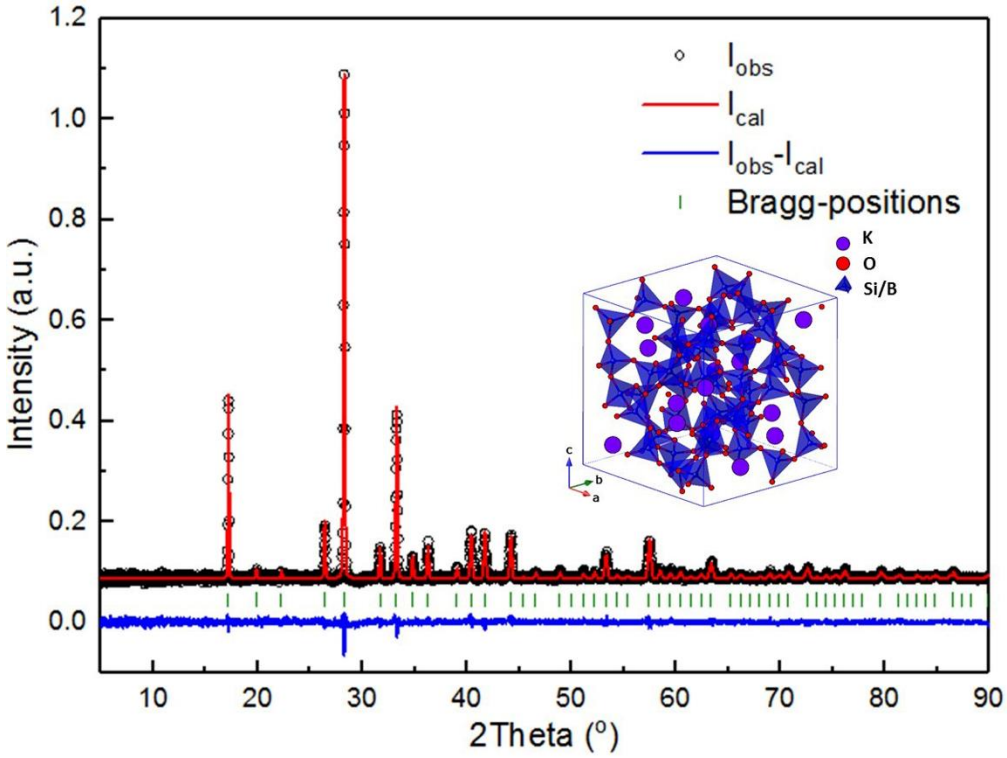

Fig. 5-2 XRD refinement result of the as-synthesized $KBSi_2O_6$ phase using Rietveld method. The inserted plot presents its crystal structure, where the B and Si occupy the same site.

To reveal more structure details of the homemade $KBSi_2O_6$ phase, the observed XRD pattern is further refined using Rietveld method in Fig. 5-2. The refinement result is consistent with the observed pattern with small intensity difference. The single phase model can lead to

reasonable results with the following reliability factors: R_p=4.88, R_{wp}= 6.65 and GOF=1.27. The refinement result shows the lattice parameters of the as-synthesized $KBSi_2O_6$ are $a=b=c$=12.61826Å and $\alpha=\beta=\gamma$=90°, with the space group of I-43d. The crystal structure of the $KBSi_2O_6$ is presented in the inserted plot, where each corner oxygen is shared by two $(Si/B)O_4$ tetrahedra and K occupies the cavities formed by the tetrahedra, and corresponding atomic fractional coordinates are listed in Tab. 5-1. It is noteworthy that within this structure, Si and B occupy the same site randomly with the mole ratio of 2:1. These structure parameters are in line with those reported by IHARA M. et al.[21]

Tab. 5-1 Refined atomic fractional coordinates from XRD data for $KBSi_2O_6$ sample.

Atom	Site	Occupancy	x	y	z	Biso/ADP
K	16c	0.333333	0.117592	0.117592	0.117592	0.041484
B	48e	0.333	0.124553	0.167602	0.408142	0.019792
Si	48e	0.667	0.124553	0.167602	0.408142	0.019792
O1	48e	1	0.23448	0.139057	0.356759	0.015274
O2	48e	1	0.120608	0.289874	0.425088	0.001267

We first adopted $CaCO_3$ as the source of calcium and the mole ratio of three raw materials is Al_2O_3 (135nm): $KBSi_2O_6$: $CaCO_3$=1: 0.5: 0.6. It can be seen in Fig. 5-3a that for this composition sintered at 950°C, 1000°C and 1050°C, the low dielectric loss (<0.1%) only can be obtained when the sintering temperature is higher than 1000°C. As $CaCO_3$ will decompose into CaO and CO_2 at high temperature, the by-product CO_2 possibly impacts the densification with pores in the sintered pellets, thereby deteriorating the dielectric properties. In order to reduce the impacts arising from the decomposition, $CaCO_3$ is replaced by CaO without varying the mole ratio, and it can be found that the low dielectric loss is achieved at 950°C. Besides, resistivities of samples have been improved to $10^{11}\Omega\cdot$cm level, without any negative influence to other performance. Therefore, using CaO as the source of calcium in the raw materials could realize the low dielectric loss, shrinkage and high resistivity at lower sintering temperature,

which are the basic requirements for LTCC devices. However, the relative permittivity is still a little bit higher than the target.

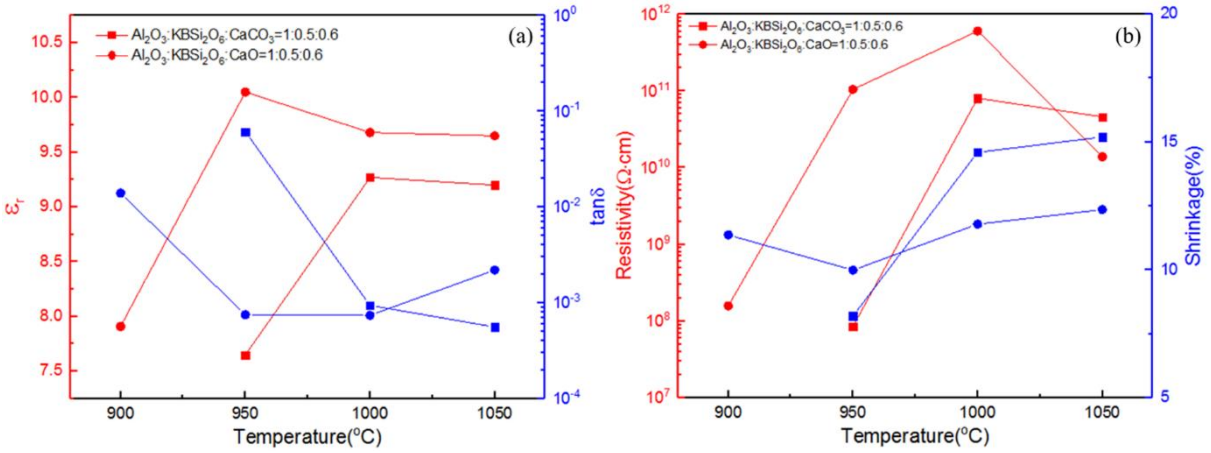

Fig. 5-3 (a) Dielectric properties (@1MHz); (b) Resistivities and shrinkages in XY plane of the sintered samples with $CaCO_3$ and CaO as calcium source.

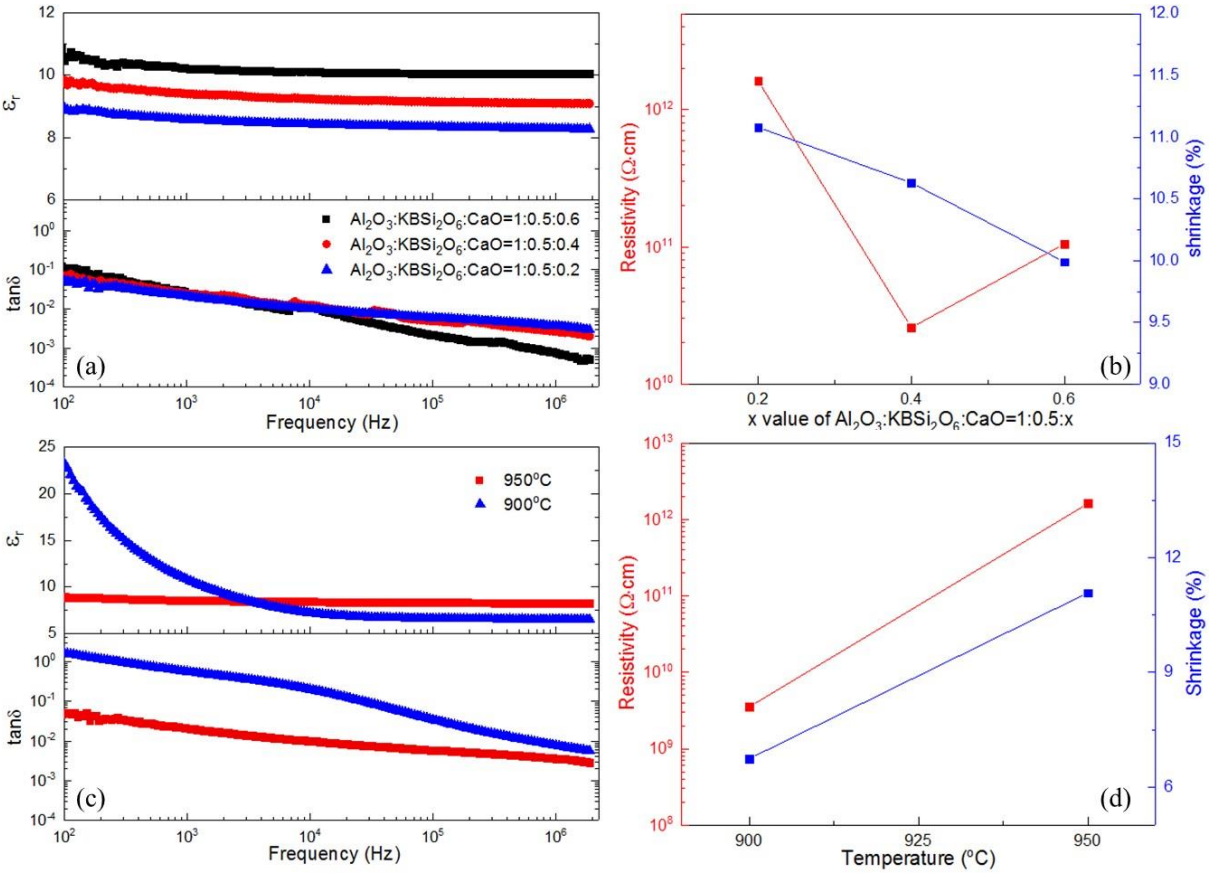

Fig. 5-4 (a) Dielectric properties; (b) Resistivities and XY-shrinkages of samples with various amount of CaO sintered at 950°C; (c) and (d) performance of samples with composition of

Al_2O_3(135nm): $KBSi_2O_6$: CaO=1: 0.5: 0.2 sintered between 900°C and 950°C.

In order to tune the relative permittivity, we need to further optimise the recipe and here we firstly try to modify the amount of CaO. It can be seen in Fig. 5-4 that the specimen with composition of Al_2O_3 (135nm): $KBSi_2O_6$: CaO=1: 0.5: 0.2 has the relative permittivity of 8.29 (@1MHz), dielectric loss of 0.003 (@1MHz), resistivity of $1.62\times10^{12}\Omega\cdot$cm and shrinkage of 11.08% when sintered at 950°C. However, when reducing the sintering temperature to 900°C, some performance, such as dielectric loss and resistivity, has degenerated seriously in Fig. 5-4c and Fig. 5-4d. As a result, although the relative permittivity can be adjusted by changing the mole ratio of CaO in raw materials, the sintering temperature is still too high for the composite to co-fire with silver electrode.

To decrease the sintering temperature, we further adjust the mole ratio between the low melting point $KBSi_2O_6$ (1095°C) and high melting point CaO (2572°C) raw materials.[22] We initially increase the amount of $KBSi_2O_6$ and it can be seen in Fig. 5-5a that samples with more amount of $KBSi_2O_6$ can achieve low dielectric loss even when sintered as low as ~850°C. Therefore, addition of $KBSi_2O_6$ is proved to be an effective way to lower the sintering temperature. However, the resistivity in Fig. 5-5b is below $10^{10}\Omega\cdot$cm. In addition, various amount of CaO are further modulated in these two composites. With regard to the composition of Al_2O_3 (135nm): $KBSi_2O_6$: CaO=1: 0.75: x, as illustrated in Fig. 5-5c, the dielectric loss remains in the low level (0.2%) except the sample with composition of Al_2O_3 (135nm): $KBSi_2O_6$: CaO=1: 0.75: 0.6 sintered at 850°C. This might be because the addition of high melting point CaO raw material will influence the sintering temperature, and the low sintering temperature possibly reduces the density of the pellet. For the samples synthesized in this experiment, the highest resistivity is achieved when x = 0.4 (in Fig. 5-5d) and this result is independent of the sintering temperature. However, the dielectric constant of this composition, as shown in Fig. 5-5c, is almost close to 10 even sintered at 850°C, which is still high compared with required value. In terms of the composition of Al_2O_3 (135nm): $KBSi_2O_6$: CaO=1:1:x (x = 0.2, 0.4 and 0.6), as illustrated in Fig. 5-5e, all samples show low dielectric loss when sintered at 850°C and 900°C.

For this batch of samples, the highest resistivity is obtained for the sample with x = 0.4 sintered at 900°C (in Fig. 5-5f). What is more, the relative permittivity of ~9.25 (in Fig. 5-5e) is closer to the requirements than that of Al_2O_3 (135nm): $KBSi_2O_6$: CaO=1: 0.75: x composite. Among above experiments, samples with composition of Al_2O_3 (135nm): $KBSi_2O_6$: CaO=1: 1: 0.4 and sintered at 900℃ present the best performance. So further optimization would be based on this composition.

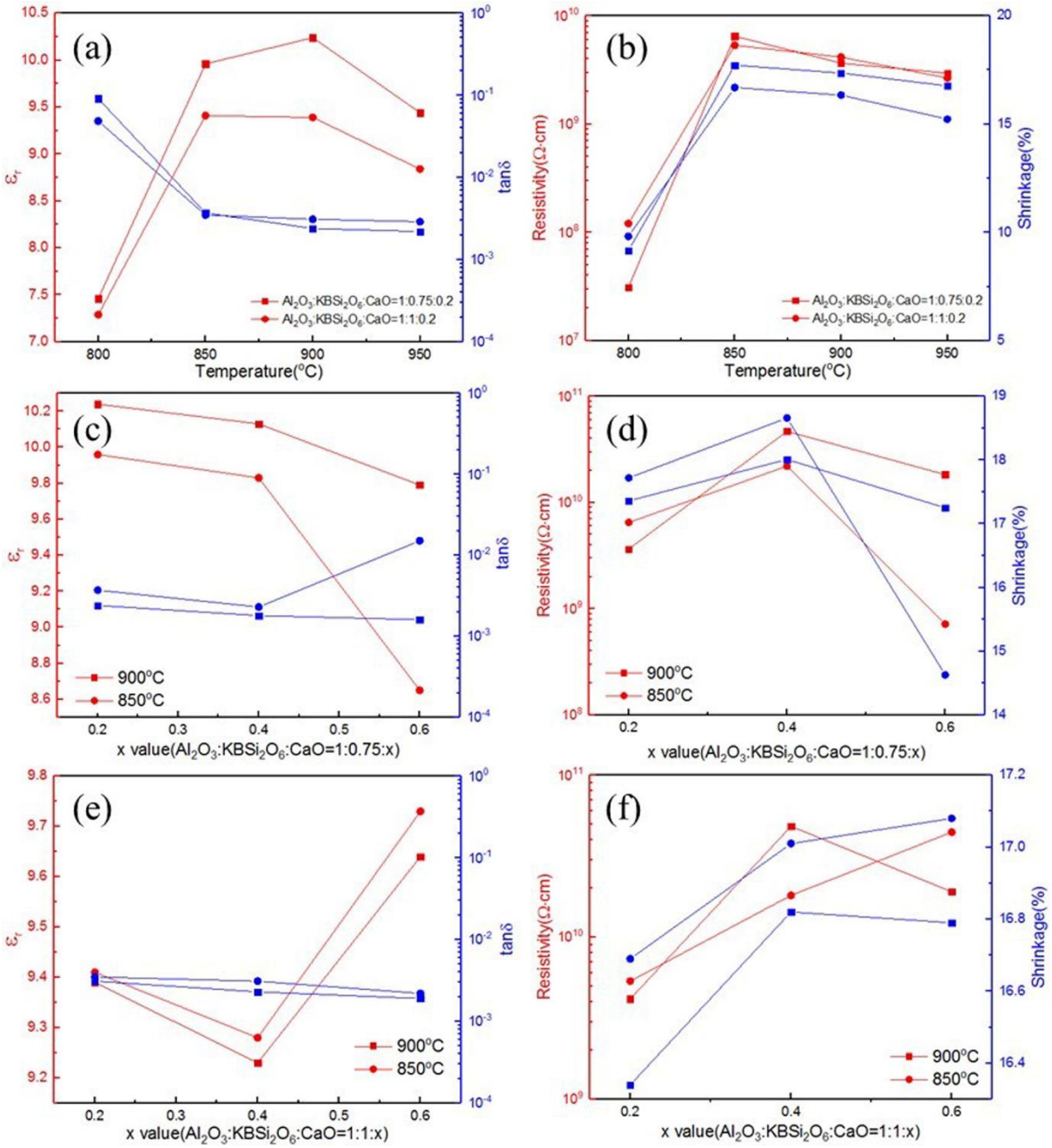

Fig. 5-5 (a) and (b) Electrical properties and XY shrinkages of samples with addition of $KBSi_2O_6$ sintered from 800°C to 950°C; (c) and (d) electrical properties and XY shrinkages of

samples with various amount of CaO in Al_2O_3: $KBSi_2O_6$: CaO =1: 0.75: x composite sintered at 850°C and 900°C; (e) and (f) electrical properties and XY shrinkages of samples with various amount of CaO in Al_2O_3: $KBSi_2O_6$: CaO =1: 1: x composite sintered at 850°C and 900°C.

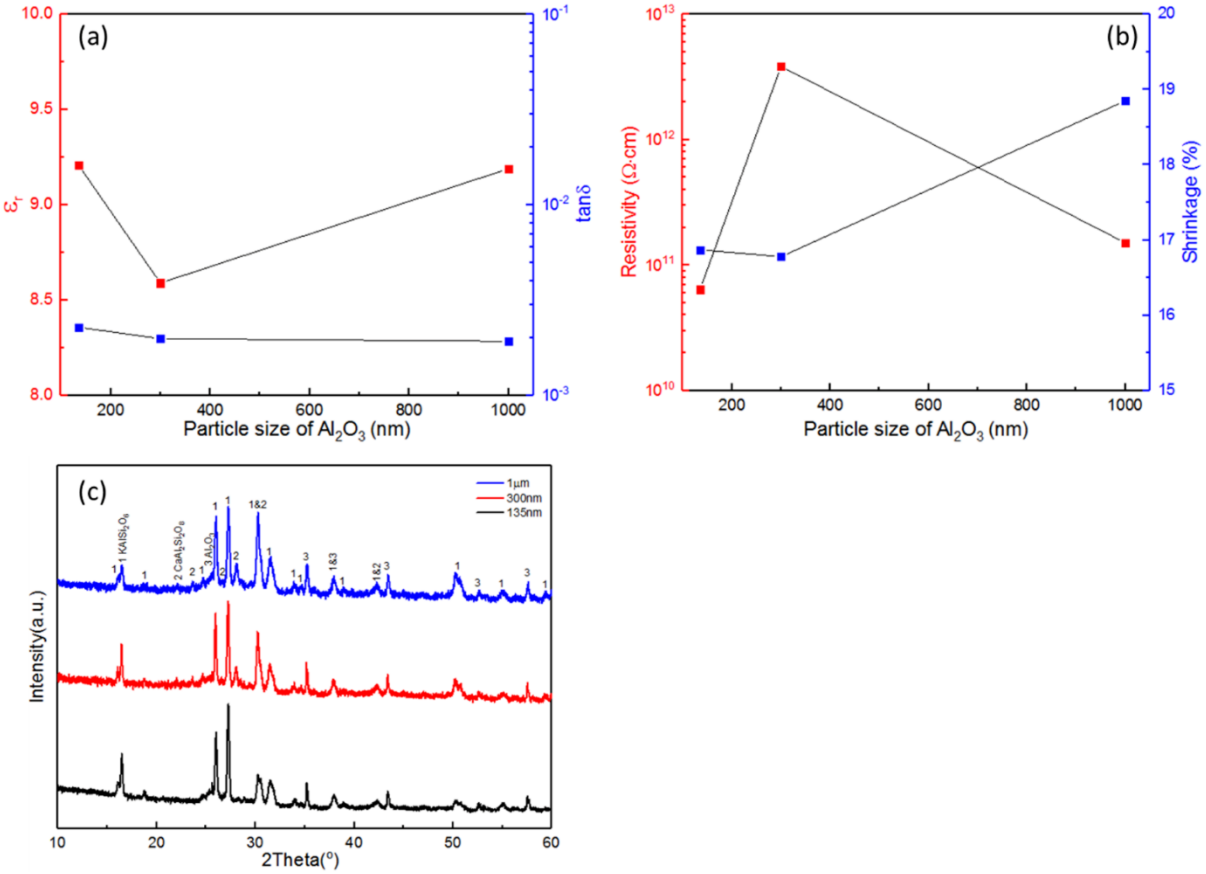

Fig. 5-6 (a) Dielectric properties; (b) resistivities and XY shrinkages; (c) XRD patterns of samples with Al_2O_3 at different particle sizes in composition of Al_2O_3: $KBSi_2O_6$: CaO=1: 1: 0.4 sintered at 900°C.

It is reported that the particle size of alumina has impacts on densification and crystallization process because of different specific surface area.[8] So alumina with different sizes (135nm, 300nm and 1μm) have also been tried in raw materials and corresponding performance is shown in Fig. 5-6. As presented in Fig. 5-6a, three samples have the dielectric loss in the similar level, which are all around 0.002 @1MHz. But the sample with Al_2O_3 at 300nm in the nominal composition has the lowest dielectric constant of ~8.59 and the highest resistivity (above 10^{12}Ω·cm in Fig. 5-6b) when sintered at 900°C. To further check the influence caused by the particle size of Al_2O_3, the XRD patterns of samples synthesized by different Al_2O_3 raw materials are presented in Fig. 5-6c. For the sample with 135nm Al_2O_3, the phases presented

include tetragonal $KAlSi_2O_6$ phase (ICSD code: 161631) and hexagonal Al_2O_3 phase (ICSD code: 52647). Herein the Ca and B might occupy the K and Al site in the $KAlSi_2O_6$ phase, respectively.[23-25] While the samples with larger sized Al_2O_3 additionally contain the monoclinic $CaAl_2Si_2O_8$ phase (ICSD code: 86329). So the crystallization process shows evident dependence on the particle size of Al_2O_3. On balance, it can be concluded that the sample synthesized by the 300nm Al_2O_3 presents the best performance.

Based on above optimization for each component, we developed the sample with the composition of Al_2O_3 (300nm): $KBSi_2O_6$: CaO=1: 1: 0.4 (mole ratio). As shown in Fig. 5-7, there are three phases presented in the samples sintered between 850°C and 900°C, that is, tetragonal $KAlSi_2O_6$ phase (ICSD code: 161631), hexagonal Al_2O_3 phase (ICSD code: 52647) and monoclinic $CaAl_2Si_2O_8$ phase (ICSD code: 86329). During the sintering, the cubic $KBSi_2O_6$ phase in the raw materials has transformed to tetragonal phase due to partial substitution of B by Al.[21, 26] What is more, the intensities of peaks, especially for the peak around 28°, originated from the $CaAl_2Si_2O_8$ phase are relatively weak when sintered at 850°C, while they increase as the sintering temperature rising.

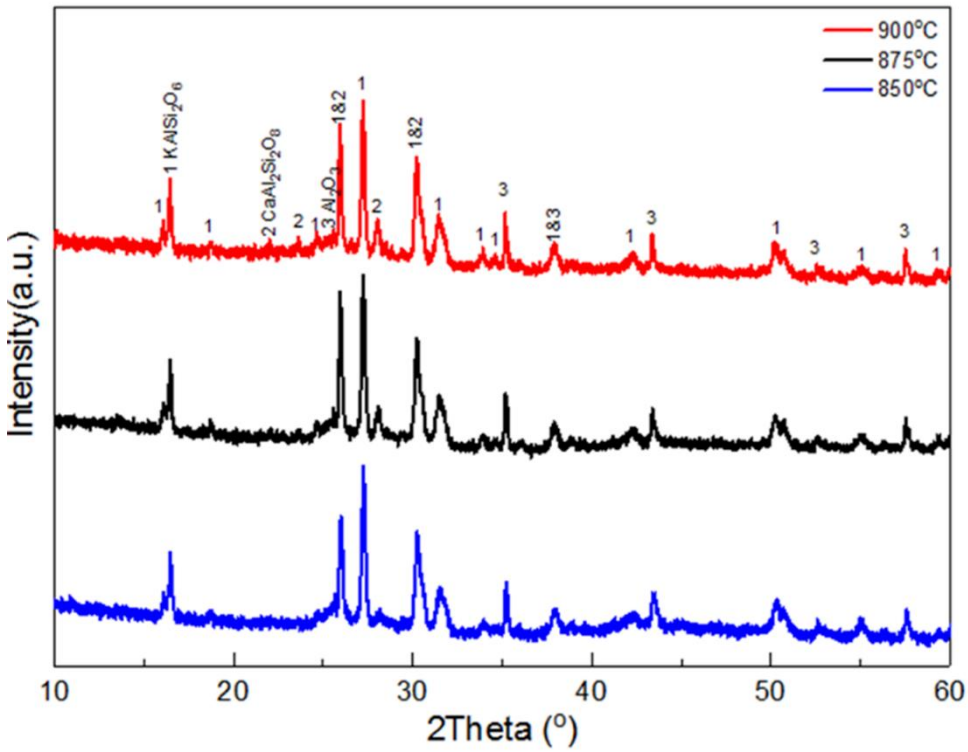

Fig. 5-7 XRD patterns of samples with the composition of Al_2O_3 (300nm): $KBSi_2O_6$: CaO=1:

1: 0.4 (mole ratio) sintered between 850°C and 900°C.

The above samples with the composition of Al_2O_3 (300nm): $KBSi_2O_6$: CaO=1: 1: 0.4 also show good electrical properties. It can be seen in Fig. 5-8a that the samples show relative permittivity of 8.3~8.6 and dielectric loss below 0.003 @1MHz when sintered at 850°C, 875°C and 900°C. These dielectric properties are quite good for LTCC application. As reported, the dielectric properties of composite relate to the phases presented and their fractions. Although the amount of $CaAl_2Si_2O_8$ phase is changing with the sintering temperature, as shown in Fig. 5-7, it doesn't cause obvious difference in dielectric constant. This is mainly because it has the similar dielectric constant (~6.9) with that of the main $KAlSi_2O_6$ phase (~6.8).[27] In addition, all samples sintered at different temperatures have resistivities as high as $10^{12}\Omega\cdot$cm, exhibiting good insulating property.

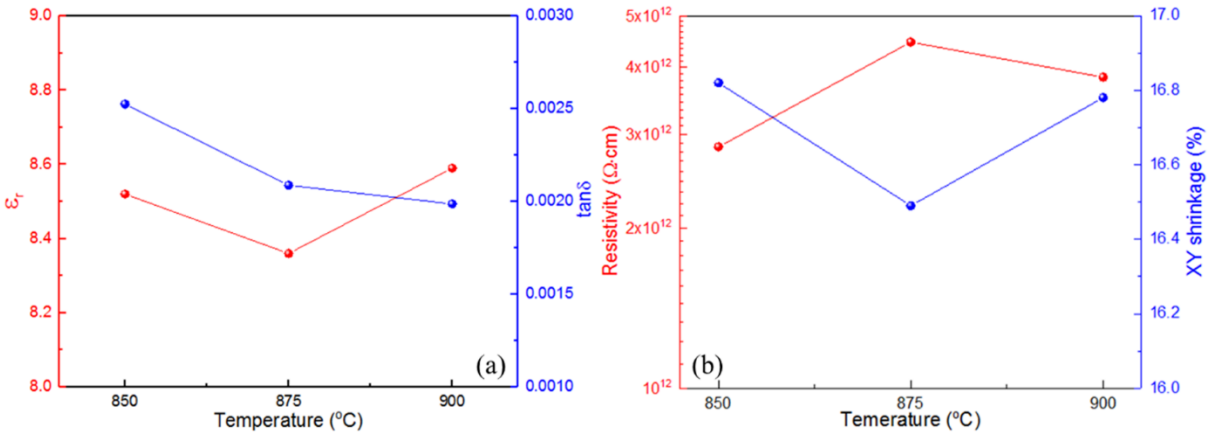

Fig. 5-8 (a) Dielectric properties of samples with the composition of Al_2O_3 (300nm): $KBSi_2O_6$: CaO=1: 1: 0.4 (mole ratio) @1MHz sintered from 850°C to 900°C; (b) resistivities of the corresponding samples tested under 100V (DC) and shrinkages in XY plane.

5.4 Improvement of resistivity and associated properties

Fig. 5-9 illustrates the XRD patterns of samples with composition of Al_2O_3 (300nm): $KBSi_2O_6$: CaO=1: 1: 0.4 sintered at 900°C for various soaking period. It can be seen that no trace of the crystal peak related to the $CaAl_2Si_2O_8$ phase exists in the sample which just sintered for 0.5

hour. In contrast, peaks associated with the $CaAl_2Si_2O_8$ phase become evident when the soaking period extends to 6 hours and their intensities remain similar to the sample sintered for 12h. Therefore, the whole sintering process in this composite might contain two stages. In the first stage, the Al_2O_3 mainly reacts with $KBSi_2O_6$ to form the $KAlSi_2O_6$ phase. After that, the resultant might react with each other to form the $CaAl_2Si_2O_8$ phase.

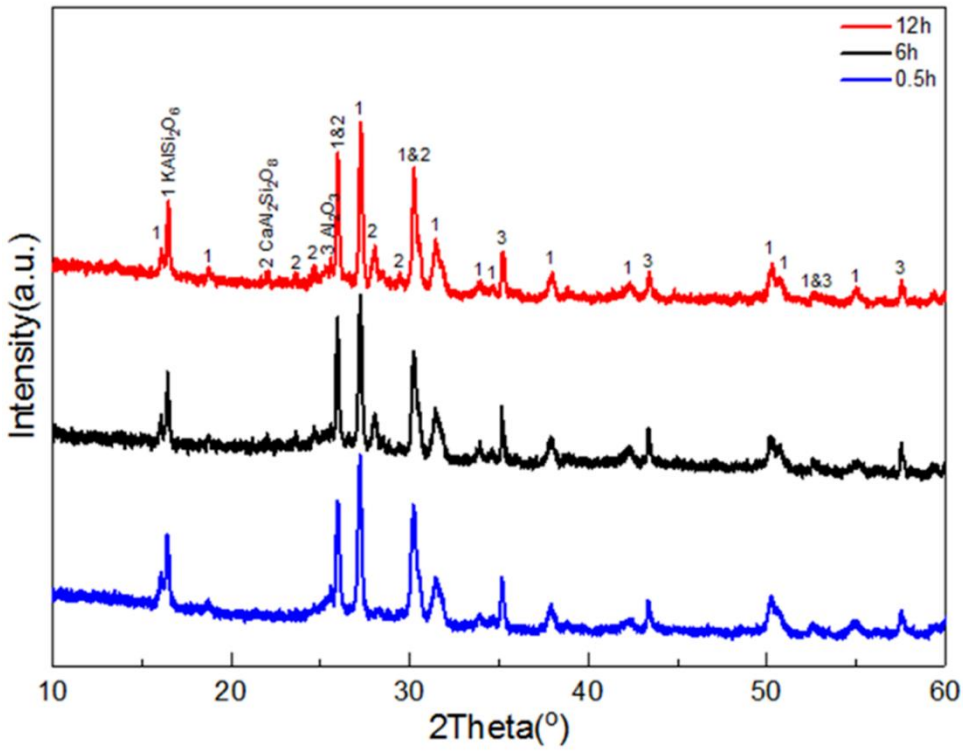

Fig. 5-9 XRD patterns of samples with composition of Al_2O_3 (300nm): $KBSi_2O_6$: CaO=1:1:0.4 sintered at 900°C for 0.5h, 6h and 12h.

Fig. 5-10a shows that the resistivities of samples with composition of Al_2O_3 (300nm): $KBSi_2O_6$: CaO=1: 1: 0.4 sintered at 900°C for various soaking period. According to the XRD results in Fig. 5-9, the amount of the $CaAl_2Si_2O_8$ phase has increased evidently by adjusting the soaking period from 0.5h to 6h. However, when comparing the resistivities of samples sintered for 0.5h and 6h, these values does not show significant differences. When the sintering time further extends to 12h, no obvious change of the phase fraction of $CaAl_2Si_2O_8$ can be obtained in the XRD pattern but the resistivity of sample is obviously enhanced. Therefore, the $CaAl_2Si_2O_8$ phase has no evident influence on the resistivity. In addition, although the resistivity can be

improved by extending the soaking period to 12h, such a long soaking time might not be an economical way for industry production.

The CaO in the raw materials is necessary for the crystallization of $CaAl_2Si_2O_8$ phase which does not present significant impacts on the resistivity of resultant samples. Therefore, to achieve the sample with higher resistivity, the amounts of other raw materials, *i.e.*, Al_2O_3 and $KBSi_2O_6$, are further adjusted. As illustrate in Fig. 5-10b, when 2wt% $KBSi_2O_6$ introduced into nominal Al_2O_3: $KBSi_2O_6$: CaO=1: 1: 0.4 composite, the resistivity has been slightly improved. In contrast, when the same amount of Al_2O_3 introduced, the resistivity has been evidently improved to $10^{13}\Omega\cdot$cm. What is more, its resistivity can remain at such a high level even when the sintering temperature decreases to 850°C. Based on this, we tried to further introduce more amount of Al_2O_3 into the composite to improve the resistivity. However, even 10wt% additional Al_2O_3 introduced, it shows similar result as that with introduction of 2wt% Al_2O_3. In addition, the sample added with 10wt% $KBSi_2O_6$ shows higher resistivity than that with 2wt% $KBSi_2O_6$. But its resistivity is still not as good as that with 10wt% Al_2O_3. Therefore, addition of Al_2O_3 should be a more effective way to improve resistivity than $KBSi_2O_6$.

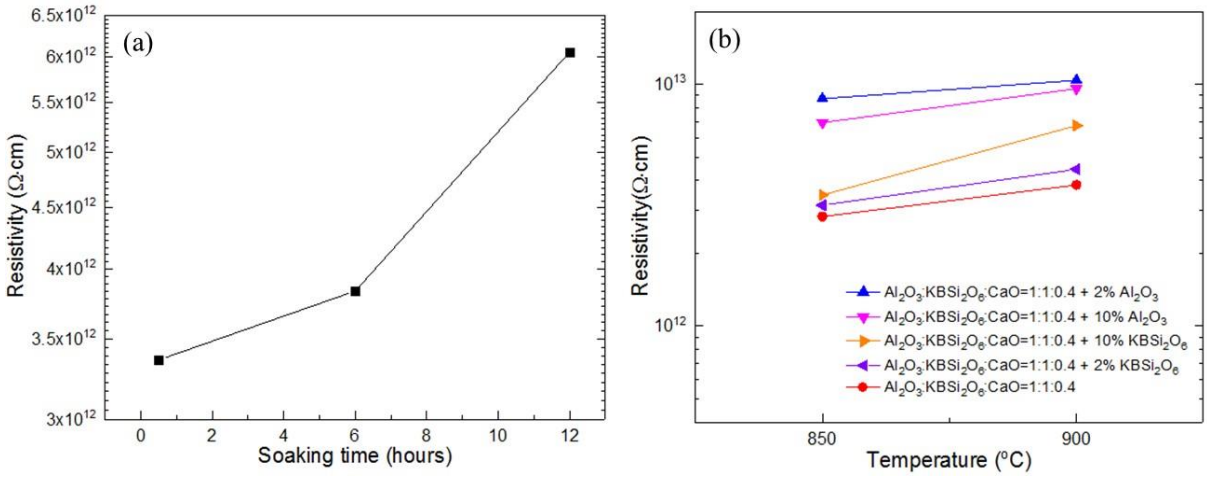

Fig. 5-10 (a) Resistivities of samples with composition of Al_2O_3 (300nm): $KBSi_2O_6$: CaO=1: 1: 0.4 sintered at 900°C for different time; (b) influence of Al_2O_3 (300nm) and $KBSi_2O_6$ on resistivities of developed samples sintered from 850°C to 900°C for 6h.

Although the introduction of Al_2O_3 can improve the resistivity, the side effect on other

properties, such as dielectric properties, is not expected. Fig. 5-11 confirms that for the sample with composition of Al_2O_3: $KBSi_2O_6$: CaO=1: 1: 0.4, addition of 2wt% Al_2O_3 could lead to smaller dielectric constant than that with additional 10wt% Al_2O_3 while the dielectric loss remains almost the same. For the LTCC devices used for rapid signal transition, the small dielectric constant are expected. In consequence, 2wt% Al_2O_3 addition to this composite would be the better choice and now the recipe is optimized as Al_2O_3 (300nm): $KBSi_2O_6$: CaO=1.07:1:0.4 (mole ratio).

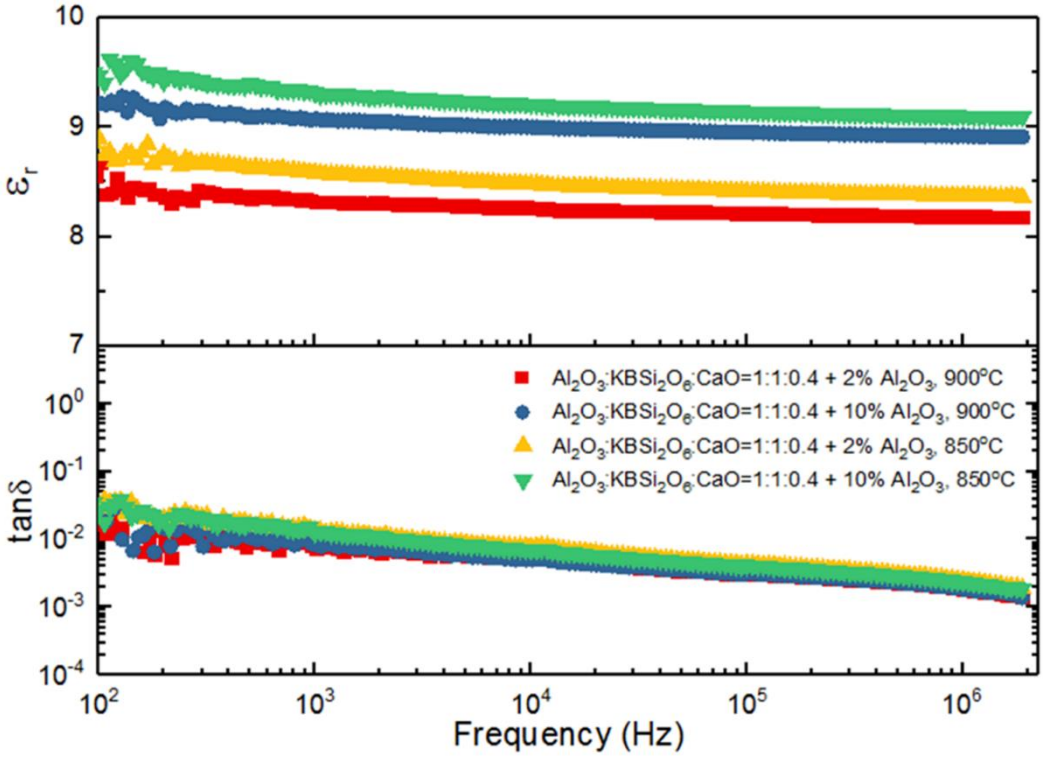

Fig. 5-11 Dielectric properties of samples with addition of 2%~10% Al_2O_3 (300nm) sintered between 850°C and 900°C.

The thermal expansions of optimized samples are linear and the CTE values decrease with the rising of sintering temperature. Fig. 5-12a shows the CTE of samples with composition of Al_2O_3 (300nm): $KBSi_2O_6$: CaO=1.07: 1: 0.4 from room temperature to 300°C. It can be seen that the sample sintered at 850°C shows the linear thermal expansion and the CTE is calculated as 12.46ppm/°C, while that of the sample sintered at 900°C decreases to 11.04ppm/°C. The CTE of the composite depends on that of phases presented and their fraction. The XRD patterns

in Fig. 5-12b illustrate that the phases present in the samples sintered between 850°C and 900°C all include tetragonal $KAlSi_2O_6$ phase (ICSD code: 161631) and hexagonal Al_2O_3 phase (ICSD code: 52647). The amount of monoclinic $CaAl_2Si_2O_8$ phase (ICSD code: 86329) grows with increasing the sintering temperature. Among the present phases, the $CaAl_2Si_2O_8$ phase has the lowest CTE of 4.8ppm/°C.[28] Thus, the decrease of CTE value is caused by the increasing proportion of the $CaAl_2Si_2O_8$ phase. In addition, these CTE values match with that of printed circuit board (PCB), thus the misregistration can be avoided in real application.[29]

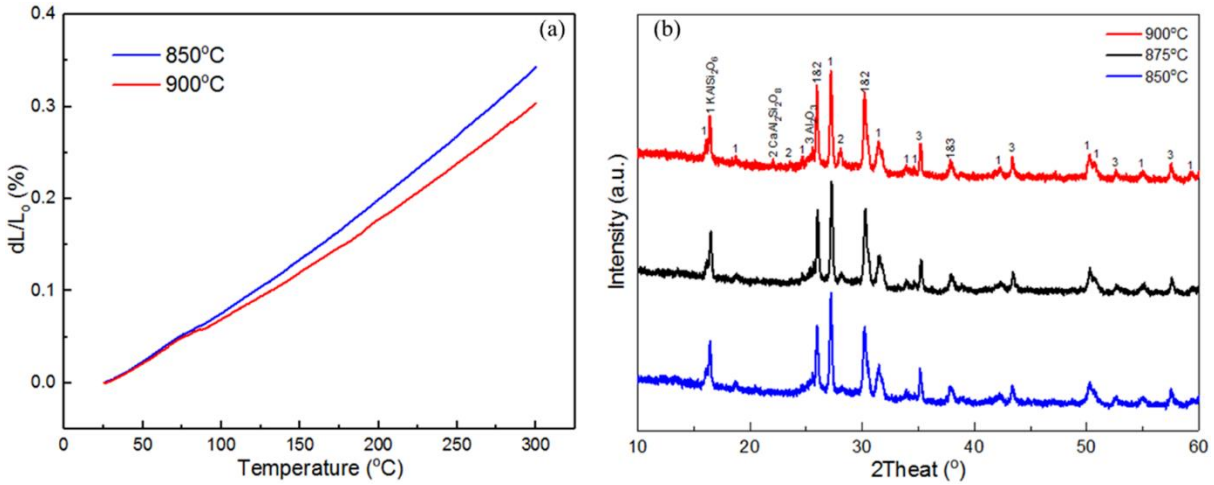

Fig. 5-12 (a) Coefficients of thermal expansion (CTE); (b) XRD patterns of samples with composition of Al_2O_3 (300nm): $KBSi_2O_6$: CaO=1.07: 1: 0.4 sintered between 850°C and 900°C.

The microstructures of the above samples sintered at different temperatures in the range from 850°C to 900°C are displayed in Fig. 5-13. It can be seen that all samples show well densified surfaces without pores. As shown in Fig. 5-13b, there are some particles (as the arrow point out) distributing in the sample sintered at 850°C. With increasing the sintering temperature to 875°C, some dots comes out around the particles in Fig. 5-13d. Comparing with the XRD patterns of the samples sintered at 850°C and 875°C in Fig. 5-12b, it is highly possible that the white dots have relationship with the $CaAl_2Si_2O_8$ phase. The size of particles surrounded by $CaAl_2Si_2O_8$ phase are gradually reducing with the sintering temperature in Fig. 5-13f due to the reaction with other phase to form $CaAl_2Si_2O_8$ phase.

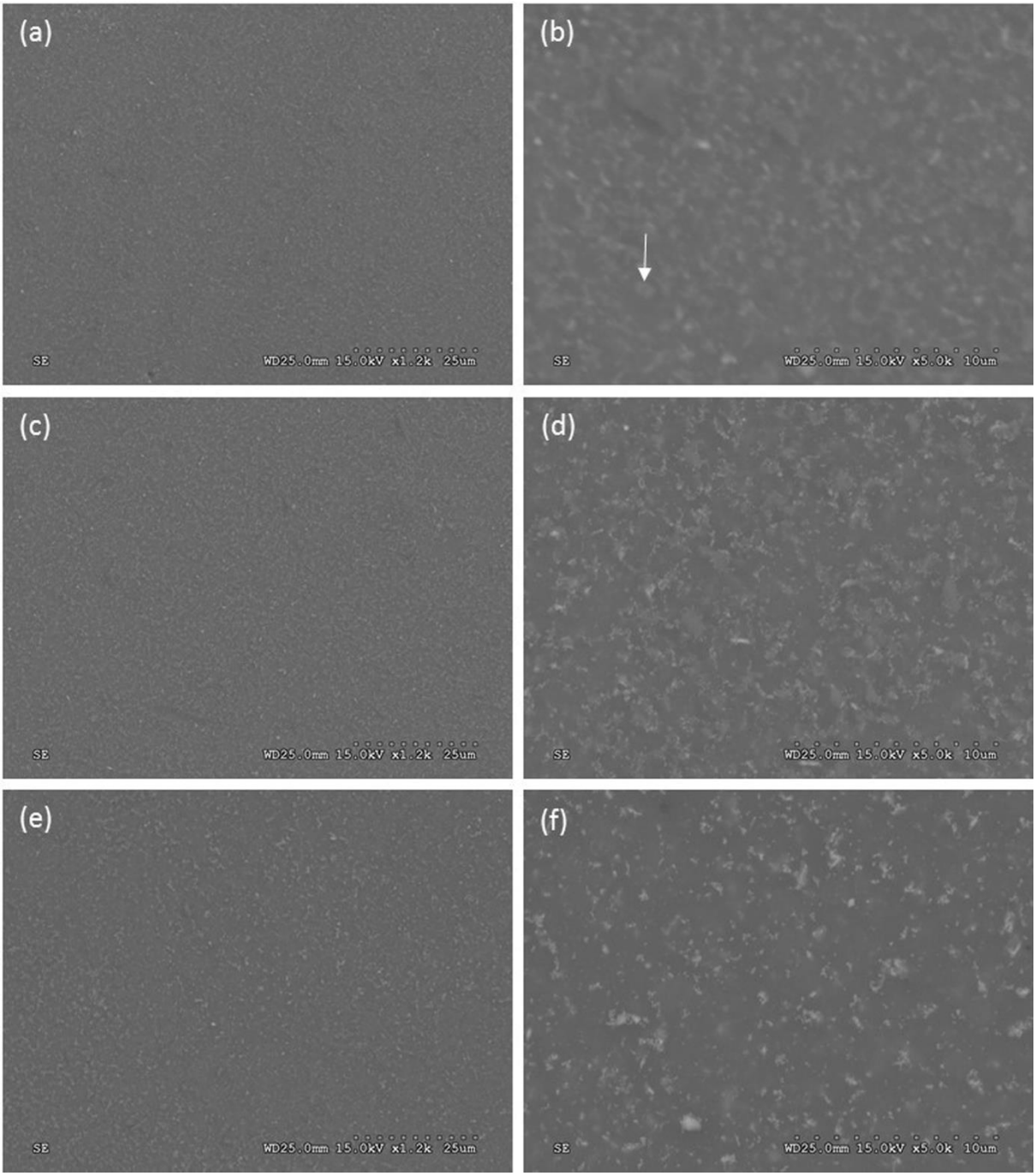

Fig. 5-13 SEM images of samples with composition of Al_2O_3 (300nm): $KBSi_2O_6$: CaO=1.07:1:0.4 sintered at (a) and (b) 850°C; (c) and (d) 875°C; (e) and (f) 900°C.

The backscattered electron (BSE) image of sample sintered at 850°C is present in Fig. 5-14. Except the dark and grey regions based on the image contrast, there are also some white dots surrounding the grey particles. Point analyses are conducted to identify the phases and corresponding results are list in Tab. 5-2, but they are not able to reveal the exact chemical composition of each phase due to the existence of B element and small particle size. The dark

regions relate to the Al_2O_3 phase according to the point analyses. These regions are rich in Al and the K/Al, Si/Al, as well as Ca/Al value are rather low, which means K, Si and Ca are not involved in this phase. The grey regions are surrounded by many small white dots (particle size <1μm), so that it is hard to achieve exact composition of them. Compared with the XRD results, they should relate to the $KAlSi_2O_6$ phase and $CaAlSi_2O_8$ phase. Because the grey regions have large area than white dots and the Ca/K ratio on the white dot is higher than that in the grey regions based on the point analyses in Tab. 5-2, the grey regions and white dots should relate to the $KAlSi_2O_6$ phase and $CaAlSi_2O_8$ phase, respectively.

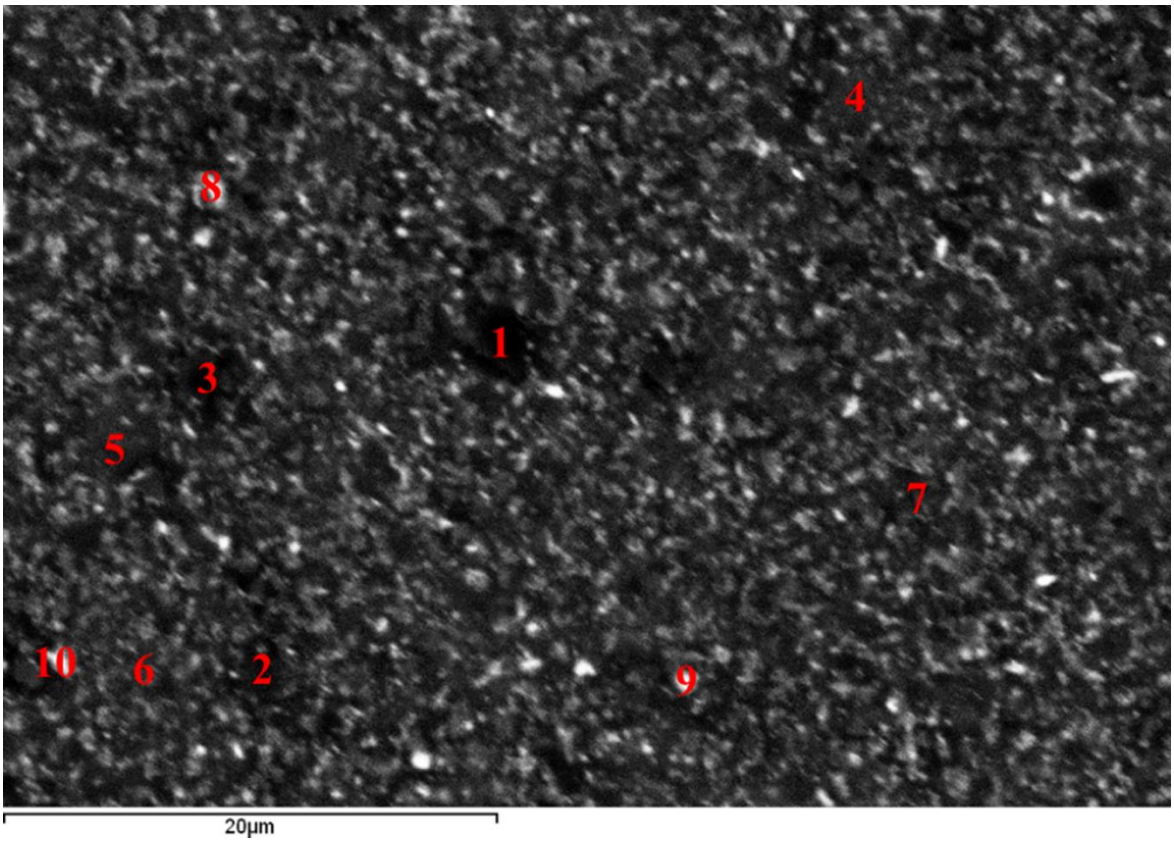

Fig. 5-14 Backscattered electron image of sample with composition of Al_2O_3 (300nm): $KBSi_2O_6$: CaO=1.07:1:0.4 sintered at 850°C. The numbers specify the locations of point analyses.

Tab. 5-2 Point analyses of different regions in the sample sintered at 850°C.

Spectrum	O	Al	Si	K	Ca	Si/Al	K/Al	Ca/Al	Ca/K
Spectrum 1	59.99	35.20	2.75	1.49	0.57	0.08	0.04	0.02	0.39

Dark region	Spectrum 2	63.09	27.55	5.50	2.79	1.07	0.20	0.10	0.04	0.38
	Spectrum 3	61.62	28.13	6.31	2.79	1.15	0.22	0.10	0.04	0.41
	Average	61.57	30.29	4.85	2.36	0.93	0.16	0.08	0.03	0.39
Grey region	Spectrum 4	61.35	12.22	16.95	8.38	1.10	1.39	0.69	0.09	0.13
	Spectrum 5	60.78	14.19	15.73	7.44	1.86	1.11	0.52	0.13	0.25
	Spectrum 6	61.94	13.35	14.81	7.71	2.20	1.11	0.58	0.17	0.29
	Spectrum 7	61.26	13.54	15.78	7.76	1.65	1.17	0.57	0.12	0.21
	Average	61.33	13.32	15.82	7.82	1.71	1.19	0.59	0.13	0.22
White dots	Spectrum 8	63.71	20.32	9.12	4.74	2.11	0.45	0.23	0.10	0.44
	Spectrum 9	60.60	16.41	14.45	6.69	1.84	0.88	0.41	0.11	0.28
	Spectrum 10	62.75	16.31	12.65	6.27	2.01	0.78	0.38	0.12	0.32
	Average	62.35	17.68	12.07	5.90	1.99	0.68	0.34	0.11	0.35

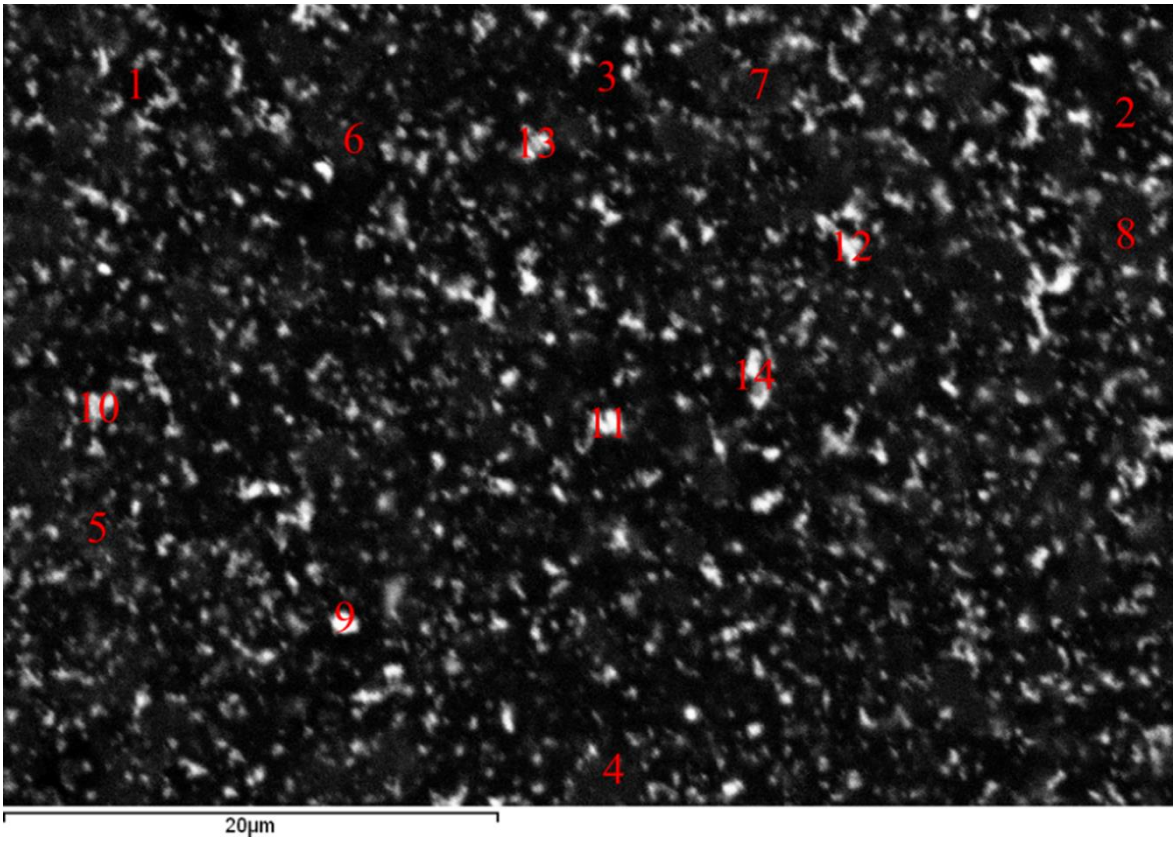

Fig. 5-15 Backscattered electron image of sample with composition of Al_2O_3 (300nm): $KBSi_2O_6$: CaO=1.07: 1: 0.4 sintered at 900°C. The numbers specify the locations of point analyses.

When sintered at 900°C, the dark and grey regions, as well as the white dots, remain in the sample as shown in Fig. 5-15. And the white dots are evidently more and growing larger than those in the sample sintered at 850°C in Fig. 5-14. This is consistent with the XRD result that the amount of $CaAl_2Si_2O_8$ phase increases with the sintering temperature rising. For the dark phase, it is still rich in Al but the element ratios have greatly changed in Tab. 5-3, which means the ions exchanges have happened for the crystal growth of $CaAl_2Si_2O_8$ phase. For the grey $KAlSi_2O_6$ phase, the amount of K increases because it is not tolerated in the $CaAl_2Si_2O_8$ structure.[30]

Tab. 5-3 Point analyses of different regions in the sample sintered at 900°C.

	Spectrum	O	Al	Si	K	Ca	Si/Al	K/Al	Ca/Al	Ca/K
Dark region	Spectrum 1	64.64	13.85	10.46	6.79	4.26	0.76	0.49	0.31	0.63
	Spectrum 2	63.89	14.38	10.71	6.77	4.25	0.74	0.47	0.30	0.63
	Spectrum 3	63.54	14.22	10.89	6.98	4.36	0.77	0.49	0.31	0.62
	Average	64.02	14.15	10.69	6.85	4.29	0.76	0.48	0.30	0.63
Grey region	Spectrum 4	61.17	10.64	18.38	9.06	0.75	1.73	0.85	0.07	0.08
	Spectrum 5	64.07	12.49	13.10	7.38	2.97	1.05	0.59	0.24	0.40
	Spectrum 6	62.44	11.81	15.52	8.18	2.06	1.31	0.69	0.17	0.25
	Spectrum 7	61.56	12.07	16.06	8.31	2.00	1.33	0.69	0.17	0.24
	Spectrum 8	60.79	11.53	17.73	8.61	1.34	1.54	0.75	0.12	0.16
	Average	62.01	11.71	16.16	8.31	1.82	1.38	0.71	0.15	0.23
White dots	Spectrum 9	63.71	14.29	11.20	7.10	3.70	0.78	0.50	0.26	0.52
	Spectrum 10	61.29	13.09	15.88	7.88	1.86	1.21	0.60	0.14	0.24
	Spectrum 11	64.80	13.12	11.56	7.06	3.45	0.88	0.54	0.26	0.49
	Spectrum 12	63.00	13.22	12.54	7.60	3.65	0.95	0.57	0.28	0.48
	Spectrum 13	64.16	13.76	11.07	6.94	4.07	0.80	0.50	0.30	0.59
	Spectrum 14	63.00	14.06	11.61	7.27	4.07	0.83	0.52	0.29	0.56
	Average	63.33	13.59	12.31	7.31	3.47	0.91	0.54	0.25	0.48

The compatibility of above samples with silver electrode are further characterized. Fig. 5-16a and Fig. 5-16b present the cross section of the sample with Ag electrode co-fired at 850°C and

900°C, respectively. It can be seen that silver electrodes are tightly combined with the ceramic without any obvious cracking or delamination. Also a series of point analyses are done in the direction perpendicular to the interface, as illustrated by the arrows in red colour, to characterize the diffusion of silver. As shown in Fig. 5-16c, the Ag profile decreases dramatically at the interface, which means the Ag should not diffuse into the ceramics when sintered at 850°C and 900°C. When the point analyse conducted too close to the interface (<2μm), the atomic percentage of Ag is influenced by the electrode due to the EDS interaction volume. It is worth to point out that the accurate Ag profile might be more shaper because the profile we characterized here might be affected by smearing effect caused by soft silver electrode during polishing.

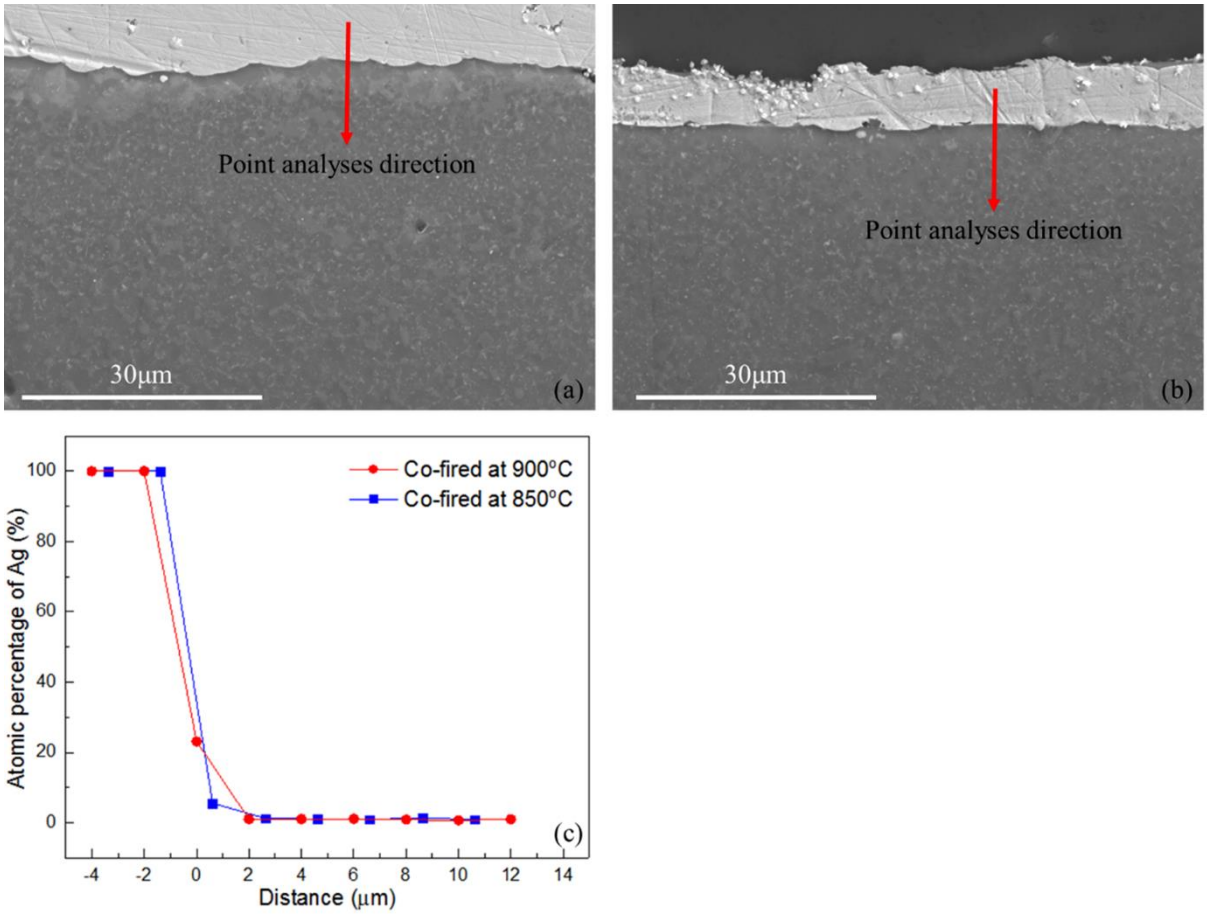

Fig. 5-16 SEM image of the cross section of sample co-fired with Ag electrode at (a) 850°C; (b) 900°C; (c) atomic percentage of silver in a series of point analyses.

5.5 Conclusion

$KBSi_2O_6$ phase has been successfully introduced to develop the crystalline composite for

LTCC application. Its lattice parameters are obtained by XRD refinement using Rietveld method. Based on the optimization of three components, we initially developed a composite with composition of Al_2O_3 (300nm): $KBSi_2O_6$: CaO=1: 1: 0.4. The resultant phases in the sintered sample include tetragonal $KAlSi_2O_6$ phase, hexagonal Al_2O_3 phase and monoclinic $CaAl_2Si_2O_8$ phase. To achieve the sample with higher resistivity, the amount of Al_2O_3 and $KBSi_2O_6$ in the raw materials are further adjusted. Finally, the optimal composite, whose composition is Al_2O_3 (300nm): $KBSi_2O_6$: CaO=1.07: 1: 0.4 (mole ratio), shows relative permittivity of ~8, dielectric loss below 0.002 @1MHz, resistivity of ~$10^{13}\Omega\cdot$cm and CTE of 11.04~12.46ppm/^{o}C when co-fired from 850^{o}C to 900^{o}C. Besides, they are compatible with silver electrode based on EDS characterization. This comprehensive and good performance is promising for LTCC application in high frequency.

Reference

1. Wen-Hao Jiang, Jian-Hong Liu, Yin Liu, Ge Jin, Jun Zhang, Jian-Wei Pan, 1.25GHz sine wave gating InGaAs/InP single photo detector with a monolithically integrated readout circuit. *Optics Letter* **2017,** *42*, 5090-5093.

2. Zheng, P.; Liu, Z.; Ma, M.; Wang, Y.; Liu, F.; Li, Y., Kα-Band LTCC Stacked Substrate Integrated Waveguide Bandpass Filter. *Wireless Communications and Mobile Computing* **2018,** *2018,* 1-7.

3. Shao, H.; Zhou, H.; Zhu, H.; Shen, X., Preparation and properties of crystallizable Glass/Al_2O_3 composites for LTCC material. *Journal of Wuhan University of Technology-Mater. Sci. Ed.* **2011,** *26* (6), 1174-1178.

4. Hong, K. P.; Choi, I. J.; Jung, J. W.; Choi, H. R.; Cho, Y. S.; Kwak, J.; Kang, D. H., Densification, Crystallization, and Dielectric Properties of AlN, BN and Si_3N_4 Filler-Containing LTCC Materials. *International Journal of Applied Ceramic Technology* **2013,** *10,* E25-E32.

5. Huang, C.-L.; Lin, R.-J.; Wang, J.-J., Effect of B_2O_3 Additives on Sintering and Microwave Dielectric Behaviors of CuO-Doped $ZnNb_2O_6$ Ceramics. *Japanese Journal of Applied Physics* **2002,** *41* (Part 1, No. 2A), 758-762.

6. Zeng, Q.; Li, W.; Shi, J.-l.; Guo, J.-k., Microwave Dielectric Properties of $5Li_2O$-$0.583Nb_2O_5$-$3.248TiO_2$ Ceramics with V_2O_5. *Journal of the American Ceramic Society* **2006,** *89* (10), 3305-3307.

7. Xu, Y.; Huang, G.; He, Y., Sol–gel preparation of $Ba_{6-3x}Sm_{8+2x}Ti_{18}O_{54}$ microwave dielectric ceramics. *Ceramics International* **2005,** *31* (1), 21-25.

8. Seo, Y. J.; Jung, J. H.; Cho, Y. S.; Kim, J. C.; Kang, N. K., Influences of Particle Size of Alumina Filler in an LTCC System. *Journal of the American Ceramic Society* **2007,** *90* (2), 649-652.

9. Takahiro Takada, Sea Fue Wang, Shoko Yoshikawa, Sei-Joo Jang and Robert E. Newnham, Effect of glass addition on BaO-TiO_2-WO_3 microwave ceramics. *J. Am. Ceram. Soc.* **1994,** *77*, 1909-1916.

10. Thomas, D.; Abhilash, P.; Sebastian, M. T., Casting and characterization of $LiMgPO_4$ glass free LTCC tape for microwave applications. *Journal of the European Ceramic Society* **2013,** *33* (1), 87-93.

11. Thomas, D.; Sebastian, M. T., Effect of Zn^{2+} substitution on the microwave dielectric properties of $LiMgPO_4$ and the development of a new temperature stable glass free LTCC. *Journal of the European Ceramic Society* **2012,** *32* (10), 2359-2364.

12. Sebastian, M. T.; Jantunen, H., Low loss dielectric materials for LTCC applications: a review. *International Materials Reviews* **2013,** *53* (2), 57-90.

13. Dong-Wan Kim, Kyung Hyun Ko and Kug Sun Hong, Influence of copper(II) oxide addition to zinc niobate microwave ceramics on sintering temperature and dielectric properties. *J. Am. Ceram. Soc.* **2001,** *84*, 1286–1290.

14. M. Udovic, M. Valant, D. Suvorov, Dielectric characterisation of ceramics from the TiO_2-TeO_2 system. *Journal of the European Ceramic Society* **2001,** *21*, 1735–1738.

15. Rajesh, S.; Jantunen, H.; Letz, M.; Pichler-Willhelm, S., Low Temperature Sintering and Dielectric Properties of Alumina-Filled Glass Composites for LTCC Applications. *International Journal of Applied Ceramic Technology* **2012,** *9* (1), 52-59.

16. Di, Z.; Li-Xia, P.; Ze-Ming, Q.; Biao-Bing, J.; Xi, Y., Novel ultra-low temperature co-fired microwave dielectric ceramic at 400 degrees and its chemical compatibility with base metal. *Sci Rep* **2014,** *4*, 5980.

17. Turnmala, R. R., Ceramic and glass-ceramic packaging in the 1990s. *J. Am. Ceram. Soc.* **1991,** *74*, 895-908.

18. Voldan J., Crystallization of a three-component compound in the system K_2O–SiO_2–B_2O_3. *Silikaty* **1979,** *23*.

19. I. Yanase, H. Kobayashi and T. Mitamura, Thermal property and phase transition of the synthesized new cubic leucite-type compounds. *Journal of Thermal Analysis and Calorimetry* **1999,** *57*, 695-705.

20. J. F. Schairer and N. L. Bowen, The system K_2O-Al_2O_3-SiO_2. *American Journal of Science* **1955,** *253*, 681-746.

21. Masayoshi IHARA, Fumio KAMEI, Crystal structure of potassium borosilicate, K_2O-B_2O_3-$4SiO_2$. *Journal of the Ceramic Association, Japan* **1980,** *88*, 40-43.

22. Krzhizhanovskaya, M. G.; Bubnova, R. S.; Filatov, S. K., Crystallography and high-temperature crystal chemistry of anhydrous borosilicates of alkali and alkali-earth metals. *Journal of Structural Chemistry* **2015,** *55* (7), 1342-1355.

23. Zhang, Y.; Lv, M.; Chen, D.; Wu, J., Leucite crystallization kinetics with kalsilite as a transition phase. *Materials Letters* **2007,** *61* (14-15), 2978-2981.

24. R. S. Bubnova, A. A. Levin, N. K. Stepanov, A. Belger, D. C. Meyer, I. G. Polyakova, S. K. Filatov and P. Paufler, Crystal structure of $K_{1-x}Cs_xBSi_2O_6$ (x=0.12, 0.50) boroleucite solid solutions and thermal behavior of $KBSi_2O_6$ and $K_{0.5}Cs_{0.5}BSi_2O_6$. *Z. Kristallogr*. **2002,** *217*, 55-62.

25. Seiji BAN, Kenji MATSUO, Haruhiko IWASE, Kentaro KAIKAWA and Jiro HASEGAWA, Lattice parameter changes of leucite by incorporation of various cations substituted for potassium. *Dental Materials Journal* **1999,** *18 (4)*, 385-394.

26. F. Mazzi, E. Galli, G. Gottardi, The crystal structure of tetragonal leucite. *American Mineralogist* **1976,** *61*, 108-115.

27. Joseph L. Rosenholtz and Dudley T. Smith, The dielectric constant of mineral powders. *American Mineralogist* **1936,** *21*, 115-120.

28. Chen, S.; Zhu, D.-g., Low-temperature densification sintering and properties of $CaAl_2Si_2O_8$ ceramics with MeO $2B_2O_3$ (Me = Ca, Sr, Ba). *International Journal of Minerals, Metallurgy, and Materials* **2015,** *22* (9), 977-986.

29. Seong-Hun Choe, Shuji Tanaka and Masayoshi Esashi, A Matched Expansion MEMS Probe Card with Low CTE LTCC Substrate. In *2007 IEEE International Test Conference*, IEEE: Santa Clara, CA, USA, 2007; pp 1-6.

30. Wells, A. F., *Structural Inorganic Chemistry*. 4 ed.; Clarendon: 1975.

Chapter 6 Main achievements and outlook

6.1 Main achievements

In this thesis, we have systemically developed five compositions for LTCC application. Four of them are based on sol-gel derived amorphous phases, and another is fully composed of crystalline materials. Their performance has reached requirements made by our industry partner for commercial application and details are presented in Tab. 6-1. Our developed materials are sinterable between 850 ºC and 900 ºC. And the dielectric constant covers the range from 4 to 12 and the dielectric loss is well below 0.003 (at 1MHz). Their dielectric properties can flexibly meet the requirements of various circuit designs with high fidelity. The resistivities are above 10^{12} Ω·cm, which means the samples are highly insulating and can prevent the coupling among adjacent components. The coefficient of thermal expansions (CTE) values match well with common chip substrates, such as silicon, alumina or printed circuit board. In addition, the developed materials are all compatible with silver electrode during co-firing. With such excellent and comprehensive performance, our industry partner can directly apply them to industry production using tape casting method.

Tab. 6-1 Performance of developed samples in this project. The chemical composition of Amorphous phase-1 is 79.51% SiO_2-0.81% Na_2O-2.41% K_2O-2.50% CaO-14.77% B_2O_3 (mole ratio), and that of Amorphous phase-2 is 80.78% SiO_2-0.27% Na_2O-0.87% K_2O-3.45% CaO-5.25% BaO-9.38% B_2O_3 (mole ratio).

Target		Compositions				
		Composites based on amorphous phases				Crystalline composite
		49.81% Al_2O_3+50.19% Amorphous phase-1	53.35% Al_2O_3+46.65% Amorphous phase-2	60% ZrO_2+40% Amorphous phase-1	52.38% SiO_2+42.86% Amorphous phase-1+4.76% Al_2O_3	Al_2O_3:$KBSi_2O_6$:CaO =1.07:1:0.4 (mole ratio)
Sintering temperature	850~900ºC	850 ~ 900ºC	850 ~ 900ºC	850ºC	850ºC	850 ~ 900ºC
Permittivity	4~12 @1MHz	7.00 ~7.17	7.27-7.81	11.27	4.86	8.18 ~ 8.37
Dielectric loss	≤0.003 @1MHz	0.0022 ~ 0.0026	0.0012 ~ 0.0019	0.0008	0.0028	0.0019 ~ 0.0024
Resistivity	≥ 10^{12} Ω·cm @100V DC	1.51×10^{13} ~ 8.99×10^{13}	7.22×10^{13} ~ 1.69×10^{14}	3.9×10^{12}	2.52×10^{12}	8.72×10^{12} ~ 1.04×10^{13}
Coefficient of thermal expansion (ppm/ºC)		5.92 ~ 6.03	5.96 ~ 6.05	6.09	3.26	11.04 ~ 12.46
Compatible with silver electrode		Yes	Yes	Yes	Yes	Yes

Different with other reported LTCC materials, the amorphous phases in our samples are

synthesized by sol-gel method, instead of the conventional melt-quench method. The nominal composition of Amorphous phase-1 is 80.01% SiO_2-0.78% Na_2O-2.33% K_2O-2.33% CaO-14.55% B_2O_3 (mole ratio), and that of Amorphous phase-2 is 81.06% SiO_2-0.28% Na_2O-0.85% K_2O-3.40% CaO-5.09% BaO-9.32% B_2O_3 (mole ratio). The tetraethyl orthosilicate (TEOS) is firstly hydrolysed in the acid environment and the corresponding dopants are then randomly integrated into the amorphous network during the condensation process. These sol-gel derived amorphous phases not only possess low softening temperature (~800 ^oC), but also can be synthesized at lower temperature (600 ^oC~700 ^oC). As reported in literature, the evaporation of some low melting components, such as B_2O_3, have been confirmed in the glasses fabricated by the conventional melt-quench method due to high melting temperature (~1500 ^oC). Using the sol-gel method proposed in this work, the resultant chemical composition of Amorphous phase-1 is 79.51% SiO_2-0.81% Na_2O-2.41% K_2O-2.50% CaO-14.77% B_2O_3 (mole ratio), and that of Amorphous phase-2 is 80.78% SiO_2-0.27% Na_2O-0.87% K_2O-3.45% CaO-5.25% BaO-9.38% B_2O_3 (mole ratio). These results remain close the nominal compositions, which means the deficiency of melt–quench method has been made up by the sol-gel method thanks to the low synthesis temperature. When sintered with Al_2O_3, the structures and required properties are systemically characterized. Both composites show dielectric constant of 7~8 at 1MHz, dielectric loss below 0.003 at 1MHz and resistivity above 10^{13} Ω·cm when sintered between 850 ^oC and 900 ^oC. Besides, they also show CTE of ~ 6 ppm/^oC and are compatible with silver electrodes. These results also imply it is feasible to use the sol-gel derived amorphous phases in the LTCC materials.

When sintered with monoclinic ZrO_2, the ratio between ZrO_2 and the sol-gel derived Amorphous phase-1 shows evident influence on the crystallization process and the electrical properties. Although the dielectric constant can be adjusted by increasing the amount of ZrO_2 in the raw material, the cristobalite phase remains in the sample. The thermal expansion characterization illustrates the cristobalite phase causes abrupt change between 100 ^oC and 200 ^oC due to its displacive phase transition. We have successfully suppressed the formation of this phase by reducing the soaking period in this case, and this has been proved by the X-ray diffraction (XRD), microstructure and thermal expansion characterization. Finally, a new

composite with the composition of ZrO_2: Amorphous phase-1=60: 40 (mass ratio) has been developed. It shows relative permittivity of ~11 (at 1MHz), dielectric loss ~0.0008 (at 1MHz), resistivity of 2.3×10^{12} Ω·cm and CTE of 6.09 ppm/°C when sintered at 850 °C for 30min. Besides these, it is compatible with silver electrode and the dielectric properties show low dependence on either frequency or temperature.

The composite based on Amorphous phase-1 and pure fused SiO_2 shows good dielectric properties when sintered between 800 °C and 900 °C. However, the XRD results illustrate the sintered sample also contains undesired cristobalite phase. The formation of this phase can be suppressed by addition of 5 wt% Al_2O_3 but the sintering temperature is limited at 800 °C, which is not high enough to fully get rid of the organic group involved in the industrial tape-casting process. We support the cristobalite phase in this case is from the sol-gel derived Amorphous phase-1 because it is more inclined to get crystallized than the pure fused SiO_2 based on the XRD characterization. As a result, we systemically changed the amount of the sol-gel derived Amorphous phase-1 in the raw materials. We have found the amount of the cristobalite phase reduces when less Amorphous phase-1 is used, which support our assumption that the cristobalite comes from the sol-gel derived Amorphous phase-1. But the sintered sample is not densified well when the amount of Amorphous phase-1 is too low. On balance, the sample with composition of 42.86 wt% amorphous phase-52.38 wt% fused SiO_2-4.76 wt% Al_2O_3 sintered at 850 °C exhibited the relative permittivity of ~5, dielectric loss below 0.003 (at 1MHz), resistivity above 10^{12} Ω·cm and CTE of 3.26 ppm/°C. Besides, it is also compatible with silver electrode and shows low dependence of either frequency or operation temperature. This sample is quite favour of rapid signal transition since the signal propagation delay is proportional to the square root of dielectric constant.

Except adding amorphous phases to reduce the sintering temperature, we also developed a LTCC composite fully composed of crystalline phases, which has intrinsic low sintering temperature. We employ the $KBSi_2O_6$ for its advantage of B atom inside can be substituted by Al under low temperature, along with the phase transition from the cubic phase to tetragonal phase. This substitution can lead to good combining behaviour of phases in the sintered samples. Based on the optimization of three components, we initially developed a composite with

composition of Al_2O_3 (300nm): $KBSi_2O_6$: CaO=1: 1: 0.4. The resultant phases in the sintered sample include tetragonal $KAlSi_2O_6$ phase, hexagonal Al_2O_3 phase and monoclinic $CaAl_2Si_2O_8$ phase. Because the CaO in the raw materials is necessary for the crystallization of $CaAl_2Si_2O_8$ phase which does not present significant impacts on the resistivity of resultant samples, the amounts of other raw materials, *i.e.*, Al_2O_3 and $KBSi_2O_6$, are further adjusted to achieve the sample with higher resistivity. Finally, the optimal nominal composite, whose composition is Al_2O_3 (300nm): $KBSi_2O_6$: CaO=1.07: 1: 0.4 (mole ratio), shows dielectric constant of ~8, dielectric loss below 0.002 at 1MHz, resistivity of ~10^{13} Ω·cm and CTE of 11.04~12.46 ppm/^oC when sintered from 850 ^oC to 900 ^oC.

Overall, our independently developed sol-gel derived amorphous phase-based composites and the crystalline composition are promising for commercial application thanks to their excellent and comprehensive performance. The developing process also provides a guidance for the further development of LTCC materials.

6.2 Future work

In view of the results presented in this project and the current research status reflected in the literature, some continuing work related to the developed materials can be done.

(1) For the sol-gel derived amorphous phases, we use corresponding nitrates as the source for various metals because they can be removed at low temperature and are much cheaper than corresponding alkoxides source. However, they are flammable and might cause fire when used in large scale. Therefore, it would be better if any other alternative can be found. The possible choice should avoid causing pH fluctuation when introduced to hydrolysed TEOS solutions.

(2) In this thesis, we have developed samples with comprehensive and excellent performance in the lab for LTCC application. For the sake of large scale production, more research needs to be made on the tape casting method. As mentioned in Chapter 1, the organics have played an important role in forming of the green tapes and its composition is rather complicated. The amount of the organics and the ratio of components inside are highly depended on the LTCC

materials. This means the specific organics should be appropriately designed according to LTCC materials.

(3) Since the signal propagation delay is proportional to the square root of the dielectric constant of the LTCC materials, future work could do is to develop the samples with dielectric constant below 4. It may be possible to realize it by replacing the amorphous phase in the developed sample with oxyfluoride amorphous phase. This is because that the contribution of electrons in the polarization decreases with the introducing of fluorine.

Publication

Shiwo Ta, Xiaozhou Wang, Tao Chen, Yun Liu, Terry J. Frankcombe, Zhenxiao Fu, Xiuhua Cao, Chunyuan Hu, A low temperature co-fired dielectric material with adjustable dielectric constant and preparation method thereof. PCT invention patent (2020), CN2020/082252. Chinese invention patent (2020), 202010221314. X.